INVESTIGATIONS OF THE SOUND GENERATED BY SUPERCAVITY VENTILATION

M. S. Howe and A. W, Foley
Boston University, College of Engineering
110 Cummington Street, Boston MA 02215

Report No. ME09 - 13
20 August, 2009

Final Technical Report of work performed under
ONR Grant No. N00014-06-1-0270
University/Laboratory Initiative

Prepared for
Office of Naval Research, Code 333
875 N. Randolph St., One Liberty Center
Arlington, VA 22203-1995

ABSTRACT

An investigation is made of the sound generated by the impingement of a ventilating jet on the gas-water interface of a ventilated supercavity. A ventilated supercavity is a gaseous envelope generated around an underwater vehicle that allows for order of magnitude increases in vehicle speeds. However, the hydrodynamic noise generated by the supercavity can interfere with successful deployment of the vehicle. One of the principal mechanisms of noise generation is believed to be the impingement of the cavity ventilating gas jets on the gas-water cavity wall. An understanding of the acoustic field generated by this interaction has been developed by analysis of a series of model problems which approximate the geometry and physical mechanisms involved in the jet-cavity interaction. The first problem is that of a spherical, gas-filled cavity in water whose surface is excited by a planar ring of axially projecting jets originating from the center of the sphere. The second involves a jet of infinitesimal cross-section impinging at normal incidence on the gas-water interface. The final problem makes use of a creeping mode diffraction theory to estimate the ‘self-noise’ produced by the impinging jets on the solid nose of the vehicle.

These problems provided insight into the general characteristics of the field and its dependence on typical flow conditions. To apply these solutions to the problem of the supercavity, experimental studies were made in collaboration with the Applied Research Laboratory (ARL) at Penn State University. These included measurement of the unsteady force exerted by a jet on an interface, the results of which have been used to make theoretical predictions of the self-noise generated by a model-scale supercavity currently in use at ARL. The final results of this project will aid current and future naval research into supercavity noise and methods for its reduction.

Contents

List of Tables

List of Figures

Chapter 1

Introduction

A ventilated supercavity is a gaseous envelope generated around an underwater vehicle that allows for significant increases in vehicle speed. However, the hydrodynamic ‘self-noise’ generated by the supercavity can interfere with successful deployment of the vehicle. In order to reduce or eliminate this problem it is necessary to understand and quantify the noise production mechanisms. One of the principal sources of noise is believed to be the impingement on the supercavity wall of the cavity-ventilating gas jets, and the outcome of this project will be an understanding of this mechanism and its probable impact on the self-noise problem.

1.1 Motivation

The successful development of high-speed supercavitating underwater vehicles is an important U.S. Navy objective. All aspects of the technology are being vigorously promoted by the Office of Naval Research and at various naval laboratories. The primary goal of this project is to provide naval researchers with an understanding of the characteristics of the sound generated by the ventilating jets of a supercavitating vehicle. This will facilitate current investigations of the overall sound generated by such vehicles, and permit the development of methods for its control and reduction.

1.2 Background

1.2.1 Cavitation

Cavitation is the development of a pocket of gas or vapor inside a liquid volume. It is driven by a drop in pressure to a level below the liquid's vapor pressure causing it to change phase (the temperature-driven equivalent to this is boiling). Cavitation can occur in liquids either in motion or at rest, and both in the body of the liquid or on solid boundaries. The form of hydrodynamic cavitation, cavitation in flowing liquids, of particular relevance to underwater vehicles is fixed cavitation, or cavitation which develops attached to a solid boundary. The boundary geometry causes the detachment of the liquid boundary layer from the solid wall, otherwise known as flow separation. High velocity (and *ergo* low pressure) flow allows for cavitation inception in the separation region. Here small cavities coalesce into a large cavity attached to the boundary. Without separation and this region of relative calm, any small cavities which may form are unable to attach to the boundary as they are rapidly convected away by the liquid flow [4, 14, 26].

If favorably low pressures persist, the cavity is maintained or may continue to expand downstream of the inception cite. Cavities which initiate and close on the same solid boundary are known as *partial* cavities. Cavities which terminate downstream of the boundary or body on which they initiate are referred to as *supercavities*. The artificial admission of gas, either into a region of separated flow to initiate a cavity or into a partial cavity or supercavity to expand and maintain it, is called *ventilation*. Ventilated cavities behave comparably with natural cavities except in the aft region of gas exhaustion and fluid entrainment and the potential deformation of the cavity due to gravity (relevant only at low flow velocities) [4, 14, 26]. The method of gas exhaustion as it applies to ventilated supercavitating vehicles is discussed below.

1.2.2 Supercavitating vehicles

An underwater vehicle can attain high forward speeds by the development of a gaseous ventilated supercavity which eliminates skin friction and reduces drag by up to 90% [7, 27]. The cavity is initiated downstream of a specially designed ‘cavitator’ on the vehicle nose. It is expanded to contain the entire aft section of the vehicle, except for control surfaces used for guidance, by the injection of gas from sources just aft of the cavitator (Fig.1.1). The cavity can be maintained in a stable configuration by carefully controlling the gas injection rate to avoid overpressures and instabilities that can cause the cavity to pulsate [14, 27, 41, 43]. Under stable conditions, involving high speed motion through the water, the gas exhausts from the rear end of the cavity by the quasi-periodic shedding of ring vorticies with gaseous cores. At low speeds (i.e. at low Froude numbers that are not necessarily relevant in the present context) the supercavity resembles a hot ’plume’ and gas escapes through two trailing, hollow vortex tubes formed by buoyancy-induced plume bifurcation [14, 39].

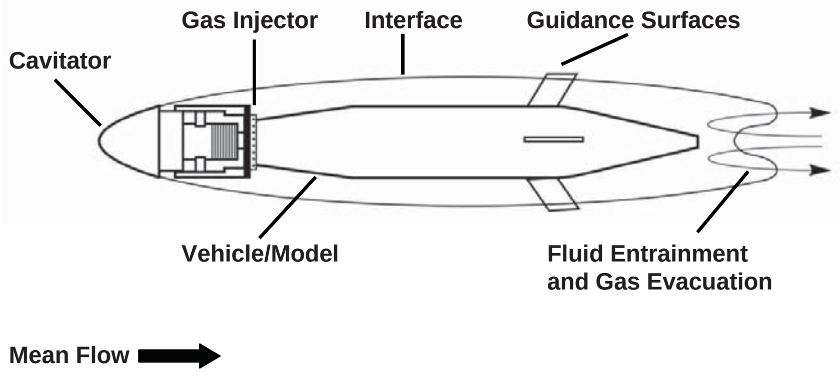

Figure 1.1. Schematic experimental supercavity

The supercavity is a significant source of aerodynamic sound that can interfere with the underwater vehicle’s guidance systems, inhibiting successful deployment [6, 18, 19, 32] (see Appendices A and B for a brief review of concepts from acoustic theory relevant to this work). Turbulence in the aqueous boundary layer approaching the wetted trailing edge of the cavitator from the nose generates sound and hydrodynamic pressure fluctuations as it convects across the edge [19, 21, 48]. To analyze sources further downstream it is reasonable in a first approximation to neglect pressure fluctuations within the cavity because of the vast difference in mass densities of the gas and water, in which case the gas-water interface can be treated as a pressure-release surface. Then the sound generated by turbulence quadrupoles in the flow adjacent to the cavity edge should be relatively unimportant, because the pressure-release interface causes the sound pressure to vary as $\rho_w v^2 M^3$, where the Mach number $M = v/c_w \ll 1$, v being the flow velocity and ρ_w, c_w are respectively the mean density and sound speed in water [12]. Bubbles and water droplets in the break-up region of the cavity far downstream are respectively equivalent to monopole and dipole sources; except at extremely high frequencies their importance is again greatly reduced by the proximity of the pressure-release cavity.

Observation suggests that the acoustic noise is dominated over a broad range of frequencies by the unsteady impingement of the ventilating jets on the cavity wall [48]. The jets ripple the gas-water interface, producing unsteady surface forces and a distributed acoustic surface source of dipole type. In order to investigate the noise from this source independently from other mechanisms at work in and around the supercavity, a theoretical description of the impingement mechanism as an acoustic source is required.

To facilitate the development of these mathematics, we will consider a slightly modified gas injection system. On typical ventilated supercavitating vehicles, a gas deflector is fitted over the gas injection site, as in Figure 1.2. This redirects the jets to impact the cavity at shallow incidence. We will choose instead to consider that the gas deflector is absent (as in Fig. 1.3), such that the jets impact the cavity at *normal* incidence. This configuration allows for much simpler geometric approximations of the jet-cavity interaction to be used in the theoretical work. Furthermore, the removal of the gas deflectors from the experimental model will promote sound production via the impingement mechanism, expediting the in-water acoustic surveys of the supercavity to be performed by naval researchers.

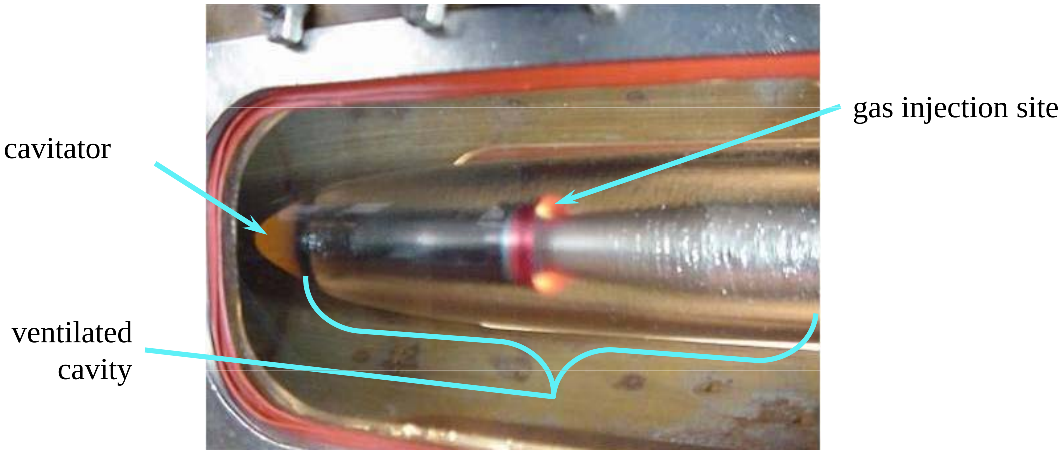

Figure 1.2. Experimental vehicle inside ARL 305 mm water tunnel

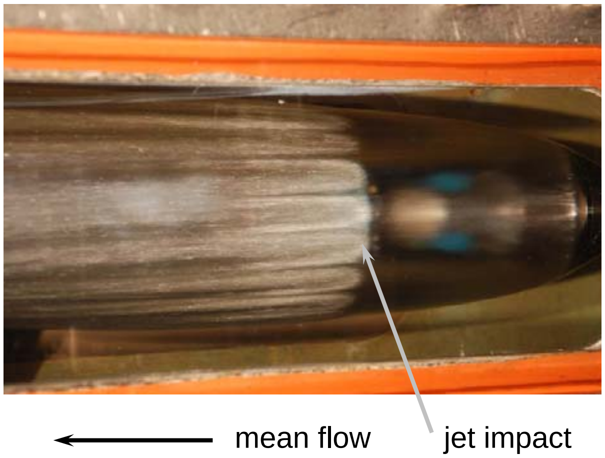

Figure 1.3. Experimental vehicle inside ARL 305 mm water tunnel with gas deflectors removed and jets impinging at normal incidence on the cavity interface

1.2.3 Discussion of existing literature

A literature survey revealed that the dynamics of jet impingement are well explored. Extensive experimental and theoretical studies of impingement on both rigid and free surfaces have been made (see [17, 36, 46] and their bibliographies as examples thereof). A significant amount of attention has been payed to the heat transfer problem of jet impingement on a plate due to its prevalence in manufacturing processes, however such work is of no relevance for the supercavity problem. The acoustics of a jet impinging on a plate have likewise been explored [28, 34, 40], though almost exclusively experimentally. Furthermore, these studies focus on mechanisms of noise generation (such as shed vorticity and turbulence) other than the unsteady motion of a free surface. No theoretical description of the sound generated by jet impingement on a gas-water interface exists; it is necessary to develop this formulation for the acoustic field using the equations and methods fundamental to the study of hydroacoustics. The few existing studies which may then prove relevant to the supercavity problem are those which provide information about the unsteady pressure exerted by the jet on an impingement surface (as in Strong *et al.* [45]). These experimental results may serve as a 'check' of empirical studies of the supercavity jets and of the generality of the mathematical formulation of the generated sound.

1.3 Approach

The problem was investigated by consideration of a series of model problems and related experiments involving predictions made on the basis of approximations to the geometry and physical mechanisms governing the jet-cavity interaction. The simplest approximation involves a ventilated supercavity in the form of a spherical, gas-filled cavity in water whose interior surface is excited by a planar ring of axially projecting jets originating from the center of the sphere. This problem was not designed to predict the acoustic field generated by the supercavity jets; it was a convenient starting point which provided general insight into the behavior of the field and the source mechanisms at work in the supercavity. The solution of the sphere problem yielded insight into the directivity of the sound radiating into the water and the likely contributions from cavity resonances; it also enabled the exploration of the importance of several damping mechanisms.

The second problem examined was the production of sound by a jet of infinitesimal cross-section impinging at normal incidence on a planar gas-water interface. Its solution was formulated in terms of the force exerted by the jet on the cavity wall. The resulting prediction of the acoustic field helps in understanding the more complex issues involved in the related problem of jet impingement on a cylindrical cavity.

To apply these general solutions to the problem of the supercavity an empirical knowledge of the gas injection jets was required. This knowledge was gained through experiments made in collaboration with the Applied Research Laboratory (ARL) at Penn State University. These experiments included measurement of the unsteady force exerted by a jet on an interface, the results of which were then used to make theoretical predictions of the self-noise generated by a model-scale supercavity in use at ARL.

The results were used finally to estimate the contribution to the self-noise at the vehicle nose from the jet impingement source. This was accomplished by use of a creeping mode diffraction theory to model propagation of sound over the rounded nose region. To do this the supercavity was modeled as a semi-infinite cylindrical cavity to the rear of a solid, elliptical nose section with a prescribed surface impedance. The cavity is excited by gas-jet impingement downstream of the cavitator which generates a separately derived pressure field. This pressure field was used in the diffraction theory to predict the sound at the nose and thereby permit more definitive conclusions to be drawn regarding the presence of noise in the vicinity of the guidance system at the nose.

1.4 Outline

Chapter 2 describes the general problem of a spherical ventilated cavity. The sound produced by jet impingement on a planar gas-water interface is explored mathematically in Chapter 3. The experiments measuring the force exerted by the scale-model vehicle's gas injection jets are detailed in Chapter 4, as are preliminary predictions for the impingement generated sound. The impingement noise heard at the nose is determined in Chapter 5. Chapter 6 summarizes the body of work and its findings and presents recommendations for future research into ventilated supercavity acoustics.

Chapter 2

Sound generated by a jet-excited spherical cavity

This chapter examines the general behavior of the acoustic field generated by the impinging jets. A spherical cavity in which gas enters from the center in a ring of radially projecting jets is considered. This highly simplified geometry allows for general deductions about the generated sound without the difficulty implicit in a more complicated, realistic cavity geometry. The mathematical problem is formally solved by series expansion in Section 2.1. Section 2.2 discusses low frequency cavity resonances. High frequency sound is addressed in Section 2.3. Specific results and conclusions are drawn by choosing the volume of the cavity to be approximately the same as that of a typical experimental supercavity. The work presented in this chapter has also appeared in *Journal of Sound and Vibration* [13].

2.1 The acoustic problem

2.1.1 Problem formulation

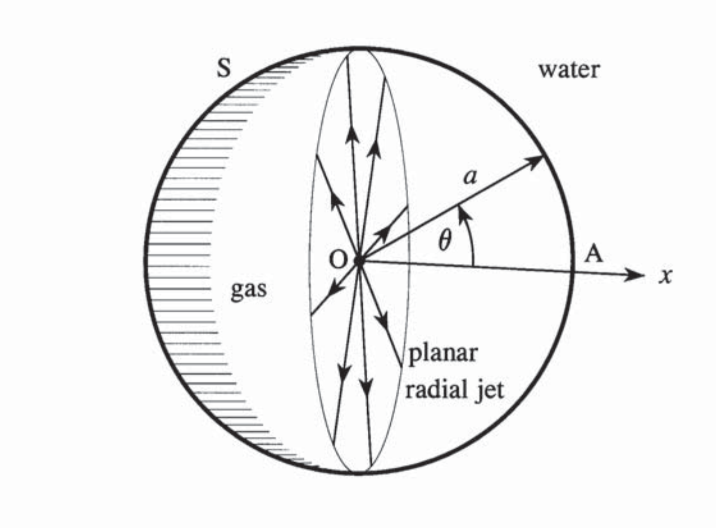

Figure 2.1. Configuration of the spherical cavity

Consider a spherical cavity of undisturbed radius a in water of mean density ρ_w and sound speed c_w which is at rest at infinity. Let the origin O be at the center of the cavity (Fig.2.1) and introduce spherical polar coordinates (r, θ, ϕ) $(0 < \theta < \pi,\ 0 < \phi < 2\pi)$, where the latitude θ is measured from the positive x direction in the figure. Gas enters the cavity via a thin, axisymmetric planar jet from a source at O, and impinges normally on the cavity interface S along the great circle $\theta = \frac{\pi}{2}$. It is assumed that the mean volume of the cavity and the mean density ρ_o of the gas in the cavity are maintained constant by the steady exhausting of gas into the water from the 'rear end' of the cavity, say the vicinity of the point A in Fig. 2.1.

Turbulence fluctuations in the jet are assumed to be axisymmetric and to exert an unsteady radial force on the cavity interface equal to $F(t)$ per unit length of the circle of impingement on S. The definition of $F(t)$ is made precise by requiring it to equal the force that would be exerted on the interface by the jet when the interface is assumed to be *rigid*. The forced motion of the interface produces pressure fluctuations $p(r, \theta, t)$ that satisfy

$$\left.\begin{aligned} \left(\frac{1}{c_o^2}\frac{\partial^2}{\partial t^2} - \nabla^2\right)p &= 0, \quad r < a, \\ \left(\frac{1}{c_w^2}\frac{\partial^2}{\partial t^2} - \nabla^2\right)p &= 0, \quad r > a, \end{aligned}\right\} \tag{2.1}$$

respectively within the cavity and in the water, where c_o is the mean speed of sound in the gas.

The analytical problem is simplified by introducing the Fourier decomposition $F(t) = \int_{-\infty}^{\infty} F_o(\omega)\mathrm{e}^{-i\omega t}\, d\omega$ and considering first the solution for the case where the cavity is excited by a time-harmonic radial force $F_o(\omega)$ per unit length. The solution of the time-dependent problem can subsequently be found by application of the integral operator $\int_{-\infty}^{\infty}(\,\cdot\,)\mathrm{e}^{-i\omega t}\, d\omega$. Then time-harmonic pressure $p(r, \theta, \omega)$ satisfies

$$\left(\nabla^2 + k^2\right)p = 0, \quad \text{where} \begin{cases} k = k_o = \omega/c_o, & r < a \\ k = k_w = \omega/c_w, & r > a \end{cases} \tag{2.2}$$

The solution in the outer region $r > a$ must exhibit outgoing wave behavior. The two solutions in $r \lessgtr a$ are related by the conditions that the pressure and normal displacement are continuous at the interface. Because the force per unit area applied to the interface by the jet is $(F_o/a)\delta\left(\theta - \frac{\pi}{2}\right)$, the pressure will be continuous at $r = a$ provided

$$p(a+0, \theta, \omega) = p(a-0, \theta, \omega) + \frac{F_o}{a}\delta\left(\theta - \tfrac{\pi}{2}\right), \quad 0 < \theta < \pi. \tag{2.3}$$

Similarly, because F_o corresponds to the force exerted on a rigid interface, continuity of normal displacement is satisfied by requiring

$$\frac{1}{\rho_w}\left(\frac{\partial p}{\partial r}\right)_{r=a+0} = \frac{1}{\rho_o}\left(\frac{\partial p}{\partial r}\right)_{r=a-0}, \quad 0 < \theta < \pi, \tag{2.4}$$

because velocity fluctuations within the jet at the interface are balanced by the unsteady pressure gradient in the jet.

2.1.2 Solution in the general case

Within the cavity the time-harmonic solution that remains finite at $r = 0$ has the expansion [18, 44]

$$p = \sum_{n=0}^{\infty} A_n j_n(k_o r) P_n(\cos\theta), \quad r < a, \tag{2.5}$$

where j_n is a spherical Bessel function of the first kind, P_n denotes the Legendre polynomial of order n [1], and the coefficients A_n are to be determined. In the water the pressure is expanded in terms of outgoing radiating waves in the form

$$p = \sum_{n=0}^{\infty} B_n h_n^{(1)}(k_w r) P_n(\cos\theta), \quad r > a, \tag{2.6}$$

where the B_n are constants and $h_n^{(1)}$ is the spherical Hankel function of the first kind [1].

The coefficients $A_n,\ B_n$ are calculated from conditions (2.3) and (2.4). The first supplies

$$\sum_{n=0}^{\infty}\Big(B_n h_n^{(1)}(k_w a) - A_n j_n(k_o a)\Big) P_n(\cos\theta) = \frac{F_o}{a}\delta\left(\theta - \tfrac{\pi}{2}\right), \quad 0 < \theta < \pi, \tag{2.7}$$

which, by means of the orthogonality relation $\int_0^\pi P_n(\cos\theta)P_m(\cos\theta)\sin\theta\, d\theta = 2\delta_{nm}/(2n+1)$ and the formula $P_n(0) = \cos(\frac{n\pi}{2})\Gamma\left(\frac{n}{2}+\frac{1}{2}\right)\Big/\sqrt{\pi}\Gamma\left(\frac{n}{2}+1\right)$ [1], reduces to

$$B_n h_n^{(1)}(k_w a) - A_n j_n(k_o a) = \frac{F_o}{a}\frac{(2n+1)}{2\sqrt{\pi}}\cos\left(\tfrac{n\pi}{2}\right)\frac{\Gamma\left(\frac{n}{2}+\frac{1}{2}\right)}{\Gamma\left(\frac{n}{2}+1\right)}. \tag{2.8}$$

Condition (2.4) yields

$$\frac{B_n k_w}{\rho_w} h_n^{(1)\prime}(k_w a) - \frac{A_n k_o}{\rho_o} j_n'(k_o a) = 0, \tag{2.9}$$

where the prime denotes differentiation with respect to the argument. Hence

$$\left.\begin{aligned} A_n &= \frac{(2n+1)}{2\sqrt{\pi}}\cos\left(\tfrac{n\pi}{2}\right)\frac{\Gamma\left(\frac{n}{2}+\frac{1}{2}\right)}{\Gamma\left(\frac{n}{2}+1\right)}\frac{F_o}{a\, j_n(k_o a)(Z_n-1)} \\ B_n &= \frac{(2n+1)}{2\sqrt{\pi}}\cos\left(\tfrac{n\pi}{2}\right)\frac{\Gamma\left(\frac{n}{2}+\frac{1}{2}\right)}{\Gamma\left(\frac{n}{2}+1\right)}\frac{F_o Z_n}{a\, h_n^{(1)}(k_w a)(Z_n-1)} \end{aligned}\right\} \tag{2.10}$$

where

$$Z_n = \frac{\rho_w c_w}{\rho_o c_o}\frac{j_n'(k_o a)}{j_n(k_o a)}\frac{h_n^{(1)}(k_w a)}{h_n^{(1)\prime}(k_w a)}\ . \tag{2.11}$$

Now $\cos(\frac{n\pi}{2}) \equiv 0$ when n is odd. Therefore, by replacing n in the above expressions by $2n$, using the result [1]

$$\frac{\Gamma(n+\frac{1}{2})}{\Gamma(n+1)} = \sqrt{\pi}\frac{1\cdot 3\cdot 5 ... (2n-1)}{2^n n!} \equiv \sqrt{\pi}\frac{(2n)!}{(2^n n!)^2},$$

and substituting into the expansions (2.5) and (2.6), we deduce the following desired representations of the sound within the cavity and radiated into the water:

$$p(r,\theta,\omega) = \frac{F_o}{2a}\sum_{n=0}^{\infty}(-1)^n\frac{(4n+1)(2n)!}{(2^n n!)^2}\frac{P_{2n}(\cos\theta) j_{2n}(k_o r)}{(Z_{2n}-1) j_{2n}(k_o a)}, \quad r < a, \tag{2.12}$$

$$= \frac{F_o}{2a}\sum_{n=0}^{\infty}(-1)^n\frac{(4n+1)(2n)!}{(2^n n!)^2}\frac{Z_{2n} P_{2n}(\cos\theta) h_{2n}^{(1)}(k_w r)}{(Z_{2n}-1) h_{2n}^{(1)}(k_w a)}, \quad r > a. \tag{2.13}$$

2.1.3 Special limiting cases

It is also useful to note the corresponding forms of equations (2.12), (2.13) when (i) the water is regarded as *incompressible* (i.e. when $c_w \to \infty$), and (ii) there is no gas in the cavity ($\rho_o \to 0$).

In case (i) there can be no damping of the sound in the cavity by radiation losses, and we find

$$p(r,\theta,\omega) = \frac{F_o}{2a}\sum_{n=0}^{\infty}(-1)^n \frac{(4n+1)(2n)!}{(2^n n!)^2}\,\frac{P_{2n}(\cos\theta) j_{2n}(k_o r)}{(Z'_{2n}-1) j_{2n}(k_o a)}, \quad r < a, \tag{2.14}$$

$$= \frac{F_o}{2a}\sum_{n=0}^{\infty}(-1)^n \frac{(4n+1)(2n)!}{(2^n n!)^2}\,\frac{Z'_{2n} P_{2n}(\cos\theta)}{(Z'_{2n}-1)}\left(\frac{a}{r}\right)^{2n+1}, \quad r > a. \tag{2.15}$$

where

$$Z'_n = \frac{-\rho_w k_o a}{\rho_o(n+1)}\,\frac{j'_n(k_o a)}{j_n(k_o a)}. \tag{2.16}$$

In case (ii), where the cavity is treated as a vacuum, $Z_n \to \infty$ and there are no pressure fluctuations within the cavity ($p \equiv 0$ for $r < a$). Then expression (2.13) reduces to

$$p(r,\theta,\omega) = \frac{F_o}{2a}\sum_{n=0}^{\infty}(-1)^n \frac{(4n+1)(2n)!}{(2^n n!)^2}\,\frac{P_{2n}(\cos\theta) h^{(1)}_{2n}(k_w r)}{h^{(1)}_{2n}(k_w a)}, \quad r > a. \tag{2.17}$$

2.1.4 Suppression of coherent interior modes

Just inside the cavity interface the Bessel function $j_n(k_o r) = \frac{1}{2}\left(h^{(1)}_n(k_o r) + h^{(2)}_n(k_o r)\right)$ in the expansion (2.5) of the cavity pressure can be interpreted as representing a component traveling wave $\sim h^{(1)}_n(k_o r)$ *incident* on the interface from within the cavity, and a component $\sim h^{(2)}_n(k_o r)$ *reflected* from the interface. Waves reflected from the interface will subsequently impinge again on the interface, possibly leading to the establishment of coherent resonant oscillations. At high frequencies scattering by small scale irregularities on the interface will induce incoherence in the interior reflected wave field tending to suppress the growth of coherent resonances. By discarding the *incident* coherent component $h_n^{(1)}(k_o r)$ of the Bessel function we can therefore hope to mimic the effect of random interface scattering.

This is equivalent to repeating the analysis leading to the predictions (2.12) and (2.13) with $j_n(k_o r)$ replaced throughout by $h_n^{(2)}(k_o r)$, and yields

$$p(r,\theta,\omega) = \frac{F_o}{2a}\sum_{n=0}^{\infty}(-1)^n\frac{(4n+1)(2n)!}{(2^n n!)^2}\,\frac{P_{2n}(\cos\theta)h_{2n}^{(2)}(k_o r)}{(\hat{Z}_{2n}-1)h_{2n}^{(2)}(k_o a)}, \quad r<a, \tag{2.18}$$

$$= \frac{F_o}{2a}\sum_{n=0}^{\infty}(-1)^n\frac{(4n+1)(2n)!}{(2^n n!)^2}\,\frac{\hat{Z}_{2n}P_{2n}(\cos\theta)h_{2n}^{(1)}(k_w r)}{(\hat{Z}_{2n}-1)h_{2n}^{(1)}(k_w a)}, \quad r>a, \tag{2.19}$$

where

$$\hat{Z}_n = \frac{\rho_w c_w}{\rho_o c_o}\,\frac{h_n^{(2)\prime}(k_o a)}{h_n^{(2)}(k_o a)}\,\frac{h_n^{(1)}(k_w a)}{h_n^{(1)\prime}(k_w a)} \tag{2.20}$$

2.2 Low frequency resonances

The spectrum of sound radiated to large distances from a cavity tends to be dominated by low frequencies, comparable to the fundamental Minnaert volumetric pulsation frequency [6, 7]. This and other resonant oscillations of the cavity are excited by the jet. In this section we examine this excitation. Predictions will be illustrated for the case of an air-filled cavity in water at standard temperature and pressure (STP) when the cavity has radius $a = 7.0\,\mathrm{cm}$, which corresponds to a cavity volume approximately the same as that of a typical small scale experimental supercavity.

2.2.1 Monopole resonances

The monopole is nominally the most efficient source, but it is relevant only at very low frequencies. Volumetric pulsations are then analogous to oscillations of a mass-spring system in which the moving 'mass' is the water displaced radially by the cavity, and the 'spring' stiffness is furnished by the compressibility of the contained gas. The compressibility of the water makes a negligible contribution to the gross motion of the cavity at low frequencies, when the acoustic wavelength is very much larger than the radius a of the cavity. The resonance frequencies can therefore be calculated by ignoring the aqueous compressibility, which is responsible only for relatively weak radiation-damping of the oscillations. This is the only damping mechanism available to an ideal spherical cavity when viscous and thermal effects are ignored [11, 30]. However, our model implicitly assumes that the gas content of the cavity is maintained roughly constant by the steady exhausting of the gas into the water, and we shall estimate below the damping arising from this.

According to equations (2.14), (2.15) resonant oscillations of a mode of order $2n$ are determined by the zeros of $(Z'_{2n}(k_o a) - 1)\, j_{2n}(k_o a) = 0$ when the water is regarded as incompressible, where Z'_{2n} is defined as in equation (2.16). Using the relation $j'_n(z) = j_{n-1}(z) - \frac{n+1}{z} j_n(z)$, the resonance condition is equivalent to

$$k_o a j_{2n-1}(k_o a) - (2n+1)\left(1 - \frac{\rho_o}{\rho_w}\right) j_{2n}(k_o a) = 0. \tag{2.21}$$

For the monopole $n = 0$, (2.21) reduces to [1]

$$k_o a - \left(1 - \frac{\rho_o}{\rho_w}\right) \tan(k_o a) = 0. \tag{2.22}$$

When $\rho_o/\rho_w \ll 1$ the smallest positive root of this equation is $k_o a \approx \sqrt{3\rho_o/\rho_w}$, which corresponds to volumetric oscillations at the *Minnaert* radian frequency $\omega = \sqrt{3\rho_o c_o^2/\rho_w a^2}$

[11, 30] for which the pressure does not vary with position in the cavity.

For our model cavity with $a = 7\,\mathrm{cm}$ the Minnaert frequency $\omega/2\pi \sim 47\,\mathrm{Hz}$. But this mode is actually atypical of monopole resonances, because it corresponds to the special case in which the acoustic wavelength is much larger than the diameter of the cavity. Higher frequency volumetric resonances (determined by the larger roots of equation (2.22)) involve pressure fluctuations within the cavity that oscillate between positive and negative values with distance from the center. The first ten monopole modes are listed in Table 2.1: the wavelengths $2\pi/k_o$ of the higher order modes ($N > 1$) are always smaller than the cavity diameter.

mode number N	1	2	3	4	5	6	7	8
$k_o a$	0.06	4.49	7.73	10.90	14.07	17.22	20.37	23.52
frequency Hz	47	3,474	5,972	8,429	10,874	13,312	15,748	18,181

Table 2.1. Cavity monopole wavenumbers and frequencies at STP (from Eq. (2.22)).

The Nth order monopole resonance wavenumber k_o is well approximated at higher frequencies by the formula

$$(k_o a)_N = \frac{(2N-1)\pi}{2}\left\{1 - \frac{4(1-\rho_o/\rho_w)}{(2N-1)^2\pi^2}\right\}, \quad \text{for} \quad N \geq 4. \tag{2.23}$$

2.2.2 Influence of dissipation

The amplitudes of resonant modes excited by the jet are governed by losses produced by acoustic radiation, and by viscous and thermal diffusion [7, 11], and also by hydrodynamic convection of vibrational energy from the cavity by the steady outflow of gas into the water [18]. These mechanisms typically produce small corrections in the values of the resonance frequencies predicted in the absence of dissipation. The first order effect is that each undamped resonant frequency $\hat{\omega}$, say, is replaced by $\omega \approx \hat{\omega} - i\epsilon$, where $\epsilon = \epsilon(\hat{\omega}) > 0$ is a small imaginary part that would cause the corresponding unforced resonance to decay in amplitude like $\mathrm{e}^{-\epsilon t}$. According to Devin [11], the separate contributions to ϵ from radiation, viscous and thermal damping are all of comparable magnitudes. We can evaluate the effect of radiation from the solution (2.12), (2.13) which takes account of the compressibility of the water, i.e. from the solutions of $Z_{2n}(k_o a) - 1 = 0$:

$$\frac{\rho_w c_w}{\rho_o c_o} \frac{j_{2n}'(k_o a)}{j_{2n}(k_o a)} \frac{h_{2n}^{(1)}(k_w a)}{h_{2n}^{(1)\prime}(k_w a)} = 1, \quad \text{where } \; k_o = \frac{\omega}{c_o}, \quad k_w = \frac{\omega}{c_w}. \tag{2.24}$$

It will be sufficient to consider the damping of the monopole modes ($n = 0$), and in particular the dominant pulsational mode, for which $\hat{\omega} a/c_o \equiv \hat{k}_o a \approx 0.06$ ($N = 1$ in Table 2.1). By setting $n = 0$ in equation (2.24) we derive the analogue of the undamped frequency equation (2.22)

$$k_o a - \left(1 - \frac{\rho_o}{\rho_w} + i k_o a \, \frac{\rho_o c_o}{\rho_w c_w}\right) \tan(k_o a) = 0, \tag{2.25}$$

from which the compressible correction to the Minnaert approximation is readily deduced to be:

$$k_o a \approx \hat{k}_o a \left(1 - i \, \frac{c_o \hat{k}_o a}{2 c_w}\right), \quad \text{where} \quad \hat{k}_o a = \sqrt{\frac{3\rho_o}{\rho_w}}. \tag{2.26}$$

Therefore the minimum complex frequency of volumetric resonances is given by

$$\omega = \frac{c_o}{a} \sqrt{\frac{3\rho_o}{\rho_w}} - i\epsilon, \qquad \epsilon = \frac{c_o^2 (\hat{k}_o a)^2}{2 c_w a}, \tag{2.27}$$

where $\hat{k}_o a \approx 0.06$ (Table 2.1).

This estimate of the radiation damping coefficient ϵ should be characteristic of the damping also expected from viscous and thermal losses. However, it is important that it be compared with the hydrodynamic damping produced by the efflux of gas from the 'rear' of the cavity. This is determined by the following argument.

Let $\mathcal{E}$ denote the mean energy density (per unit volume) of the resonance mode within the cavity. The rate at which energy of this mode is removed from the cavity by convection in the gas exhausting into the water is $Q\mathcal{E}$, where Q is the volume velocity of the exhausting gas, which is the same as the volume inflow rate in the jet. Hence, if $V = \frac{4}{3}\pi a^3$ is the cavity volume, the net monopole energy $V\mathcal{E}$ within the cavity decays at a rate determined by

$$\frac{d\mathcal{E}}{dt} = -\frac{Q\mathcal{E}}{V}. \tag{2.28}$$

But $\mathcal{E} \sim |p|^2/\rho_o c_o^2$ and $d|p|^2/dt = -2\epsilon|p|^2$, where ϵ is the corresponding imaginary part of the resonance frequency associated with hydrodynamic damping, i.e. $\epsilon = Q/2V$.

Hence, from (2.27), (2.28)

$$\frac{\epsilon_{\text{hydrodynamic}}}{\epsilon_{\text{radiation}}} \sim \frac{Q/V}{c_o^2(\hat{k}_o a)^2/c_w a}. \tag{2.29}$$

The typical gas inflow rate $Q \sim 0.01\,\text{m}^3/\text{s}$ for our notional experimental supercavity whose volume is the same as that of a sphere of radius $a = 7\,\text{cm}$, Taking $\hat{k}_o a = 0.06$ and using STP values for the other quantities in (2.29), we deduce that

$$\frac{\epsilon_{\text{hydrodynamic}}}{\epsilon_{\text{radiation}}} \sim 0.02,$$

and therefore that the steady efflux of gas into the water has no significant impact on damping.

This conclusion is doubly true for higher frequency modes which radiate more freely into the water. The implication is that the acoustic properties of the cavity are not significantly influenced by the gaseous exhaust. This is evidently a consequence of pressure continuity across the cavity interface and in the exhaust flow.

2.2.3 Quadrupole resonances

The case $n = 1$ in equation (2.13) represents a radiation field of quadrupole directivity. The corresponding resonance frequencies when the compressibility of the water is neglected are determined by setting $n = 1$ in equation (2.21), i.e. by the roots of

$$(k_o a)^3 - 9k_o a\left(1 - \frac{\rho_o}{\rho_w}\right) + \left(9 - 4(k_o a)^2 - \frac{3\rho_o}{\rho_w}\Big(3 - (k_o a)^2\Big)\right)\tan(k_o a) = 0. \tag{2.30}$$

The length scales of these wave modes within the cavity are no larger than the cavity diameter. Indeed it is readily confirmed by expansion of the equation in powers $k_o a$ that there are no solutions satisfying $|k_o a| \ll 1$. Numerical solution of equation (2.30) yields the results in Table 2.2, where the frequencies tabulated in the third line are for a 7 cm spherical air cavity.

mode number N	1	2	3	4	5	6	7	8
$k_o a$	3.34	7.29	10.61	13.85	17.04	20.22	23.39	26.55
frequency Hz	2,585	5,636	8,205	10,704	13,175	15,632	18,082	20,526

Table 2.2. Cavity quadrupole wavenumbers and frequencies at STP (from Eq. (2.30))

Similar analyses of the resonances can be performed for the higher order modes ($n > 1$ in equations (2.12), (2.13)), but it is not necessary to present details here. It is clear that the principal low frequency resonances occur for $k_o a > 1$, the only exception being the special case of the Minnaert monopole. Experiments on cavitating jets all indicate that the far field acoustic spectrum peaks in the neighborhood of a frequency comparable to the Minnaert frequency [6, 7] and typically decays like ω^{-2} at higher frequencies. Our results indicate a similar behavior for the cavity (the corresponding continuum spectrum being formed by the aggregate contributions from the cavity resonances) although the precise details for the spherical cavity and for a practical ventilated supercavity depend on the frequency dependence of the appropriate jet forcing function $F_o(\omega)$.

2.3 Directivity of the sound

The acoustic far field in the water satisfies $k_w r \gg 1$. In this limit the asymptotic approximation $h_n^{(1)}(z) \approx (-i)^{n+1}\mathrm{e}^{iz}/z$ permits the reduction of equation (2.13) to the form

$$p(r,\theta,\omega) \approx -\frac{iF_o\mathrm{e}^{-i\omega(t-r/c_w)}}{k_w ar}\sum_{n=0}^{\infty}\frac{A_n\, Z_{2n}P_{2n}(\cos\theta)}{(Z_{2n}-1)h_{2n}^{(1)}(k_w a)}, \quad k_w r \to \infty, \tag{2.31}$$

where $A_n = (4n+1)(2n)!/\{2^{(2n+1)}(n!)^2\}$. Therefore

$$\left|\frac{p(r,\theta,\omega)}{F_o/a}\right|^2 \approx \frac{1}{(k_w r)^2}\left|\sum_{n,m=0}^{\infty}\frac{A_n A_m Z_{2n}Z_{2m}P_{2n}(\cos\theta)P_{2m}(\cos\theta)}{(Z_{2n}-1)(Z_{2m}-1)h_{2n}^{(1)}(k_w a)h_{2m}^{(1)}(k_w a)}\right|, \; k_w r \to \infty. \tag{2.32}$$

This formula determines the directivity ($\propto |p(r,\theta,\omega)|^2$) of the sound radiated into the water. The directivity is plotted as a function of θ in Fig. 2.2 (on a polar plot, each curve being normalized with respect to its maximum value) for a cavity filled with air at standard temperature and pressure when $k_w a = 0.1,\ 1,\ 10,\ 100$. The field shape is spherically symmetric at very low frequencies ($k_w a < 0.1$) characteristic of the Minnaert monopole. As the frequency increases (for $k_w a$ greater than about 10, i.e. for frequencies exceeding 38,600 Hz for a spherical cavity of radius 7 cm) the sound exhibits a progressive tendency to radiate preferentially in the side-line direction with the directivity of the principal side lobe being approximately $\sin^2\theta$, i.e. that of an axisymmetric dipole with axis along the radial direction of the jet.

This dipole radiation is accompanied by narrow beams radiated in the fore and aft directions ($\theta = 0,\ \pi$). The presence of these beams appears to be an artifact of the spherical geometry, and would likely be absent for the more realistic geometries, such as that of the ‘cigar’ shaped cavity illustrated in Figure 1.1, because the interface is effectively equivalent to a ‘pressure release’ surface along which sound cannot propagate.

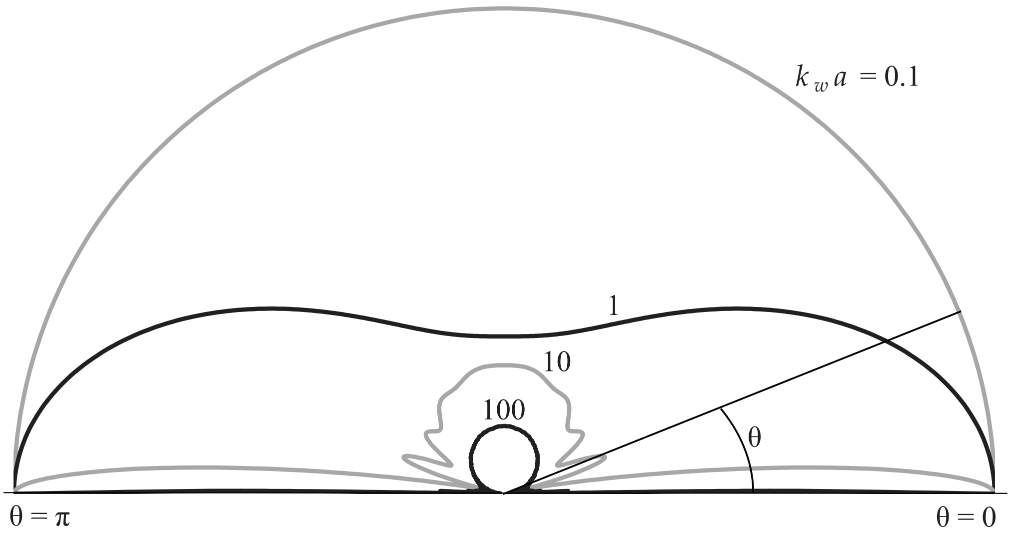

Figure 2.2. Directivity of the jet-excited sound for the general case of an air-filled spherical cavity at STP determined by Eq. (2.32) when $k_w a = 0.1, 1, 10, 100$. Each curve is normalized with respect to its peak value.

This is illustrated by reference to the exact analytical solution for the case of a two-dimensional jet impinging on a plane interface (Figure 2.3).

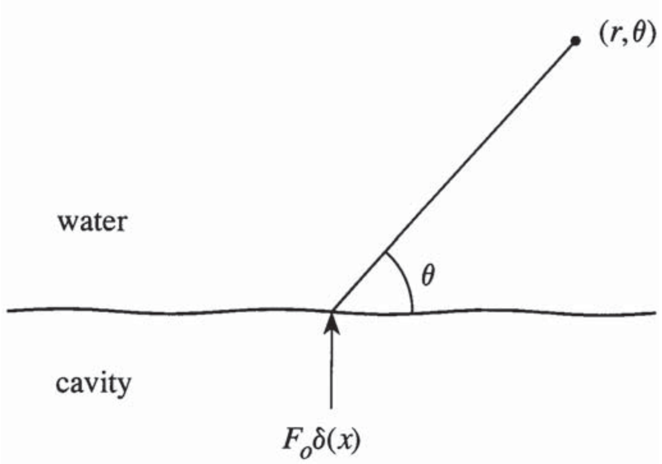

Figure 2.3. The problem of the sound produced by a two-dimensional jet impinging on a nominally plane interface

For the simplest condition in which the pressure in the cavity (the lower region in Figure 2.3) is negligible, the pressure radiated into the water consists entirely of the dipole field

$$p(r,\theta,\omega) \sim \frac{-F_o\sqrt{k_w}\sin\theta\, \mathrm{e}^{i\{k_w r-\pi/4\}}}{\sqrt{2\pi r}}, \quad k_w r \to \infty \tag{2.33}$$

where angle θ is defined as in Figure 2.3. Therefore, to better visualize the emergence of the dipole we plot the directivity (again, $\propto |p(r,\theta,\omega)|^2$) of the sound normalized with respect to its value at $\theta = \frac{\pi}{2}$, clipping the beams in the fore and aft directions, as in Figure 2.4.

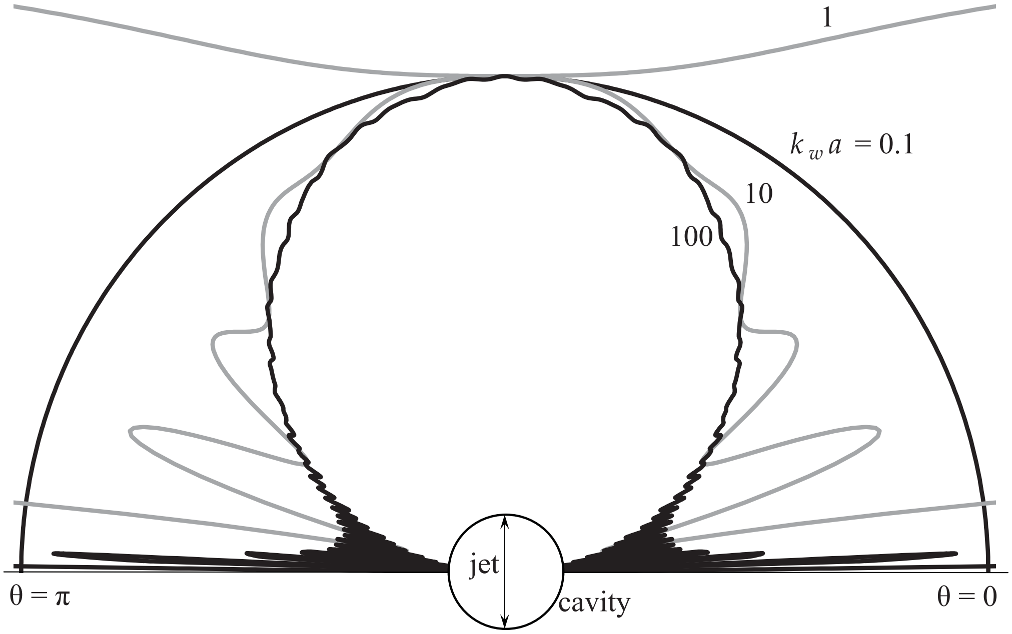

Figure 2.4. Directivity of the jet-excited sound for the general case of an air-filled spherical cavity at STP determined by Eq. (2.32) when $k_w a$ = 0.1, 1, 10, 100. Each curve is normalized with respect to its value at $\theta = \frac{\pi}{2}$.

It is also of interest to compare these predictions with those for two of the special cases discussed in §2.1.3 and §2.1.4. In §2.1.4 the effect on sound generation of wave incoherence produced by a randomly irregular cavity interface is modeled by the formal neglect of pressure waves incident on the interface from within the cavity. In this case $|p(r,\theta,\omega)|^2$ in the far field is given by equation (2.32) with $Z_{2n,2m}$ replaced by $\hat{Z}_{2n,2m}$ defined in equation (2.16). The corresponding directivities (in Fig. 2.5) are seen to be hardly changed from those predicted from equation (2.32) for the full solution, indicating that the directivity of high frequency resonances are essentially unaffected by 'wrinkling' of the cavity interface.

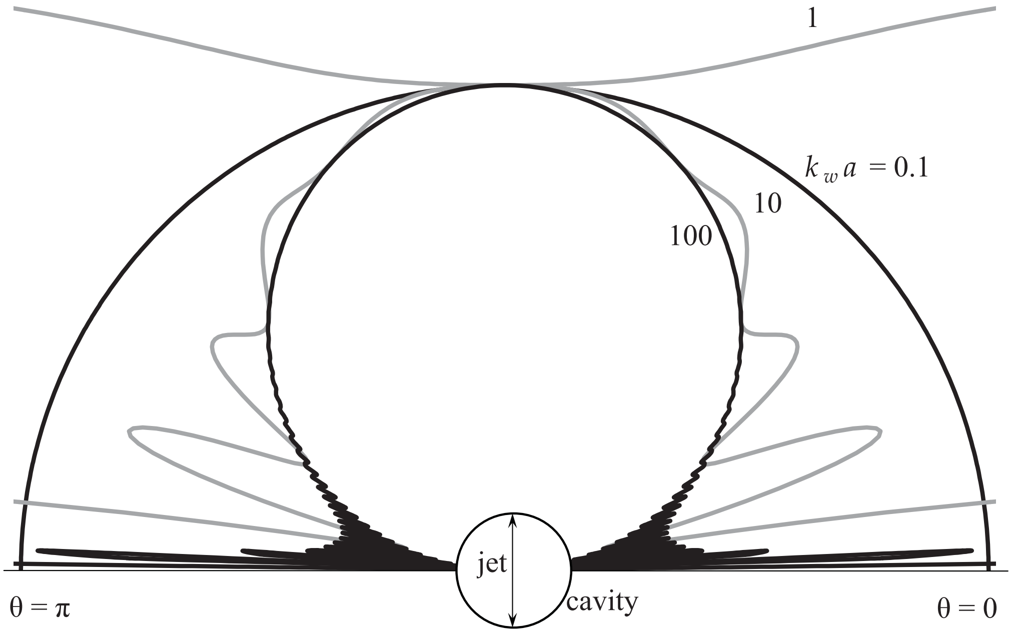

Figure 2.5. Directivity of the jet-excited sound when the correction of Eq. (2.16) is introduced into (2.32) to account for incoherent reflection of waves from the interface, for an air-filled spherical cavity at STP when $k_w a = 0.1$, 1, 10, 100. Each curve is normalized with respect to its value at $\theta = \frac{\pi}{2}$.

Second, in case (ii) of §2.1.3 pressure variations within the cavity are absent (a 'vacuous' cavity interior). It now follows from equation (2.17) that

$$\left|\frac{p(r,\theta,\omega)}{F_o/a}\right|^2 \approx \frac{1}{(k_w r)^2}\left|\sum_{n,m=0}^{\infty}\frac{A_n A_m P_{2n}(\cos\theta)P_{2m}(\cos\theta)}{h_{2n}^{(1)}(k_w a)h_{2m}^{(1)}(k_w a)}\right|, \quad k_w r \to \infty. \tag{2.34}$$

Again, the typical field shapes plotted in Fig.2.6 are effectively identical with the corresponding plots for the full solution.

This agreement occurs because, except at the resonance frequency, $Z_{2n}/(Z_{2n}-1) \sim \hat{Z}_{2n}/(\hat{Z}_{2n-1}) \sim 1$ when $\rho_w \gg \rho_o$. This conclusion has been confirmed (and the accuracy of the numerical procedure validated) by recalculating the directivities for the fully com-

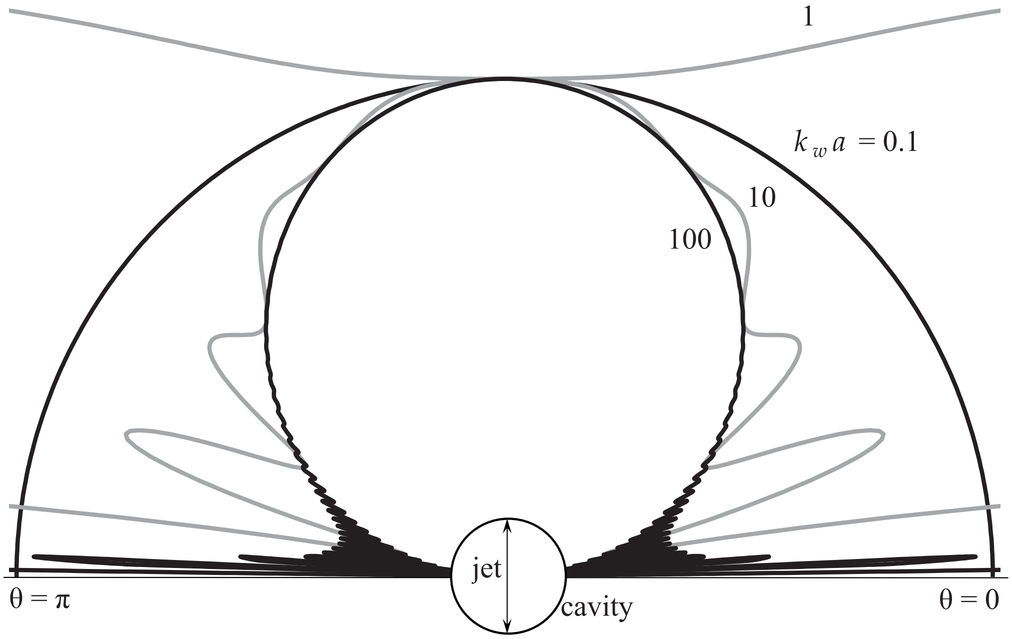

Figure 2.6. Directivity of the jet-excited sound in case (ii) of §2.1.3 (a 'vacuous' cavity interior) determined by Eq. (2.34) when $k_w a = 0.1$, 1, 10, 100. Each curve is normalized with respect to its value at $\theta = \frac{\pi}{2}$.

pressible cavity for the case of §2.1.4 of incoherent interface scattering in cases where $\rho_o \sim \rho_w$ (but with unchanged values of c_o and c_w). The resulting directivities are consistently found to be *different* from each other, and also different from the results in Figs.2.4 - 2.6 for an air filled cavity.

2.4 Conclusions

The low frequency sound radiated by the spherical model of a supercavity is dominated by the volumetric monopole modes excited by the jet. The amplitudes of motions near the cavity are controlled by damping produced by the sound radiation, by viscous and thermal losses in the cavity, and by the steady hydrodynamic flow of gas from the 'rear end' of the cavity. For all frequencies of practical interest, the continuity of pressure across the cavity interface and within the exhaust flow ensures that the hydrodynamic damping is negligible, and therefore that the acoustics of the system are effectively unaffected by the gas exhaust flow.

The radiation from the cavity is omnidirectional at low frequencies, comparable to the Minnaert frequency of the dominant monopole. As the frequency increases the radiation directivity develops a principal side-lobe equivalent to that produced by a dipole acoustic source with axis along the radial direction of the gas jet impinging on the interface. Our numerical results for the spherical cavity with a jet impinging at $\theta = \frac{\pi}{2}$ to the nominal direction of the mean water flow indicate that this dipole radiation (of directivity $\sim \sin^2\theta$) is accompanied by narrow beams radiated in the fore and aft directions ($\theta = 0,\ \pi$). These beams are an artifact of the spherical geometry that is likely to be absent in more realistic cavity geometries.

The theoretical results for the spherical cavity indicate that the side-line dipole is well formed when $k_w a > 10$. For the more general cavity this suggests that the dipole becomes prominent at frequencies exceeding about $1.5c_w/\mathcal{R}\,\mathrm{Hz}$, where $\mathcal{R}$ is the mean radius of curvature of the interface at the point of impact of the jet. At such frequencies, the self-noise generated by the gas jet might be expected to have a negligible influence on control systems situated forward of the cavitator.

Chapter 3

Analytical model for jet impingement on a plane interface

This chapter describes the sound generated by a circular jet of small cross-section impinging on a planar interface. We consider the scale-model vehicle depicted in Figure 1.1. Ventilating gas is injected into the cavity via an axisymmetric ring of twenty radiating jets which impinge on the cavity wall at normal incidence. Each jet impact is discreet and will be considered as an independent source of sound. Given that each jet is identical and the injection ring, vehicle, and supercavity are all axisymmetric, it is therefore only necessary to compute the sound generated by the impingement of a single jet.

Next we consider that the estimated radius of curvature of the supercavity is more than three times the diameter of the jet impact area, D. Furthermore, at the highest frequencies ω of interest, $k_w D \sim 1$, where acoustic wavenumber $k_w = \omega/c_w$ and c_w is the speed of sound in water, so we will approximate the source as being acoustically *compact* (see Appendix B). We can therefore approximate the site of the jet impact on the cavity wall as locally plane, and the jet to be of infinitesimal thickness. As with the sphere problem of the previous chapter, these simplifications eliminate difficulties associated with a more realistic cavity geometry. The predicted pressure field and its expression in terms of the frequency spectrum of the force applied by the jet on the wall is determined.

3.1 Pressure fluctuations in the water

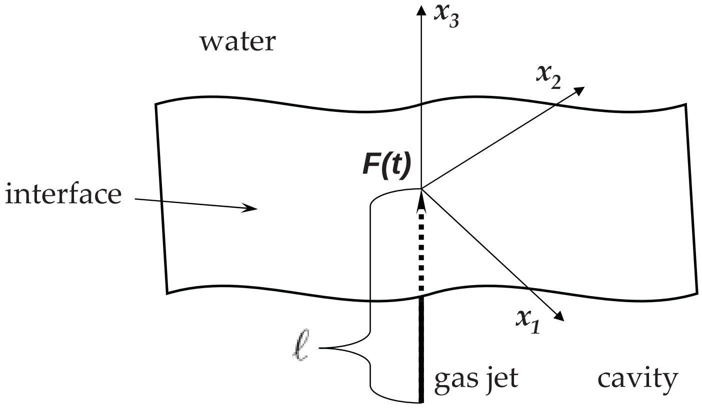

Figure 3.1. Problem of a jet of infinitesimal cross-section impinging on a gas-water interface

Let the mean position of the gas-water interface coincide with the plane $x_3 = 0$ of the rectangular coordinate system $\mathbf{x} = (x_1, x_2, x_3)$, with water of density ρ_w and sound speed c_w occupying the region $x_3 > 0$ (Fig. 3.1). The Mach number of the mean flow of water over the interface is assumed to be sufficiently small that the convection of sound can be ignored. Small amplitude fluctuations in the pressure $p(\mathbf{x}, t)$ (where t denotes time) may therefore be taken to satisfy

$$\left(\frac{1}{c_w^2}\frac{\partial^2}{\partial t^2} - \nabla^2\right) p = 0, \qquad x_3 > 0, \tag{3.1}$$

provided that turbulence sources of ‘noise’ within the flow are ignored [18].

A circular gas jet which is coaxial with the x_3 axis is incident normally on the interface from within the cavity $x_3 < 0$. The jet exhausts at mean speed U_o from a circular nozzle of radius R_o whose exit plane is at $x_3 = -\ell$ (where $R_o \ll \ell$). The unsteady force $F(t)$, say, exerted by the jet on the interface is distributed over a circularly symmetric region of the x_1x_2-plane centered on the origin of nominal effective radius $R \ll \ell$. This force excites unsteady motions and pressure fluctuations within the water. When attention is confined to the unsteady motions occurring at distances $|\mathbf{x}| \gg R$ and when, in addition, the relevant acoustic wavelengths are much larger than R, it is permissible for the purposes of calculation to assume that $F(t)$ is concentrated at the origin, and corresponds to a singular distribution of applied surface pressure equal to $F(t)\delta(x_1)\delta(x_2)$. Furthermore, the very large differences in the mean gas and water densities implies that to an excellent approximation pressure fluctuations occurring elsewhere on the interface can be ignored (for further discussion of this approximation see Chapter 2). The solution of equation (3.1) is therefore required in $x_3 > 0$ subject to the condition

$$p = F(t)\delta(x_1)\delta(x_2) \quad \text{on } x_3 = 0. \tag{3.2}$$

To determine p we introduce a Green's function $G(\mathbf{x}, \mathbf{y}, t - \tau)$ defined by

$$\begin{aligned} G(\mathbf{x}, \mathbf{y}, t-\tau) \;=\; & \frac{1}{4\pi|\mathbf{x}-\mathbf{y}|}\,\delta\left(t - \tau - \frac{|\mathbf{x}-\mathbf{y}|}{c_w}\right) \\ & - \frac{1}{4\pi|\mathbf{x}-\bar{\mathbf{y}}|}\,\delta\left(t - \tau - \frac{|\mathbf{x}-\bar{\mathbf{y}}|}{c_w}\right) \end{aligned} \tag{3.3}$$

where $\bar{\mathbf{y}} = (y_1, y_2, -y_3)$ is the 'image' of the point $\mathbf{y}$ in the plane of the interface. The Green's function vanishes when either of $x_3,\ y_3$ lies on the interface, and satisfies

$$\left(\frac{1}{c_o^2}\frac{\partial^2}{\partial t^2} - \nabla^2\right) G = \delta(\mathbf{x}-\mathbf{y})\delta(t-\tau), \quad x_3,\ y_3 > 0, \tag{3.4}$$

where $G = 0$ for $t < \tau$ (see Appendix B for a brief discussion of the derivation and use of Green's functions).

The application of Green's theorem and the radiation condition (see Appendices A and B) to Eqs. (3.1), (3.4) now permits the pressure in $x_3 > 0$ to be expressed in the form [2, 6, 10, 29]

$$\begin{aligned} p(\mathbf{x},t) &= \oint_{\mathrm{S}} \Big(p(\mathbf{y},\tau)\frac{\partial G}{\partial y_3}(\mathbf{x},\mathbf{y},t-\tau) \\ &\qquad -G(\mathbf{x},\mathbf{y},t-\tau)\frac{\partial p}{\partial y_3}(\mathbf{y},\tau)\Big)\, dy_1 dy_2 d\tau \end{aligned} \tag{3.5}$$

where the integration is over all values of the retarded time $-\infty < \tau < +\infty$, and the surface integral is over the cavity interface S: $y_3 = +0$.

Substituting into the integrand from Eqs.(3.2), (3.3), we find that both the near and far field pressure fluctuations in the water are given without further approximation by the dipole formula

$$p(\mathbf{x},t) = -\frac{\partial}{\partial x_3}\left[\frac{1}{2\pi|\mathbf{x}|}F\left(t-\frac{|\mathbf{x}|}{c_w}\right)\right], \quad x_3 > 0. \tag{3.6}$$

3.2 The pressure spectrum

It will be assumed that the unsteady component of the jet impact force $F(t)$ (the net force minus the mean force) is stationary random with frequency spectrum

$$\Phi_{FF}(\omega) = \frac{1}{2\pi}\int_{-\infty}^{\infty}\langle F(t)F(t+\tau)\rangle\, \mathrm{e}^{i\omega\tau}\, d\tau \tag{3.7}$$

where the angle brackets $\langle\ \rangle$ denote an ensemble or time average. Then (3.6) implies that the corresponding pressure spectrum $\Phi_{pp}(\mathbf{x},\omega)$ in the water is given by

$$\begin{aligned}\Phi_{pp}(\mathbf{x},\omega) &= \Phi_{FF}(\omega)\left|\frac{\partial}{\partial x_3}\left(\frac{\mathrm{e}^{ik_o|\mathbf{x}|}}{2\pi|\mathbf{x}|}\right)\right|^2 \\ &\equiv \frac{\Phi_{FF}(\omega)}{4\pi^2}\frac{\cos^2\theta}{|\mathbf{x}|^4}\Big(1+k_w^2|\mathbf{x}|^2\Big), \quad x_3>0, \end{aligned} \tag{3.8}$$

where $\cos\theta = x_3/|\mathbf{x}|$ determines the dipolar directional characteristics of both the near and far pressure fields in the water, and $k_w = \omega/c_w$ is the acoustic wavenumber, and

$$\Phi_{pp}(\mathbf{x},\omega) = \frac{1}{2\pi}\int_{-\infty}^{\infty}\langle p(\mathbf{x},t)p(\mathbf{x},t+\tau)\rangle\,\mathrm{e}^{i\omega\tau}\,d\tau. \tag{3.9}$$

Equation 3.8 determines the pressure spectrum at $\mathbf{x}$ in the water in terms of the spectrum of the impact force of the jet. In the next chapter, this formula will be used to approximate the spectrum of the water-borne sound generated by the experimental vehicle (Figure 1.1) by determination of the impact force spectrum Φ_{FF} exerted by one of the vehicle's jets.

Chapter 4

Jet impingement experiment

This chapter describes a canonical experiment performed to determine the frequency spectrum Φ_{FF} of the interaction force for a single jet impinging on an interface. We again consider the vehicle depicted in Figure 1.1. The ventilating gas enters the cavity axisymmetrically through twenty radially orientated nozzles equally spaced on a gas injector ring close to the cavitator. Each jet impinges on the cavity interface at close to normal incidence. In the impact region, turbulence and other water-borne disturbances such as bubbles are rapidly convected away over a pressure release interface by the mean flow of water outside the experimental cavity and exert a negligible surface force and, therefore, are expected to have no effective influence on acoustic generation and transmission. The wakes behind the ridges in the cavity created by the impinging jets (see Fig. 1.3) are not acoustic sources because they convect along with the mean flow velocity and exert no pressure on the water. Forces exerted by turbulence and bubbles convecting over these wakes are identically canceled by equal and opposite images inside the cavity (see Appendix B). Therefore, the dominant acoustic source associated with ventilation jet impingement is the unsteady fluctuations of the cavity wall in the jet impact region.

The sound produced by these interactions is determined principally by the unsteady forces exerted on the water at the interface by the impinging jets. In practice the ventilating jets are fully turbulent on impact with the interface, and the properties of the sound depend on the spectral content of the surface force. Typical gas speeds on impact do not normally exceed $\sim 60\,\mathrm{m/s}$. In these circumstances the very large difference in the densities of the gas and water permit the interface to be regarded as *rigid* in a first approximation. The unsteady impact force of the jet may then be identified with that obtained when a jet is allowed to impinge on a rigid plate. To exploit this analogy one of the ventilating jets of the test vehicle was directed at normal incidence onto the plate-like measurement surface of a rigidly-fixed force transducer. Though made slightly awkward by the vehicle body and mounting system, this method allowed us to capture the properties and frequency dependence of the vehicle jet due to its unique orifice and injection system, details which may be lost when using a simpler, stand-alone jet nozzle. The spectrum of the exerted force was measured for a range of gas injection flow rates and jet lengths. The results of these tests were used with the formulae determined in Chapter 3 to make predictions for the sound generated by jet impingement on a planar interface.

As discussed in Section 1.2, a literature survey revealed that investigations of the acoustics of jet impingement [28, 34, 40] have focused on impingement on a plate and on acoustic sources such as shed vorticity or turbulence; no work appears to have been done on the acoustics of a jet impinging on an unsteady, free gas-water interface. Furthermore, no examples of the direct measurement of the unsteady force exerted by an impinging jet were found. Thus the few existing studies of relevance are those which provide information about the exerted pressure. Strong *et al.* [45] describe an experiment in which a jet was directed at a flat plate at various angles of incidence. Two surface pinhole microphones were used to measure the correlation spectrum of the fluctuating surface pressure on the plate. Their measurements for normal incidence are compared in this chapter with our experimental results for the surface force spectrum on the flat force transducer. We also compare predictions of the impingement-generated sound using the data from [45] with our predictions for the supercavity.

The first section (4.1) describes the supercavitating vehicle experimental setup. Section 4.2 recounts the experimental method and executed trials. Data analysis and uncertainty in the results are discussed in Section 4.3. Results for the exerted force spectra are presented in Section 4.4. Using these results, predictions are made in Section 4.5 for the sound generated by jet impingement on a planar interface and compared with corresponding predictions based on the results of Strong *et al.* [45] in Section 4.6. Conclusions are then inferred for the sound generated by jet impingement on a more realistic, cylindrical cavity interface.

4.1 Experimental setup

Testing was conducted at the Garfield Thomas Water Tunnel facility at ARL using a single ventilating jet of a 76 mm body-diameter experimental supercavitating vehicle like that depicted in Figures 1.1 and 1.2. In normal operation the vehicle is rigidly mounted in an ARL 0.305 m water tunnel test section (see Appendix C). Gas is injected into the cavity axisymmetrically via a ring of 20 identical, radially directed jets. The diameter of the exit orifice for each jet is 1.6 mm, and the exit planes are evenly distributed in a ring of radius 25 mm centered on the axis of symmetry of the vehicle.

Gas enters the system by way of a line passing through the vehicle mounting strut (Fig. 4.1). A line from each of six bottles of compressed gas is connected to a manifold where the separate supplies are combined into single gas line. A seventh bottle of compressed air provides a constant back pressure to this gas line at the manifold so that a constant flow rate of gas to the vehicle can be maintained as the supply bottles empty. A ball valve in the supply line allows for rapid on/off control of the gas flow to the vehicle when the bottles are open and feeding the line. The gas flow rate through the system is monitored by a flow meter upstream of the ball valve, and is varied by adjustment of the ball valve aperture.

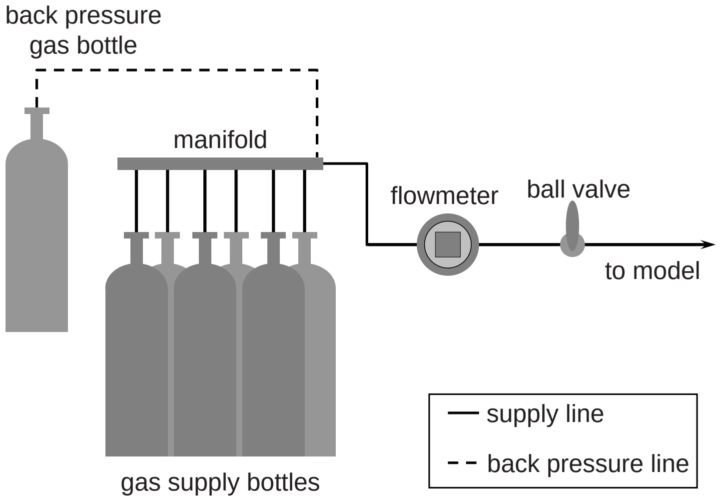

Figure 4.1. Schematic of gas injection system

The model vehicle, without the cavitating nose section which was not required for this experiment, was secured to a bench top. The gas injection system described above was connected to the vehicle. Four of the jet orifices were plugged with wax held in place with firmly fixed electrical tape, two each immediately clockwise and anti-clockwise of the 'test' jet (see Fig 4.2). Though this increased the net flow through the remaining open orifices by approximately 25% (relative to typical running conditions with all jets operating), it was important to do this in order to isolate a single jet for measurement. This isolated test jet was directed at normal incidence onto the 12.7 mm diameter measurement surface of a *PCB* ICP dynamic force transducer (Fig. 4.3).

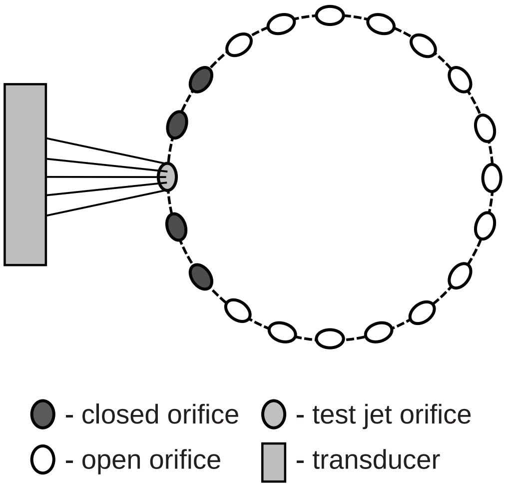

Figure 4.2. Arrangement of open and closed jet orifices

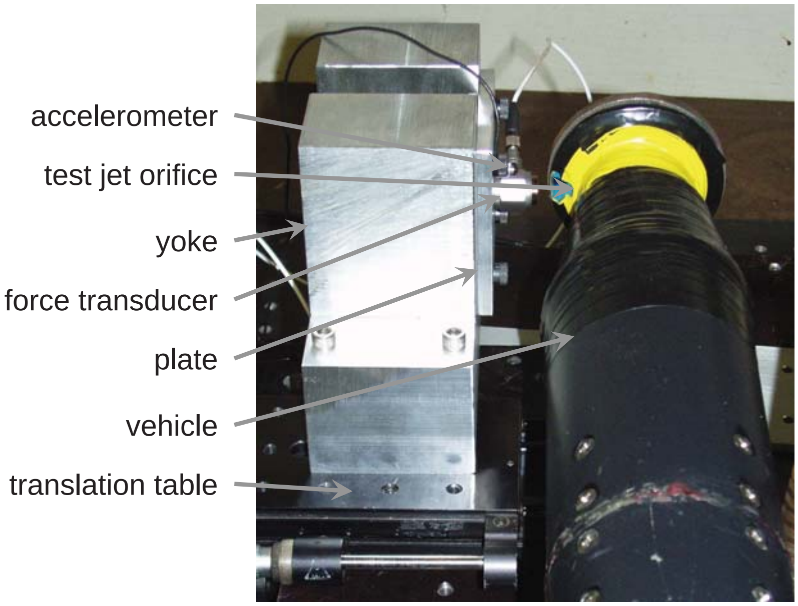

Figure 4.3. Experimental setup. The vehicle's nose section, unnecessary for this experiment, has been removed. In this photograph, only the test jet is exposed; the other fifteen jets were subsequently unsealed as in Fig. 4.2 before testing was conducted.

The force transducer was fixed at the center of a 6.35 mm thick 76.2 mm square aluminum plate (Fig. 4.4). The plate was screwed onto a 127 mm tall heavy aluminum yoke made massive in an effort to reduce structural vibrations induced by the impacting jet (Fig. 4.5). The yoke was fastened on a 1-axis, 0.25 mm resolution translation table mounted on the bench top. The axis of the translation table was parallel with the center axis of the jet allowing for adjustment of the length of the test jet, defined to be the distance between the jet orifice and the wetted surface of the transducer. Superglue was used to fix an accelerometer to the plate, in close proximity with the transducer.

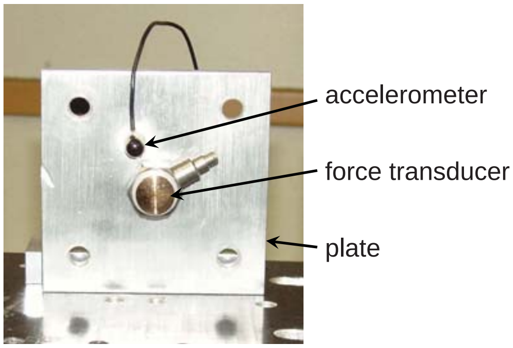

Figure 4.4. Plate and transducer assembly. The force transducer was threaded into the center of the plate. The accelerometer fixed with superglue.

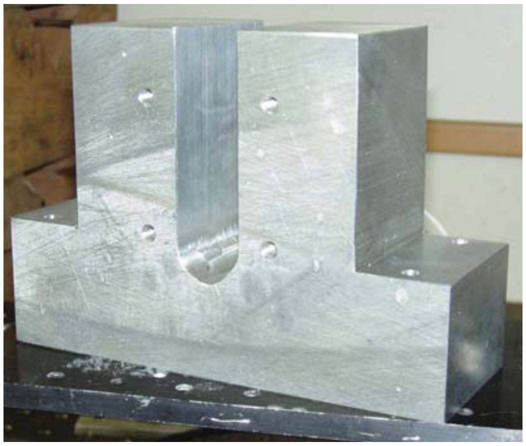

Figure 4.5. Massive yoke used for mounting of plate and transducer assembly

4.2 Methods

The *PCB* dynamic force sensor directly measured the unsteady force exerted by the test jet. Pertinent specifications for this and all of the electronic equipment used are presented in Appendix D. The force transducer was calibrated using a set of known masses. This piezoelectric transducer cannot measure static loads, so the calibration technique, similar to that used by the manufacturer, consisted of securing the transducer to the benchtop with its measurement surface horizontal (*i.e.* facing upward), resting a mass on the transducer, and measuring the output voltage when the mass was quickly removed. This was executed three times each for masses between 0.05 and 2 kg. Assuming the force exerted on the transducer by each mass was its weight, mg, these data and the resulting calibration curve are shown in Figure 4.6. The calibration curve was fitted to the data using the method of linear-least-squares.

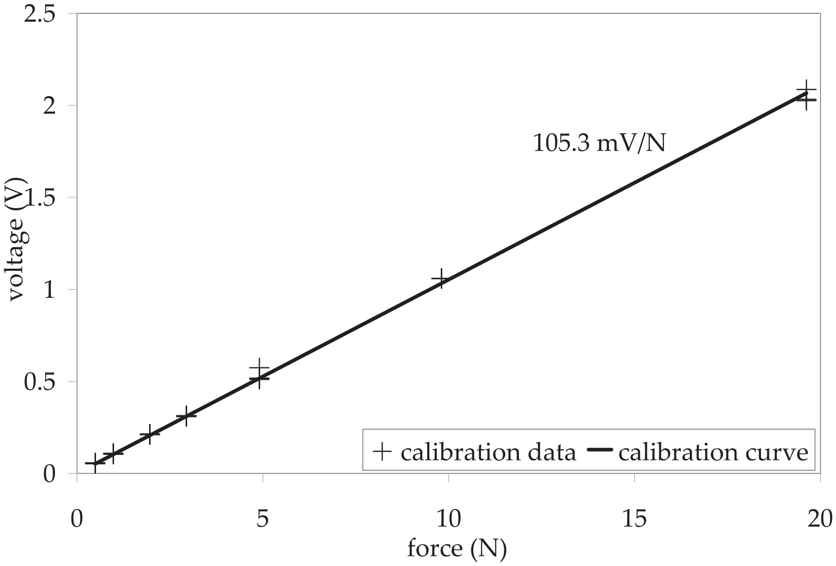

Figure 4.6. Calibration data for unsteady force transducer

The accelerometer was used to measure the structural vibrations of the plate generated from both the test environment and the jet impact. Assuming a rigid mounting (the force transducer was threaded tightly onto the plate), this vibration is taken to be that experienced by the force transducer housing. The accelerometer was calibrated using a *PCB* 394C06 hand held 1-g shaker. The shaker is an oscillating piston which accelerates the transducer at 1 g. The accelerometer was fixed to the shaker and the amplitude of its output voltage recorded. This was repeated three times and the results averaged, yielding a sensitivity of 14.566 mV/g.

The signals from the force transducer and accelerometer were fed through a PCB 480B21 signal conditioner, applying a gain of 10 to both the force sensor signal and the accelerometer signal. The signals were then passed to a *DSP* SigLab 50-21 data acquisition system. This system was connected to a laptop computer with accompanying SigLab software used to record and process each signal. The software applied a fast-Fourier transform (FFT) of 8192 points to 64 ms samples of the time series of each signal to produce an autocorrelation spectrum with units of root-mean-square (RMS) voltage squared in 15.6 Hz bins up to 50 kHz (see Bendat and Piersol [3] for a discussion of the theory and application of spectral functions). An *ensemble* of 60 of these spectra were averaged to produce a final resultant spectrum. Cross-correlation spectra between the force sensor and accelerometer signals were also generated using the same transform and averaging parameters.

Measurements were made for a variety of jet lengths ℓ and gas injection volume flow rates Q. A complete list of trial parameters is given in Table 4.1. Typical experimental injection rates for the model test vehicle are 0.0047, 0.0071, and 0.0094 m^3/s, producing jet lengths of approximately 35 mm. A range of lengths around this median value were tested to study the effect of jet length on the spectrum of the applied force and the produced sound. For the shorter of these jet lengths, 15 and 20 mm, the entire impact area of the jet lies within the face of the force transducer, assuming a jet spread half-angle of 12.5° [29] and finding the diameter D of the jet cross-section

$$D = 2(R_o + \ell \tan(12.5^\circ)), \tag{4.1}$$

in terms of the radius of the jet orifice R_o and jet length ℓ (see Figure 4.7). Longer jet lengths have cross-sections on impact larger than the force transducer measurement surface. However, the bulk of the force exerted by a jet is produced by the flow in the vicinity of the jet centerline, inferred by the variation of longitudinal velocity with radial distance from the jet's central axis. If the jet's velocity drops off rapidly above $0.4a$ from the centerline [29], we estimate from (4.1) that the force transducer is large enough to capture the bulk of the force exerted by a jet up to 64 mm in length. It was therefore assumed that for our jets of length > 20 mm, the force measured by the transducer is a sufficient approximation to the force exerted over the entire impact area. Comparison of the measured force spectra for the longer jet lengths with those for jet lengths of 15 and 20 mm will demonstrate the appropriateness of this assertion and the magnitude of any introduced error.

ℓ (mm)	Q (m^3/s) $\times 10^4$
15	47, 71, 94
20	47, 71, 94
25	47, 71, 94
30	47, 71, 94
35	47, 71, 94
40	47, 71, 94
45	47, 71, 94

Table 4.1. Schedule of experimental trials

Each trial was repeated three times. In addition, the centerline jet exit velocity U_o at the jet orifice was measured for a jet injection rate of $Q = 0.0047$ m/s using a *TSI* VelociCalc probe air velocity meter. Direct measurement of the exit velocity for the higher injection rates was not possible because of the limitations imposed by the

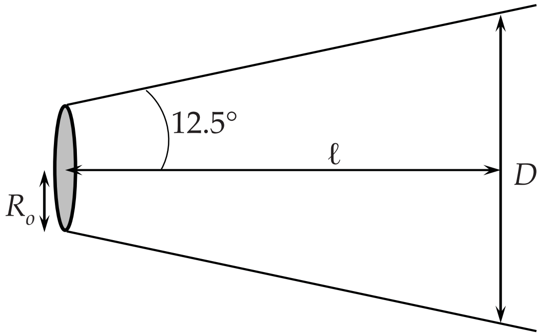

Figure 4.7. Estimated shape of a fully turbulent jet

velocimeter's usable range; these values will be interpolated from the lower injection rate measurement using fluid dynamic theory. To make the measurement, the probe tip was inserted into the center of the jet approximately 1 mm downstream of the jet orifice. The VelociCalc is calibrated annually by the manufacturer, and the measurement was repeated three times to account for statistical variability. The device is also equipped with a temperature probe which was used to measure the ambient air temperature and that of the jet at the jet orifice employing the same technique.

4.3 Data analysis

4.3.1 Post-processing

The determined calibration factor for each transducer was applied during post-processing to convert the measured autocorrelation spectra from units of RMS voltage squared into units of squared force (N^2) or acceleration (g^2) and the cross-correlation spectra from units of RMS voltage squared into units of force×acceleration, N-g's. Applying a method similar to that used by Young, *et al.* [48], the spectra were then combined to eliminate vibrational contamination in the measured unsteady force spectra (the source of this contamination is discussed later). A cross correlation spectrum $X_{\alpha\beta}(\omega)$ (where angular frequency $\omega = 2\pi f$) between two signals $\alpha(t)$ and $\beta(t)$ is defined by [3]

$$X_{\alpha\beta}(\omega) = \frac{1}{2\pi}\int_{-\infty}^{\infty} \langle \alpha(t)\beta(t+\tau)\rangle \, \mathrm{e}^{i\omega\tau}\, d\tau. \tag{4.2}$$

The coherence between the signals is then given (in dimensions of α^2) by [3]

$$X_{\alpha\beta}(\omega) \cdot X_{\beta\alpha}(\omega)/A_{\beta\beta}(\omega), \tag{4.3}$$

where $A_{\beta\beta}(\omega) \equiv X_{\beta\beta}(\omega)$ is the autocorrelation spectrum of signal β. Applying this to the experiment, vibrational contamination was approximately eliminated by subtraction from the measured unsteady force spectrum of any coherence with the vibration spectrum (measured by the accelerometer), according to

$$A_{FF,c}(\omega) = A_{FF}(\omega) - X_{aF}(\omega) \cdot X_{Fa}(\omega)/A_{aa}(\omega), \tag{4.4}$$

where $A_{FF,c}(\omega)$ is the 'corrected' unsteady force spectrum, $A_{FF}(\omega)$ and $A_{aa}(\omega)$ are respectively the measured unsteady force and vibration spectra, and $X_{aF}(\omega)$ and $X_{Fa}(\omega)$ are cross-correlation spectra between the accelerometer and force transducer signals.

4.3.2 Uncertainty

The major source of error in these measurements is vibrational contamination of the force sensor readings. Two sources of this contamination exist: background vibration from the experimental environment and structural vibrations in the transducer mounting assembly induced by the test jet. Transducer readings were collected with the jet off (i.e. $Q = 0$) to record any environmental noise, as well as electrical noise inherent in the transducers or electronics. These readings were consistently 10 to 40 dB below measurements taken with the jet on except at the lowest ($<$ 100 Hz) and highest frequencies ($>$ 30kHz).

Examples of the unsteady force and vibration spectra recorded for a jet with $Q = 0$ and $Q = 0.0047$ m^3/s, $\ell = 35$ mm are given in Figures 4.8 and 4.9.

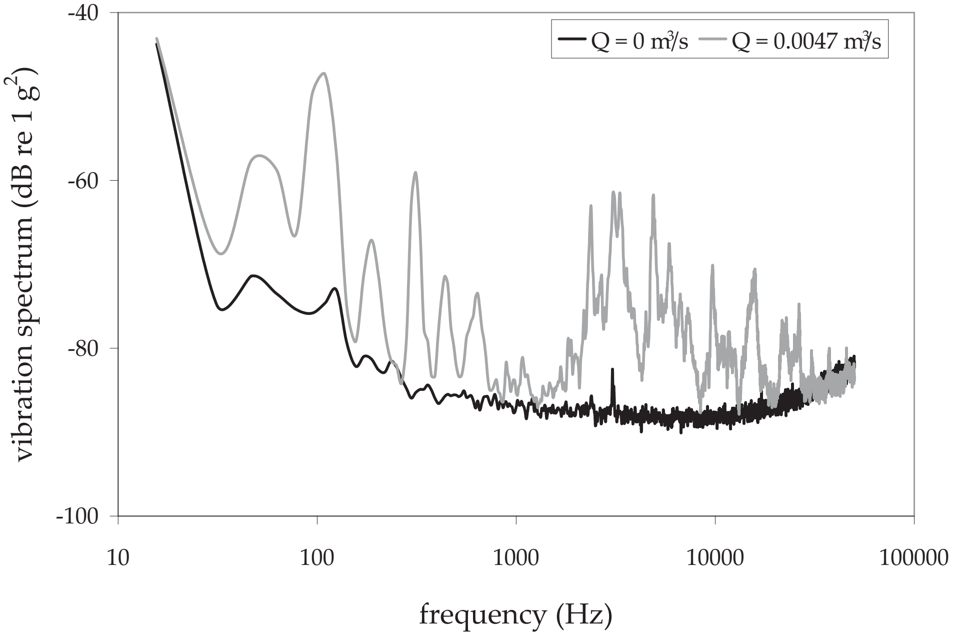

Figure 4.8. Comparison of the vibration spectra for jets of flow rates $Q = 0$ and $Q = 0.0047$ m^3/s and jet length $\ell = 35$ mm. The spectra are given in units of dB relative to 1 g^2.

Jet induced vibrations were partially eliminated by application of the coherence correction formula (4.4). Figure 4.10 presents an example of the unsteady force spectrum recorded for a trial at $Q = 0.0047\,\text{m}^3/\text{s}$ and $\ell = 35$ mm before and after application of the coherence formula. Noise up to 20dB was removed at frequencies across the entire measured bandwidth. However, it appears that there is still significant contamination of this unsteady force spectrum above 3000 Hz. Comparing corrected spectra for varying jet lengths and injection rates (see an example in Figure 4.11), we find that this contamination is consistently present in magnitude and frequency dependence in all of the readings, implying that the contamination is due to structural vibrations, rather than a true measurement of the unsteady force exerted by the jet. We will therefore choose

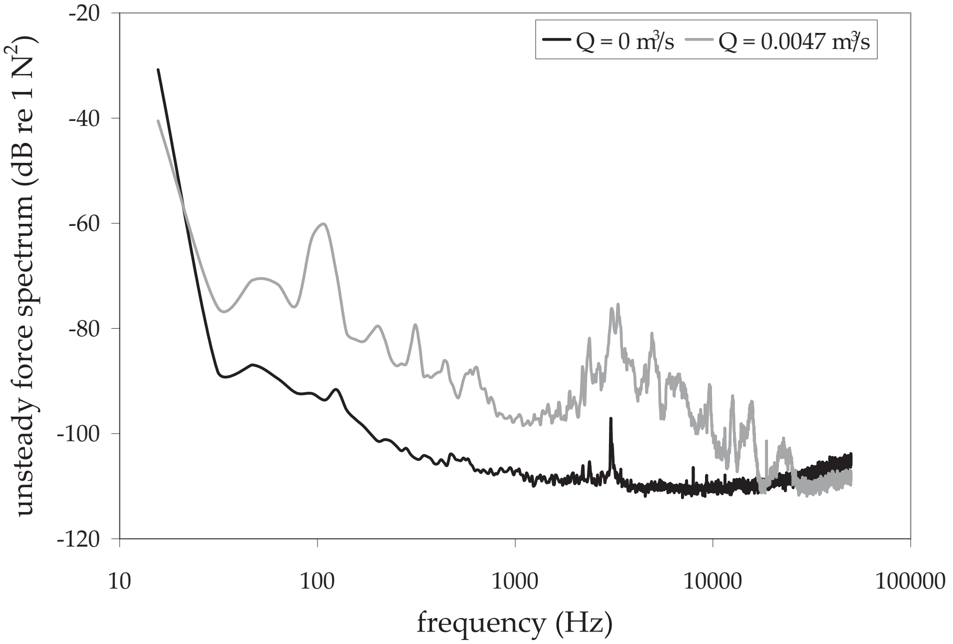

Figure 4.9. Comparison of the unsteady force spectra for jets of flow rates $Q = 0$ and $Q = 0.0047$ m^3/s and jet length $\ell = 35$ mm. The spectra are given in units of dB relative to 1 N^2.

to estimate the unsteady force over these higher frequencies by projecting a curve which continues the slope of the spectrum at lower frequencies (see Figure 4.12).

The normalized random statistical error η_r for each spectrum can be estimated as [3]

$$\eta_r = \frac{1}{\sqrt{n}} \tag{4.5}$$

where n is the number of samples averaged in the ensemble. As given in Section 4.2, 60 samples were averaged in each ensemble for an error of ± 0.13. Random error in the readings as assessed by variation between duplicated runs (repeatability) is estimated at ± 1.5 dB (see Fig. 4.13 for an example). Errors in frequency are systematic, dominated by the chosen bin width of the Fourier transform, and are on the order of ± 7.8 Hz. The combined statistical and bias errors in the jet exit velocity measurements produced an error of $\sim \pm 1$ m/s.

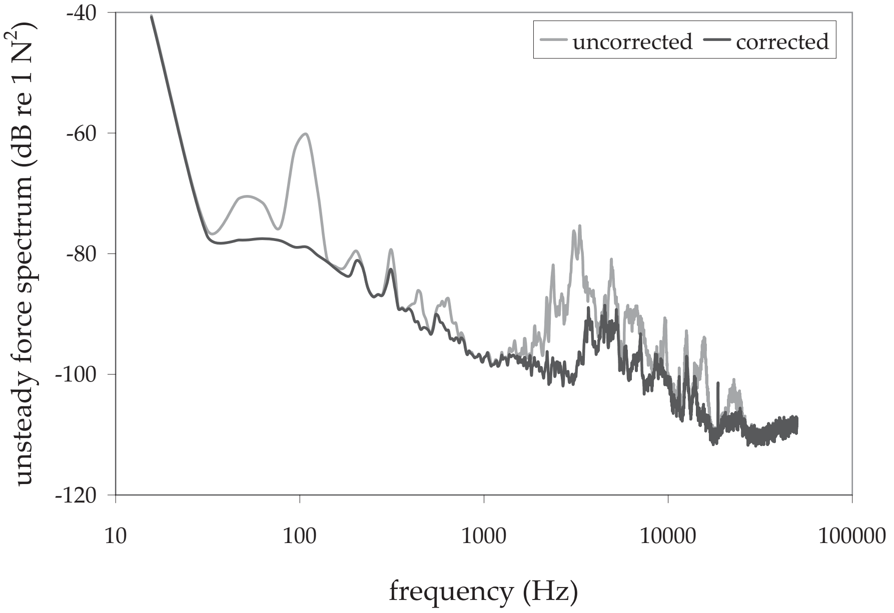

Figure 4.10. Comparison of the corrected and uncorrected unsteady force spectra ($A_{FF,c}$ and A_{FF} of Eq. 4.4, respectively) for $Q = 0.0047\,\mathrm{m}^3/\mathrm{s}$ and $\ell = 35\,\mathrm{mm}$. The spectra are given in units of dB relative to 1 N^2.

Finally we consider the validity of the force spectra measured for jet lengths >20 mm, for which the cross-sectional area of the jet at impact is larger than the force transducer measurement surface. Figure 4.14 compares the corrected force spectra for trials at each jet length $\ell = 15$, 20, 30, and 40 mm and injection rate $Q = 0.0047\mathrm{m}^3/\mathrm{s}$. The greatest disparity between the spectra occurs near 1000 Hz, which may imply that these frequencies are dominant at the outer edge of the jet's cross-section and they are not being captured by the transducer at longer jet lengths. However, across the rest of the measured bandwidth we find an average difference of approximately ±2 dB between the spectra. This difference is of the same order as the statistical error between repeated runs (see above); we therefore conclude that the force spectrum measurements for jets with lengths longer than 20 mm sufficiently approximate the entire force exerted by the jet across these frequencies. Furthermore, the disparity between the spectra occurs well below the frequencies of interest for the self noise problem, so we consider it acceptable

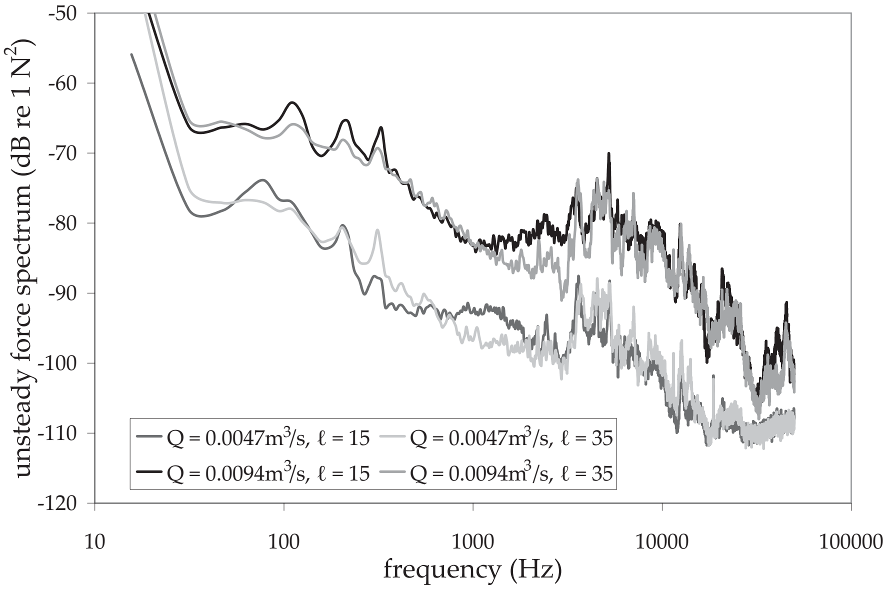

Figure 4.11. Comparison of the corrected unsteady force spectra for jets with $Q = 0.0047$ and $0.0094\,\mathrm{m}^3/\mathrm{s}$ and $\ell = 15$ and $35\,\mathrm{mm}$. The spectra are given in units of dB relative to 1 N^2.

to use these measurements to make predictions for the sound generated by the longer jets.

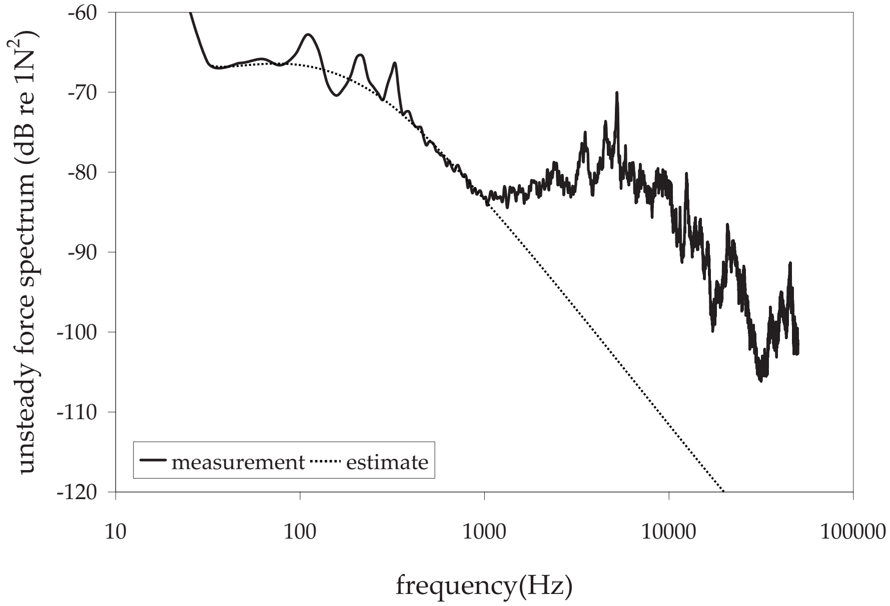

Figure 4.12. Demonstrating the estimate of the unsteady force spectrum for frequencies >3000 Hz. The given spectrum was measured for a jet of length $\ell = 15$ mm and injection rate $Q = 0.0094\,\mathrm{m}^3/\mathrm{s}$, and is presented in units of dB relative to 1 N^2.

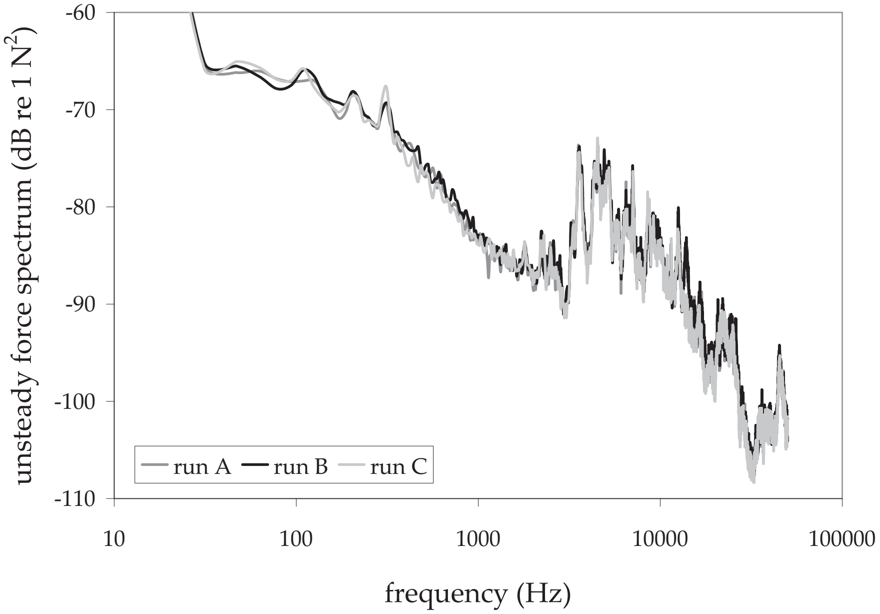

Figure 4.13. Comparison of corrected force spectra for multiple trials at $Q = 0.0094$ m^3/s and $\ell = 35$ mm. The spectra are given in units of dB relative to 1 N^2.

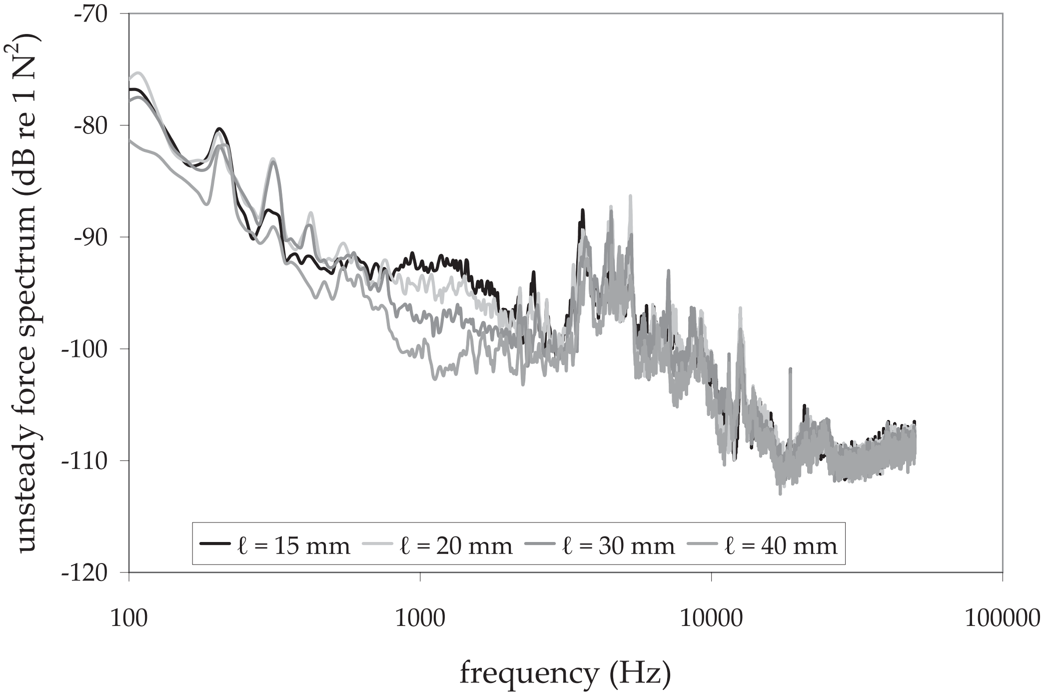

Figure 4.14. Comparison of corrected force spectra for trials at $Q = 0.0047$ m^3/s and $\ell = 15$, 20, 30, and 40 mm. The spectra are given in units of dB relative to 1 N^2.

4.4 Results

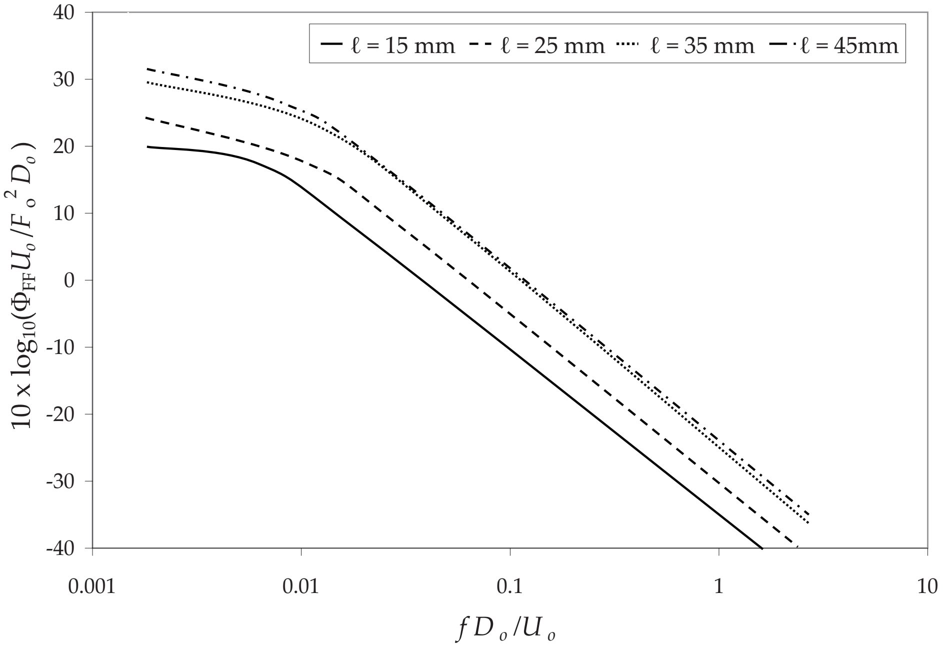

Figure 4.15. Measured force spectra for jets of gas injection rate $Q = 0.0047$ m^3/s and jet lengths $\ell = 15$, 25, 35, and 45 mm, normalized to mean force F_o in 15.6 Hz bins, versus dimensionless frequency fD_o/U_o.

The corrected unsteady force spectra are taken to be the spectra of the impact force for a single jet on the supercavity's gas-water interface (i.e. $\Phi_{FF}(\omega) \equiv A_{FF,c}(\omega)$). Figures 4.15-4.17 depict the measured normalized impact force spectrum

$$10 \times \log_{10}\left(\frac{\Phi_{FF}(\omega)U_o}{F_o^2 D_o}\right)$$

as a function of non-dimensional frequency fD_o/U_o for the gas flow rates of 0.0047, 0.0071, and 0.0094 m^3/s, respectively, where F_o is the mean force exerted by the jet, D_o is the diameter of the jet orifice, and U_o is the mean centerline jet velocity at the orifice.

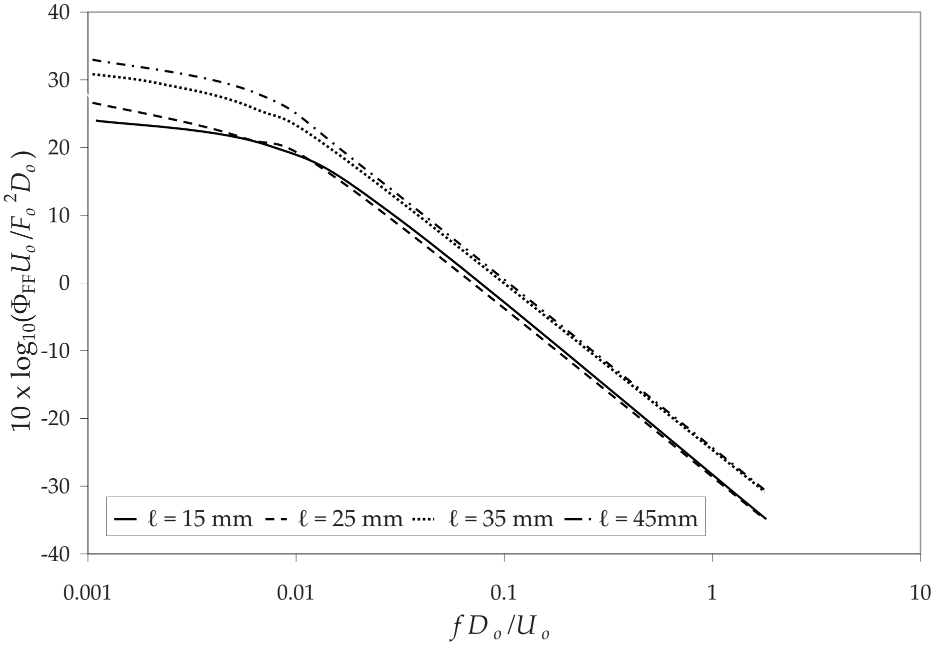

Figure 4.16. Measured force spectra for jets of gas injection rate $Q = 0.0071$ m^3/s and jet lengths $\ell = 15$, 25, 35, and 45 mm, normalized to mean force F_o in 15.6 Hz bins, versus dimensionless frequency fD_o/U_o.

F_o is defined by the momentum balance formula

$$F_o = \rho_A U^2 \frac{\pi D^2}{4}, \tag{4.6}$$

where U is the mean jet velocity at impact, D is the diameter of the jet impact area, and ρ_A is the mean density of the jet. The density ρ_A is approximated as that for air at STP, 1.2 kg/m^3, based on temperature readings of the jet which measured only about 3° lower than ambient. D is calculated for each jet length ℓ from $D_o = 2R_o$ using Eq. (4.1). As described in §4.2, the jet exit centerline velocity U_o was measured for the jets of $Q = 0.0047$ m/s with a probe velocimeter. The value of U_o was determined for higher flow

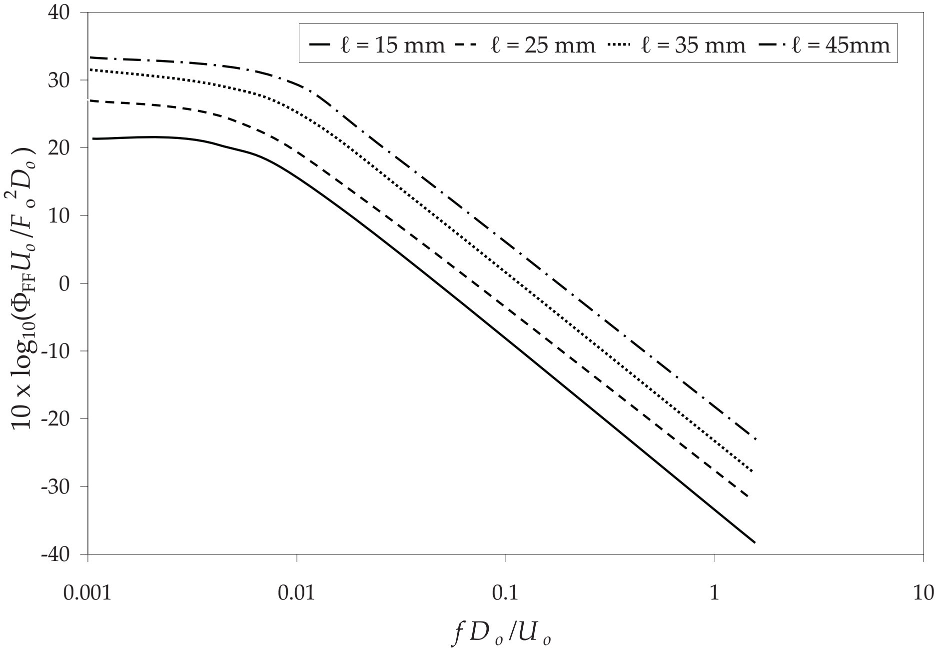

Figure 4.17. Measured force spectra for jets of gas injection rate $Q = 0.0094$ m^3/s and jet lengths $\ell = 15$, 25, 35, and 45 mm, normalized to mean force F_o in 15.6 Hz bins, versus dimensionless frequency fD_o/U_o.

rates by assuming a linear relationship between flow rate and velocity, i.e.

$$U_2 = U_1 \frac{Q_2}{Q_1} \tag{4.7}$$

where U_1 and U_2 are the exit velocities which correspond to injection flow rates Q_1 and Q_2, respectively. This relationship is derived using the definition of the volume flow rate out of the jet orifice $Q_o = U_o(\pi/4)D_o^2$.

The volume flow rate $Q' = U(\pi/4)D^2$ through any cross-section of the jet at length ℓ is given by [29]

$$Q' = \beta Q_o \frac{\ell}{R_o}. \tag{4.8}$$

For a circular jet orifice, the empirical value of $\beta = 1.5$ [29]. Applying the definitions of Q', Q_o to (4.8), the mean jet impact velocity for a jet of length ℓ is interpolated from the exit velocity using [29]

$$U = 1.5U_o \left(\frac{\ell}{R_o}\right)\left(\frac{D_o^2}{D^2}\right) \tag{4.9}$$

This self-similarity relation breaks down near the jet orifice. For the shortest jet length ℓ = 15 mm, the impact velocity is unlikely to differ significanly from the exit velocity [16]; we will therefore take $U \approx U_o$. Values of D and U (D_o and U_o at the jet orifice, $\ell = 0$) for each case are tabulated below.

ℓ (mm)	0	15	20	25	30	35	40	45
D_o, D (mm)	1.6	8.3	10.5	12.7	14.9	17.1	19.3	21.6
U_o, U (m/s); $Q = 0.0047$ m^3/s	27.1	27.1	23.7	20.2	17.6	15.5	13.9	12.6
U_o, U (m/s); $Q = 0.0071$ m^3/s	40.7	40.7	35.6	30.3	26.3	23.3	20.9	18.9
U_o, U (m/s); $Q = 0.0094$ m^3/s	54.2	54.2	47.5	40.4	35.2	31.1	27.8	25.2

Table 4.2. Estimated values of jet diameter D and exit ($\ell = 0$) and mean impact velocities U_o and U for each trial at jet length ℓ and injection flow rate Q.

In all cases the spectra in Figures 4.15-4.17 peak near $fD_o/U_o \sim 0.01$ then drop off rapidly like $(fD_o/U_o)^{-2.5}$. For the purpose of presentation, the spectra for the intermediate jet lengths of 20, 30, and 40 mm have been omitted; the normalized unsteady force spectra of all of the collected data are presented in Appendix E.

Figure 4.18 presents the unnormalized measured force spectra plotted against frequency for jets with test parameters $Q = 0.0047$ and $0.0094\,\text{m}^3/\text{s}$ and $\ell = 15$ and $35\,\text{mm}$. This plot elucidates the relationship between injection rate and the magnitude of the measured force spectrum as well as jet length and magnitude. Let us consider that the unsteady component F of the force exerted by the jet scales with the mean component of the exerted force F_o and the unsteady component of the jet's impact velocity u scales with the mean component of the impact velocity U. As $\Phi_{FF} \propto F^2 \propto u^4$, then a doubling of the injection flow rate (and *e.g.* the mean impact velocity U) results in four-fold increase in the mean force, for a sixteen-fold or 12dB increase in $F^2 \propto \Phi_{FF}$. Our data approximate this well, with an estimated 10-15 dB increase in the unsteady force spectrum with the doubling of the injection flow rate. There is also only a 2-3 dB difference between the unsteady force spectra for jets of differing length; this is attributable to statistical variability between runs.

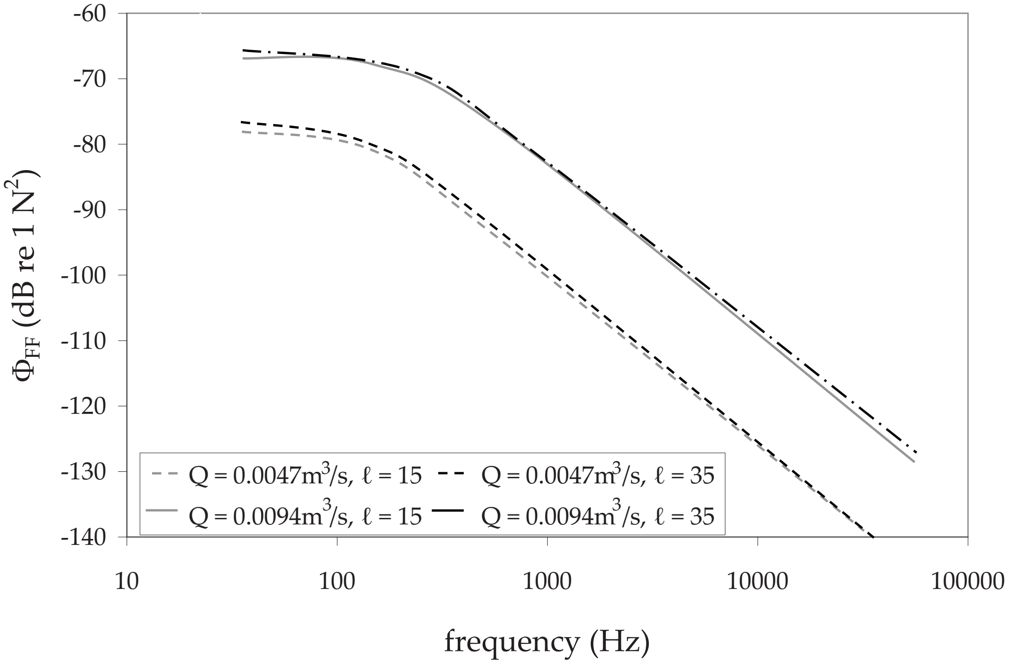

Figure 4.18. Measured force spectra for jets with test parameters $Q = 0.0047$ and 0.0094 m^3/s and $\ell = 15$ and $35\,$mm. The spectra are given in units of dB relative to 1 N^2.

4.5 Predicted acoustic power spectra

These impact force spectra can be used with the results of Chapter 3 to predict the spectrum of the sound power generated by jet impingement on a planar interface. From the definition of sound power (see Appendix A), the radiated sound power spectrum $\Pi(\omega)$, the power spectrum for the sound which transmits to the far field, is given by

$$\Pi(\omega) = \int_0^{2\pi} \int_0^{\pi/2} \frac{\Phi_{PP}(\omega)}{\rho_w c_w} |\mathbf{x}|^2 \sin\theta d\theta d\phi \tag{4.10}$$

where the integration is over the surface of a large hemisphere in the water of radius $|\mathbf{x}|$ centered on the centroid of the gas interface impact region. Note that in (3.8) the terms in parenthesis represent respectively the near and far pressure fields, and the near field term vanishes as $|\mathbf{x}| \to \infty$, yielding

$$\Pi(\omega) = \Phi_{FF}(\omega) \frac{k_w^2}{6\pi \rho_w c_w}. \tag{4.11}$$

A convenient nondimensional form is

$$\frac{\rho_w \Pi(\omega)}{M^2 \rho_A^2 U^2 D^3} = \frac{\Phi_{FF}(\omega) c_w}{F_o^2 D} \frac{\pi (k_w D)^2}{96}, \tag{4.12}$$

where M is the jet Mach number U/c_w relative to the speed of sound in water. The variation of

$$10 \times \log_{10} \left(\frac{\rho_w \Pi(\omega)}{M^2 \rho_A^2 U^2 D^3} \right) \mathrm{dB}$$

with reduced frequency $k_w D$ is plotted in Figures 4.19-4.22 for the measured cases $\ell = 15$, 25, 35, and 45 mm at 0.0047, 0.0071, and 0.0094 m^3/s. Predictions of the radiated sound power spectrum based on all of the measured force spectra are given in Appendix E.

The predictions have collapsed to a common form across all frequencies, peaking in $0.005 < k_w D < 0.05$ and dropping off like $k_w D^{-0.5}$. This implies that the dominant sound is in a frequency range where the wavelength $\lambda = 2\pi/k_w$ is much larger than the characteristic length D, validating our hypothesis of acoustic compactness required by the plane interface approximation. The relative differences between runs of varying flow lengths are attributable to statistical variation for each run and the differing magnitudes of the normalizing quantities. As $\Pi \propto \Phi_{FF}$, Figure 4.18 and its discussion at the end of §4.4 indicate that there is approximately a 10-15 dB increase in radiated sound power

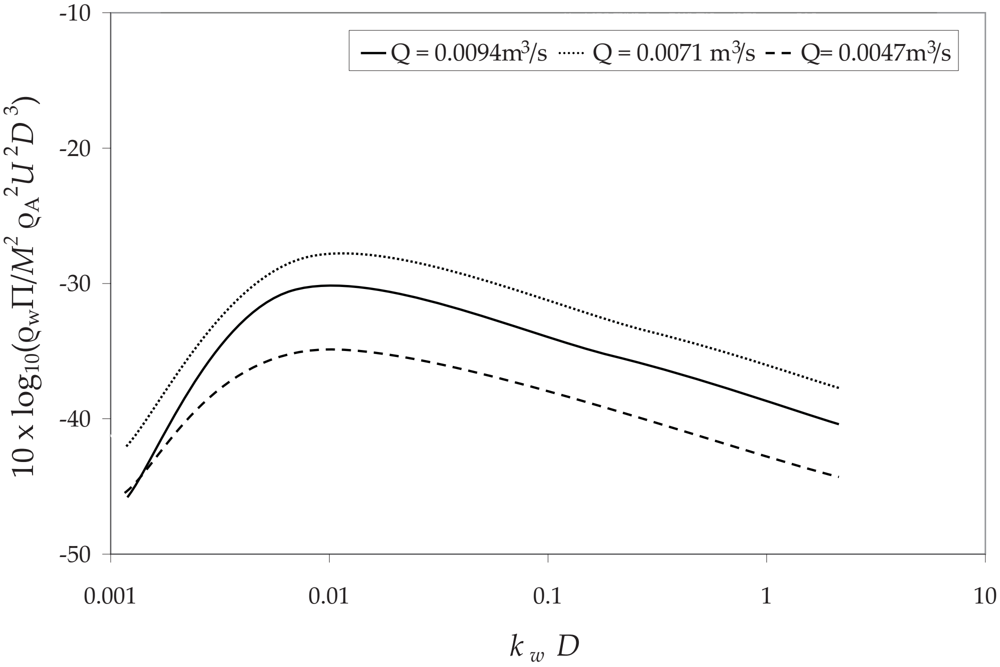

Figure 4.19. Predicted sound power spectra for jets of gas injection rate $Q = 0.0047$, 0.0071, and 0.0094 m^3/s and $\ell = 15\,\text{mm}$ versus reduced frequency k_w/D.

with a doubling of gas injection rate.

4.6 Comparison with Strong *et al.*

In order to have some independent support for these results we look to the work of Strong *et al.* [45]. In their experiment an air jet with nozzle diameter 102 mm was directed at a heavy plate. Two pinhole microphones flush mounted in the plate, one at the centroid of the impact area and the second at various radial distances from this centroid, were used to measure the correlation of the unsteady surface pressure on the plate for frequencies between 40 and 10,000 Hz. Their results include the frequency spectral density of these pressure fluctuations $\Phi_p(\omega)$ (in their nomenclature) on the plate for a jet at normal incidence. This is a measurement of the unsteady pressure exerted on the plate at the centroid of the impact area, not a measurement of the pressure spectrum of the sound

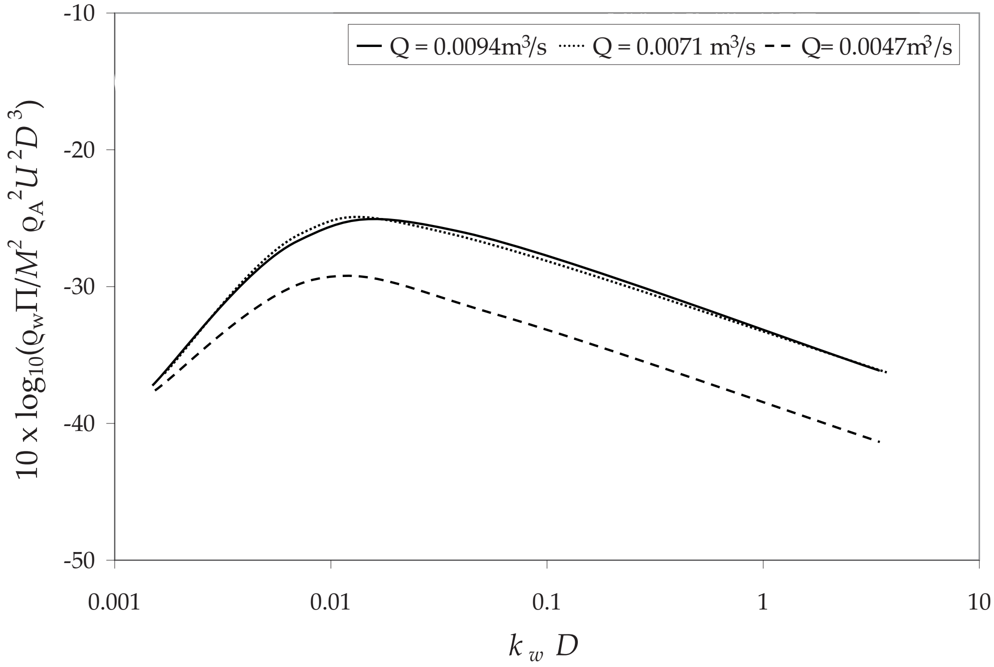

Figure 4.20. Predicted sound power spectra for jets of gas injection rate $Q = 0.0047$, 0.0071, and 0.0094 m^3/s and $\ell = 25\,\mathrm{mm}$ versus reduced frequency k_w/D.

radiating from the jet impact region, which we have previously called $\Phi_{pp}(\omega)$. These data are reproduced in Figure 4.23, normalized by mean jet density ρ_A, jet exit velocity U_o, and jet orifice diameter D_o and plotted against the dimensionless frequency $\omega D_o/U_o$.

The pressure spectrum can be used to make a rough estimate of the spectrum of the force exerted on the plate by the jet. As a first approximation we assume that all frequency components of the pressure on the plate are fully correlated over the impact area $\frac{\pi}{4}D^2$, *i.e.* we assume

$$\Phi_{FF}(\omega) = \Phi_p(\omega)\left(\frac{\pi}{4}D^2\right)^2 . \tag{4.13}$$

This cannot be correct, because the *correlation area* of the surface pressure must be smaller than $\frac{\pi}{4}D^2$. Therefore the approximation (4.13) will provide an upper bound for the acoustic radiation spectrum. Again using Eqs. (4.1) and (4.6) to define the experiment's characteristic dimensions of mean impact velocity and mean force, the

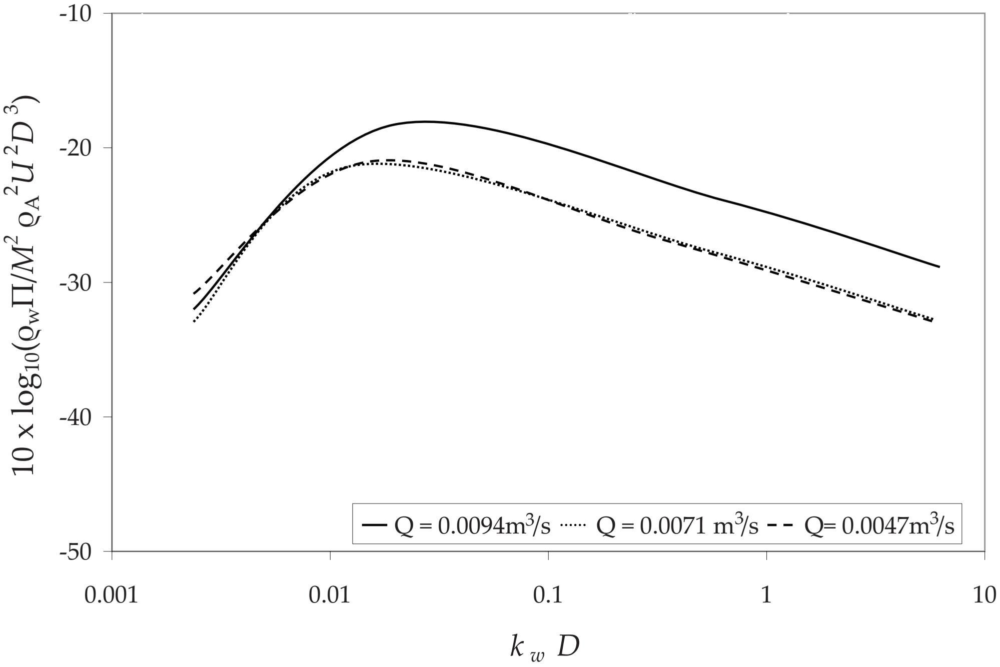

Figure 4.21. Predicted sound power spectra for jets of gas injection rate $Q = 0.0047$, 0.0071, and 0.0094 m^3/s and $\ell = 35\,\mathrm{mm}$ versus reduced frequency k_w/D.

normalized force spectrum defined by (4.13) becomes

$$10 \times \log_{10}\left(\frac{\Phi_{FF}(\omega)U_o}{F_o^2 D_o}\right) \equiv 10 \times \log_{10}\left(\frac{\Phi_P(\omega)U_o}{\rho_A^2 U^4 D_o}\right)$$

which is plotted in Figure 4.24 versus fD_o/U_o. Also plotted are measured unsteady force spectra for the supercavity jets; because the experiment in Strong *et al.* was conducted with a jet length of $14R_o$, we have chosen the most similar cases of $\ell = 15$ mm ($= 18.75R_o$) and $Q = 0.0047$, 0.0071, and $0.0094\,\mathrm{m}^3/\mathrm{s}$ for comparison. As with the ARL jets, the Strong *et al.* estimated unsteady force spectrum drops off like $(fD_o/U_o)^{-2.5}$. The apparent shift in the curve is likely a consequence of the differing normalization values for each experiment, while the similar frequency dependence confirms the validity of our measurement technique and estimation for higher frequencies.

The estimated force spectrum is used to predict the sound power spectrum generated

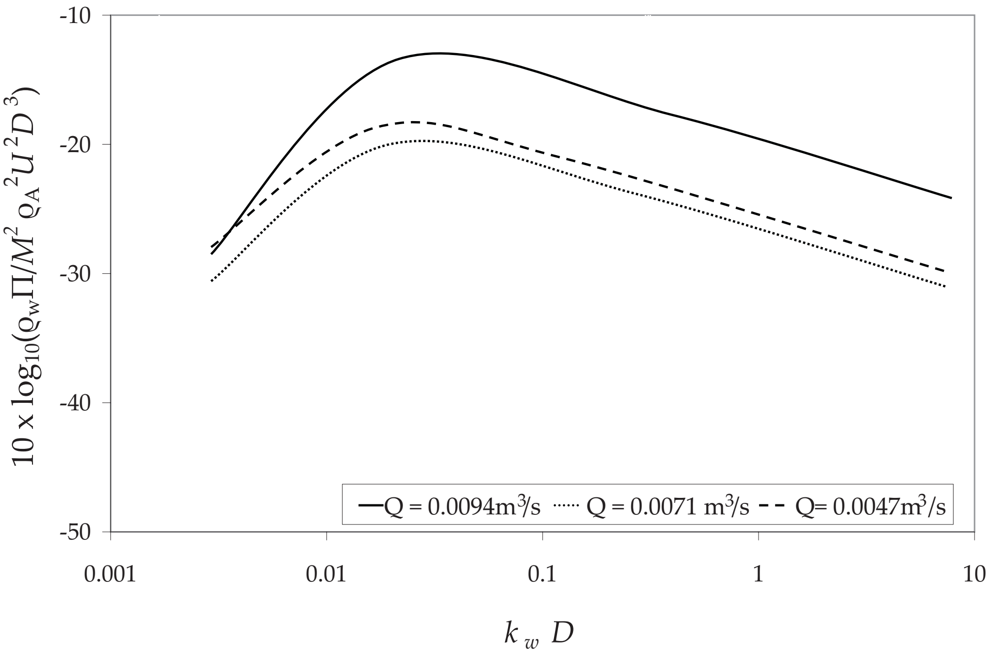

Figure 4.22. Predicted sound power spectra for jets of gas injection rate $Q = 0.0047$, 0.0071, and 0.0094 m^3/s and $\ell = 45\,\mathrm{mm}$ versus reduced frequency k_w/D.

when the jet impinges on a gas-water interface, given by Eq. 4.11. Figure 4.25 presents the normalized sound power spectra

$$10 \times \log_{10}\left(\frac{\rho_o \Pi(\omega)}{M^2 \rho_A^2 U^2 D^3}\right) \mathrm{dB}$$

(plotted against dimensionless frequency $k_w D$) for the jet of Strong *et al.* compared with corresponding predictions based on our measurements using a supercavitating vehicle jet. The Strong *et al.* spectrum peaks near $k_w D = 0.2$ and drops off like $(k_w D)^{-0.5}$. The similarity of the frequency dependence between the predictions for the Strong *et al.* and ARL jet again confirms the validity of our chosen measurement technique and the generality of our mathematical solution for the acoustic pressure.

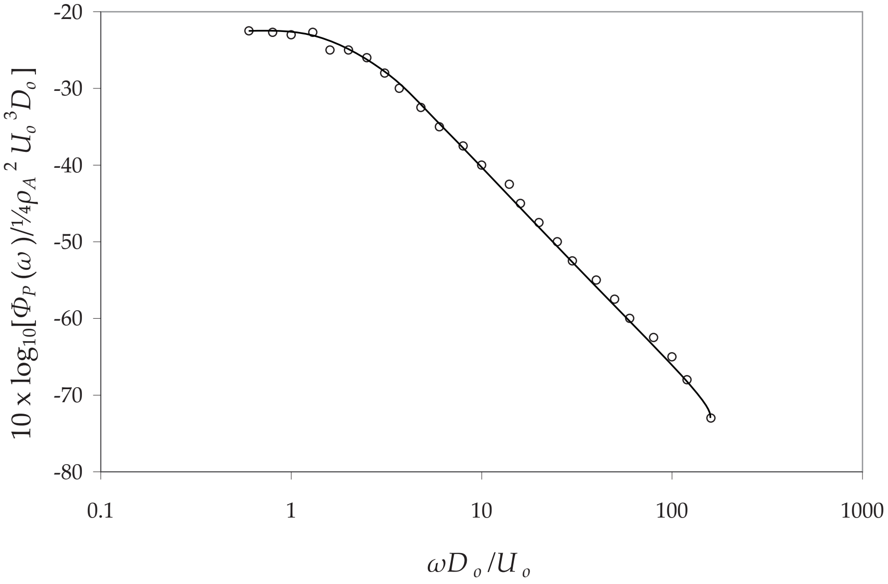

Figure 4.23. Pressure spectral density at the centroid of the impact area for the jet measured by Strong *et al.* [45].

4.7 Conclusions

Observations about the noise predictions for a plane interface can be used to postulate similar characteristics for the sound generated by a ventilation jet impinging on a more realistic cylindrical interface of a supercavity. The observed small differences in force spectra associated with differences in the jet length indicate that for an experimental supercavity, where an accurate determination of the jet length is not easily made, a rough estimate of ℓ to within, say, 5 mm, is sufficient to derive an adequate prediction of the radiated sound.

The measured effect of increased flow rate on the magnitude of the impact force spectrum for a single jet on a plane interface will likely be representative of the multiple jet case for the supercavity. For the planar interface Fig. 4.18 and Eq. 4.11 indicate that the sound power increases by 10-15 dB when the injection flow rate is doubled. This may not be the case for multiple jets because of possible correlations between the surface

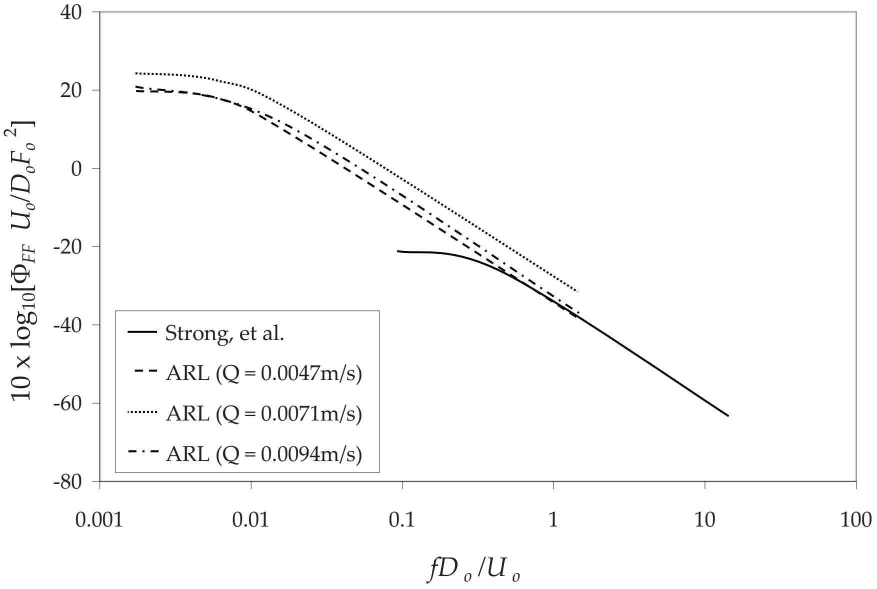

Figure 4.24. Comparison of unsteady force spectra for ARL jets of $Q = 0.0047$, 0.0071, and $0.0094\,\mathrm{m}^3/\mathrm{s}$ and $\ell = 15\,\mathrm{mm}$ and the jet of Strong *et al.* [45].

force fluctuations produced by neighboring jets. In any event, because an increase in the gas injection rate causes a rapid increase in sound power it would evidently be of considerable interest to determine the minimum gas injection rate that can safely sustain the supercavity of an underwater vehicle in a stable form.

It can be anticipated that the directivity of sound radiated from a real supercavity must differ in detail from that from a planar interface because of possible interference between neighboring jets and the fundamental geometric differences. On the planar interface the jet produces a single dipole source projecting into the water, normally to the interface, while the supercavity creates an axisymmetric array of dipoles projecting normally off of the cavity into the water. However, the far field magnitudes and frequency dependences of the generated sound should be similar. The sound power spectra predicted for the plane interface indicate that most of the radiated sound is contained in the frequency range $0.005 < k_w D < 0.05$. This confirms the assumption that the jet impact region is acoustically compact, and therefore that the local geometry of the im-

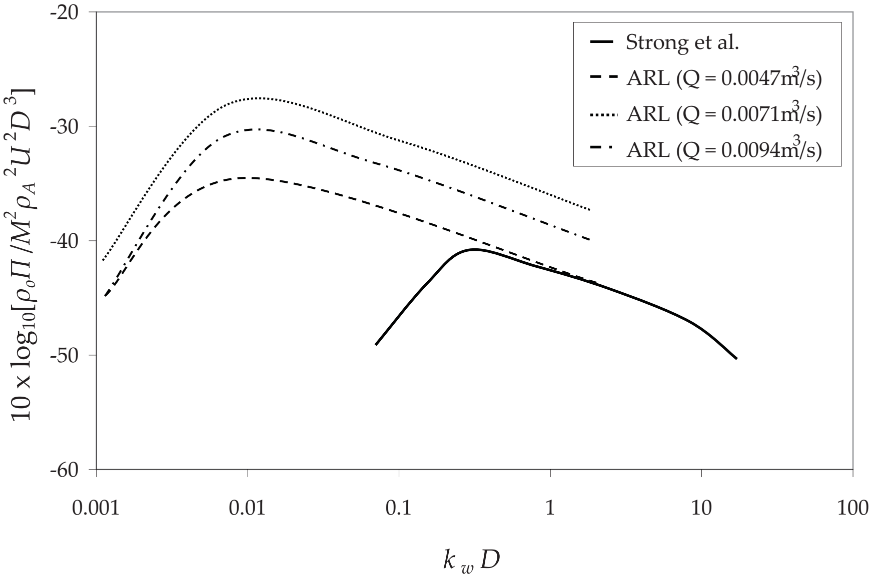

Figure 4.25. Comparison of predicted sound power spectra for ARL jets of $Q = 0.0047$, 0.0071, and $0.0094\,\mathrm{m}^3/\mathrm{s}$ and $\ell = 15\,\mathrm{mm}$ and the jet of Strong *et al.* [45].

pact region is probably irrelevant. The power spectrum for the sound radiated from the supercavity would be expected to exhibit a frequency dependence that is very similar to that predicted for the plane interface, again with the peak acoustic frequencies between $0.005 < k_w D < 0.05$.

Chapter 5

Self-noise at the vehicle nose

In this chapter we predict the high-frequency impingement generated noise at the vehicle nose. We choose to model the experimental ventilated cavity as a gaseous, circular cylinder seated behind a solid ellipsoidal cavitating nose section (see Figure 5.1). The ventilating jets exert an unsteady pressure on the cavity interface downstream of the cavitator. This constitutes an acoustic source of dipole type which generates sound in the water. By finding a suitable frequency-dependent *transfer function* we can relate the jet-exerted pressure to the corresponding acoustic pressure, or 'self-noise,' at the vehicle nose. The transfer function, computed for the simplified ellipsoidal nose and cylindrical cavity geometry, takes account of diffraction of high frequency waves and creeping waves on the nose and the surface transition from the solid nose section to the gas-water cavity interface.

The solution for the acoustic pressure at the nose in terms of the transfer function is given in Section 5.1. The transfer function is determined analytically in Section 5.2 and approximated numerically for high and intermediate frequencies in Section 5.3. In Section 5.4, the spectrum of the sound at the nose is derived in terms of the spectrum of the unsteady force exerted by a ventilating jet. In Section 5.5, the results of §5.3, §5.4

are combined with the experimental results of Chapter 4 to predict the self-noise at the nose generated by the experimental supercavitating vehicle.

5.1 Pressure fluctuations at the nose

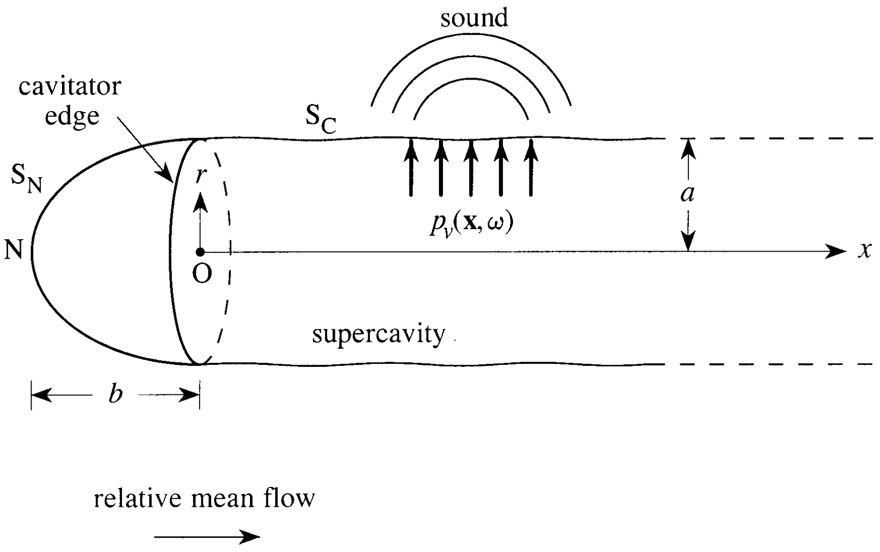

Figure 5.1. Model of a cylindrical supercavity with an ellipsoidal cavitator.

We consider the undisturbed gas-water interface (S_C in Figure 5.1) to be a circular cylinder of radius $r = a$ coaxial with the positive x axis, taking the origin at the midpoint O of the rear, plane face of the cavitator. The surface S_N of the cavitator in contact with the water is defined in terms of the cylindrical coordinates of Figure 5.1 by the ellipsoid

$$r = a\sqrt{1 - \frac{x^2}{b^2}}, \quad -b < x < 0, \quad b > a, \tag{5.1}$$

where b and a are respectively the lengths of the semi-major and minor axes. The water has density ρ_w and sound speed c_w, and the material of the cavitator is assumed to be locally reacting, such that at a point on S_N where the acoustic pressure is p and the outward (into the water) normal component of velocity is v_n we can write

$$\frac{p}{v_n} = -\ \rho_w c_w \mathcal{Z}, \tag{5.2}$$

where $\mathcal{Z}$ is the dimensionless surface impedance. In practice the Mach number of the relative mean flow over the supercavity is sufficiently small that the convection of sound can be ignored. Also ignoring turbulence noise sources in the mean flow, the acoustic pressure $p(\mathbf{x}, \omega)e^{i\omega t}$ of radian frequency ω in the water propagates like [6, 10, 12, 18, 32]

$$\left(\nabla^2 + k_w^2\right) p = 0, \tag{5.3}$$

where $k_w = \omega/c_w$ is the acoustic wavenumber. The visco-thermal dissipation of the sound is ignored, so that equation (5.2) implies

$$\frac{\partial p}{\partial x_n} + \frac{ik_w p}{\mathcal{Z}} = 0 \;\text{ on } \mathrm{S_N}, \tag{5.4}$$

where x_n is the local outward normal coordinate.

Consider the sound generated in the water by the impingement of ventilating gas jets on the cavity wall $\mathrm{S_C}$. The jets produce a localized fluctuating surface pressure $p_v(\mathbf{x}, \omega)$ on $\mathrm{S_C}$ which is equivalent to an array of dipole acoustic sources radiating into the water. The distribution and frequency of $p_v(\mathbf{x}, \omega)$ are known from the measurements described in Chapter 4. The disparity between the mean gas and water densities allows the interface to be treated as a pressure release surface, and we therefore assume that pressure fluctuations elsewhere on $\mathrm{S_C}$ can be neglected.

Let $p_N(\omega)$ denote the acoustic pressure produced by jet impingement at the tip of the nose $\mathrm{S_N}$ (the intersection of the negative x axis and $\mathrm{S_N}$). To express this in terms of $p_v(\mathbf{x}, \omega)$ we introduce a Green's function $G(\mathbf{x}, \omega)$ with outgoing wave behavior which is defined by

$$\left(\nabla^2 + k_w^2\right) G = 0 \tag{5.5}$$

in the water, subject to

$$\left.\begin{array}{rcll} \dfrac{\partial G}{\partial x_n} + \dfrac{ik_w G}{\mathcal{Z}} & = & \delta(y)\delta(z) & \text{on } \mathrm{S_N}, \\[2ex] G & = & 0 & \text{on } \mathrm{S_C}, \end{array}\right\} \tag{5.6}$$

where $\delta(\cdot)$ is the Dirac-delta function and the coordinates y,z are defined such that $\mathbf{x} = (x, y, z)$ forms a right-handed Cartesian basis. This defines G to be an axisymmetric function $G(x, r, \omega)$ of x and $r = \sqrt{y^2 + z^2}$.

Applying Green's theorem and the radiation condition (see Appendix B) to (5.5) and (5.3) yields [2, 10, 18]

$$\oint_{\mathrm{S_N+S_C}} \left(p(\mathbf{x}, \omega) \frac{\partial G}{\partial x_n}(\mathbf{x}, \omega) - G(\mathbf{x}, \omega) \frac{\partial p}{\partial x_n}(\mathbf{x}, \omega) \right) dS = 0, \tag{5.7}$$

where the integration is over the combined surfaces $\mathrm{S_N} + \mathrm{S_C}$ of the cavitator and the cavity interface. The boundary conditions (5.4) and (5.6), and the requirement that $p \equiv p_v$ on $\mathrm{S_C}$ then imply that

$$p_{\mathrm{N}}(\omega) = \int_{\mathrm{S}} p_v(\mathbf{x}, \omega)\, T(x, \omega)\, dS, \tag{5.8}$$

where the integration is over the impingement region S, say, of the cavity interface $\mathrm{S_C}$, and $T(x, \omega)$ is a *transfer function* defined by

$$T(x, \omega) \equiv - \left(\frac{\partial G}{\partial r}(x, r, \omega) \right)_{r=a}. \tag{5.9}$$

$T(x, \omega)$ depends only on frequency ω and distance from the cavitator edge x; the axisymmetry of the cavitator and cavity demand a solution for the acoustic pressure at the nose which is independent of the azimuthal location of the point on $\mathrm{S_C}$ where p_v is applied.

5.2 Calculation of the transfer function

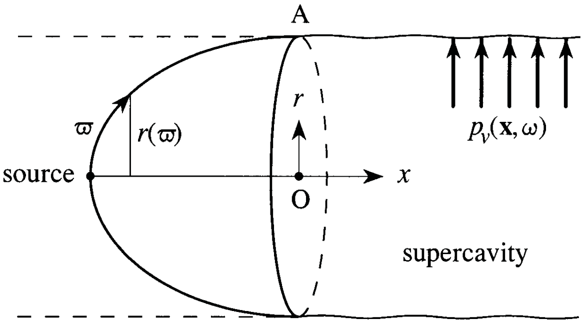

Figure 5.2. Reciprocal problem of the solution of the wave equation for the motion produced in the water by a unit point source at the nose used to calculate the transfer function

To calculate the transfer function we consider the reciprocal problem in which we first calculate the motion produced on the jet impingement region S from a point source at the nose (Figure 5.2). The region S lies in the geometric shadow of direct acoustic radiation from the source. The behavior of the Green's function in this region is therefore governed by the diffraction of sound waves around the nose of the cavitator, $\mathrm{S_N}$ (see [8, 15, 24, 25, 31, 35, 37, 38, 47]). This will be analyzed by interpolation between analytical predictions of $G(x, r, \omega)$ for large and small values of $k_w a$, an extension of the method of Howe *et al.* [23].

5.2.1 Surface diffraction when $k_w a \gg 1$

The surface diffraction of high frequency waves from the source can be represented in terms of *creeping modes*. The incidence of these modes on the edge A of the cavitator is first calculated; a separate calculation is then performed to determine their subsequent propagation over the pressure release surface $\mathrm{S_C}$ to impingement region S.

The creeping wave representation is found by choosing the local approximation $G = G_\mathrm{N}$, where in the immediate vicinity of N G_N satisfies the 'earth flattening' approximation of the wave equation [8, 15, 25, 31, 35, 37]

$$\left[\frac{\partial^2}{\partial x_n^2} + \left(1 - \frac{2x_n}{\wp}\right)\frac{1}{\varpi}\frac{\partial}{\partial \varpi}\left(\varpi\frac{\partial}{\partial \varpi}\right) + k_w^2\right] G_\mathrm{N} = 0, \quad x_n \ll a, \tag{5.10}$$

subject to

$$\frac{\partial G_\mathrm{N}}{\partial x_n} + \frac{ik_w G_\mathrm{N}}{\mathcal{Z}} = \frac{1}{2\pi\varpi}\,\delta(\varpi) \quad \text{at} \quad x_n = 0, \tag{5.11}$$

where ϖ denotes curvilinear 'radial' distance on $\mathrm{S_N}$ from the point source at the nose along a meridional arc of the ellipsoid (5.1), and $\wp = a^2/b$ is the radius of curvature of $\mathrm{S_N}$ at N.

Following the method of Howe *et al.* [23], we introduce the zeroth-order Hankel transform

$$G_\mathrm{N}(x_n, \varpi) = 2\pi \int_0^\infty \hat{G}_\mathrm{N}(x_n, k) k J_o(k\varpi)\mathrm{d}k, \tag{5.12}$$

where J_0 is the Bessel function of zero order. Therefore [42]

$$\frac{\partial^2 \hat{G}_\mathrm{N}}{\partial x_n^2} + \frac{2k^2}{\wp}\left[x_n + \frac{\wp}{2}\left(\frac{k_w^2}{k^2}\right)\right]\hat{G}_\mathrm{N} = 0, \quad x_n > 0, \tag{5.13}$$

where, from (5.11),

$$\frac{\partial \hat{G}_\mathrm{N}}{\partial x_n} + \frac{ik_w \hat{G}_\mathrm{N}}{\mathcal{Z}} = \frac{1}{(2\pi)^2}, \quad x_n = 0. \tag{5.14}$$

The solution for this system with outgoing wave behavior is [8, 37]

$$\begin{aligned}\hat{G}_{\mathrm{N}}(x_n,k) &= \frac{1}{(2\pi)^2} \\ &\times \frac{\mathrm{Ai}\left\{\mathrm{e}^{-\frac{i\pi}{3}}\left(\frac{2|k|^2}{\wp}\right)^{\frac{2}{3}}\left[x_n+\left(\frac{k_w^2}{k^2}-1\right)\right]\right\}\mathrm{e}^{i(k\varpi-\frac{\pi}{4})}}{\left(\frac{2|k|^2}{\wp}\right)^{\frac{1}{3}}\mathrm{e}^{-\frac{i\pi}{3}}\mathrm{Ai}'\left\{\mathrm{e}^{-\frac{i\pi}{3}}\left(\frac{|k|\wp}{2}\right)^{\frac{2}{3}}\left(\frac{k_w^2}{k^2}-1\right)\right\}+\frac{ik_w}{\mathcal{Z}}\mathrm{Ai}\left\{\mathrm{e}^{-\frac{i\pi}{3}}\left(\frac{|k|\wp}{2}\right)^{\frac{2}{3}}\left(\frac{k_w^2}{k^2}-1\right)\right\}},\end{aligned} \tag{5.15}$$

where Ai denotes the Airy function [1] and the prime denotes differentiation with respect to its argument. Putting $x_n = 0$ on the surface, we find from (5.12) that

$$\begin{aligned}G_{\mathrm{N}}(0,\varpi) &= \frac{1}{2\pi} \\ &\times \int_0^\infty \frac{kJ_0(k\varpi)\,\mathrm{Ai}\left\{\mathrm{e}^{-\frac{i\pi}{3}}\left(\frac{|k|\wp}{2}\right)^{\frac{2}{3}}\left(\frac{k_w^2}{k^2}-1\right)\right\}\mathrm{e}^{i(k\varpi-\frac{\pi}{4})}\,dk}{\left(\frac{2|k|^2}{\wp}\right)^{\frac{1}{3}}\mathrm{e}^{-\frac{i\pi}{3}}\mathrm{Ai}'\left\{\mathrm{e}^{-\frac{i\pi}{3}}\left(\frac{|k|\wp}{2}\right)^{\frac{2}{3}}\left(\frac{k_w^2}{k^2}-1\right)\right\}+\frac{ik_w}{\mathcal{Z}}\mathrm{Ai}\left\{\mathrm{e}^{-\frac{i\pi}{3}}\left(\frac{|k|\wp}{2}\right)^{\frac{2}{3}}\left(\frac{k_w^2}{k^2}-1\right)\right\}},\end{aligned} \tag{5.16}$$

When $k_w a \gg 1$ the Bessel function may be replaced by its large argument approximation ($J_0(x) \sim \sqrt{2/\pi x}\cos(x-\pi/4)$ [1]), and the range of integration extended to $-\infty < k < \infty$ to give

$$\begin{aligned}G_{\mathrm{N}}(0,\varpi) &\approx \frac{1}{(2\pi)^{\frac{3}{2}}\sqrt{\varpi}} \\ &\times \int_{-\infty}^\infty \frac{\sqrt{k+i\epsilon}\,\mathrm{Ai}\left\{\mathrm{e}^{-\frac{i\pi}{3}}\left(\frac{|k|\wp}{2}\right)^{\frac{2}{3}}\left(\frac{k_w^2}{k^2}-1\right)\right\}\mathrm{e}^{i(k\varpi-\frac{\pi}{4})}\,dk}{\left(\frac{2|k|^2}{\wp}\right)^{\frac{1}{3}}\mathrm{e}^{-\frac{i\pi}{3}}\mathrm{Ai}'\left\{\mathrm{e}^{-\frac{i\pi}{3}}\left(\frac{|k|\wp}{2}\right)^{\frac{2}{3}}\left(\frac{k_w^2}{k^2}-1\right)\right\}+\frac{ik_w}{\mathcal{Z}}\mathrm{Ai}\left\{\mathrm{e}^{-\frac{i\pi}{3}}\left(\frac{|k|\wp}{2}\right)^{\frac{2}{3}}\left(\frac{k_w^2}{k^2}-1\right)\right\}},\end{aligned} \tag{5.17}$$

where $|k| = \sqrt{k^2+\epsilon^2}$ ($\epsilon \to +0$), with the branch cuts for $\sqrt{k \pm i\epsilon}$ taken respectively from $\mp i\epsilon$ to $\mp i\infty$ in the k-plane.

As $k_w\varpi \to \infty$ the main contribution to the integral is from the residues of poles at the zeros $k = k_n$ $(n = 1,\ 2,\ 3,\ \ldots)$ of

$$\left(\frac{2|k|^2}{\wp}\right)^{\frac{1}{3}} \mathrm{e}^{-\frac{i\pi}{3}} \mathrm{Ai}'\left\{\mathrm{e}^{-\frac{i\pi}{3}}\left(\frac{|k|\wp}{2}\right)^{\frac{2}{3}}\left(\frac{k_w^2}{k^2}-1\right)\right\} + \frac{ik_w}{\mathcal{Z}}\mathrm{Ai}\left\{\mathrm{e}^{-\frac{i\pi}{3}}\left(\frac{|k|\wp}{2}\right)^{\frac{2}{3}}\left(\frac{k_w^2}{k^2}-1\right)\right\} = 0 \tag{5.18}$$

in the upper k-plane. By making use of the formula $\mathrm{Ai}''(\xi) = \xi\mathrm{Ai}(\xi)$ [1] we accordingly find

$$G_{\mathrm{N}}(0,\varpi) \approx \frac{3\mathrm{e}^{\frac{3i\pi}{4}}}{2\sqrt{2\pi\varpi}}\sum_n \frac{\sqrt{k_n}\mathrm{e}^{ik_n\varpi}}{\left\{\frac{k_w}{\mathcal{Z}k_n} - \frac{ik_n\wp}{2}\left(\frac{2k_w^2}{k_n^2}+1\right)\left[1-\left(1-\frac{1}{\mathcal{Z}^2}\right)\frac{k_w^2}{k_n^2}\right]\right\}}, \quad k_w a \gg 1. \tag{5.19}$$

The solution is valid for $k_o\varpi \gg 1$ and is asymptotically accurate for ϖ less than about $\frac{1}{2}a$ [35]. Howe *et al.* [23] demonstrate how the geometrical theory of diffraction [31, 37] can be used to extend the range of validity of the solution out to the edge A of the cavitator. To do this the algebraic amplitude factor $1/\sqrt{\varpi}$ involving the curvilinear surface propagation distance ϖ must be replaced by $1/\sqrt{r}$ and the complex phase $k_n\varpi$ in the exponential factor $\mathrm{e}^{ik_n\varpi}$ must be modified to account for the variation of the creeping wavenumber $k_n = k_n(\varpi)$ because of the change in the radius of curvature $\wp = \wp(\varpi)$ of creeping surface rays with distance ϖ along the propagation path on $\mathrm{S_N}$. The result can be expressed in the form

$$G_{\mathrm{N}}(0,\varpi) \approx \frac{3\mathrm{e}^{\frac{3i\pi}{4}}}{2\sqrt{2\pi r}}\sum_n \left(\frac{\sqrt{k_n}}{\frac{k_w}{\mathcal{Z}k_n} - \frac{ik_n\wp}{2}\left(\frac{2k_w^2}{k_n^2}+1\right)\left[1-\left(1-\frac{1}{\mathcal{Z}^2}\right)\frac{k_w^2}{k_n^2}\right]}\right)_0 \mathrm{e}^{i\Psi_n(\varpi)}, \quad k_w a \gg 1. \tag{5.20}$$

where the quantity $(\cdot)_0$ is evaluated at the nose N (where $\wp = a^2/b$) and the phase Ψ_n is given by

$$\Psi_n = \int_0^{\varpi} k_n(\varpi')\,d\varpi', \tag{5.21}$$

in which k_n is the appropriate solution of Equation (5.18) when $\wp = \wp(\varpi')$.

5.2.2 Diffraction at the cavitator edge

When the creeping surface wave (5.20) reaches the edge A of the cavitator (Figure 5.2) it is further diffracted because of the change in surface condition from (5.11) on $\mathrm{S_N}$ to $G = 0$ on $\mathrm{S_C}$. Near A (where $r \to a$) the approaching surface wave $G_\mathrm{N}(0, \varpi)$ has a slowly varying amplitude but rapidly varying phase factor $\sim \mathrm{e}^{ik_w\varpi}$. The diffraction of this wave at the edge was treated approximately by Howe *et al.* [23] by imagining the surface of the cavitator to be deformed near A into a circular cylinder of radius a (depicted by the broken lines in Figure 5.2) that forms a rigid upstream continuation of the mean cylindrical cavity interface $\mathrm{S_C}$. The creeping wave (5.20) is then regarded as incident on A from along this cylinder, and expressed in the form

$$G_\mathrm{N}(0, \varpi) = \mathcal{G}_\mathrm{I}\mathrm{e}^{ik_w x} \tag{5.22}$$

where

$$\mathcal{G}_\mathrm{I} = \frac{3\mathrm{e}^{\frac{3i\pi}{4}}}{2\sqrt{2\pi}a}\sum_n \left(\frac{\sqrt{k_n a}}{\frac{k_w}{\mathcal{Z}k_n} - \frac{ik_n a^2}{2b}\left(\frac{2k_w^2}{k_n^2} + 1\right)\left[1 - \left(1 - \frac{1}{\mathcal{Z}^2}\right)\frac{k_w^2}{k_n^2}\right]} \right)_0 \mathrm{e}^{i\Psi_n(\ell)}, \tag{5.23}$$

and $\ell = b\,E\left(\sqrt{\frac{b^2-a^2}{b^2}}\right)$ is the curvilinear distance on the meridional geodesic on the ellipsoidal cavitator $\mathrm{S_N}$ from the nose N to the edge A, where $E(\xi)$ is the complete elliptic integral of the second kind [1].

Howe *et al.* [23] solved this diffraction problem for an acoustically *hard* cavitator by the method of Weiner-Hopf [9, 33] in the limiting case where $k_w a \gg 1$; the same method is applicable here. Letting G_S denote the edge diffracted component of G, in the region

$r > a$ we can write

$$G = \mathcal{G}_{\mathrm{I}} \mathrm{e}^{ik_w x} + G_{\mathrm{S}}(x, r), \tag{5.24}$$

where for some function $\mathcal{A}(k)$ we can put [10, 18, 33]

$$G_{\mathrm{S}}(x, r) = \int_{-\infty}^{\infty} \mathcal{A}(k) H_0^{(1)}(\gamma r) \mathrm{e}^{ikx} \mathrm{d}k, \tag{5.25}$$

where $H_0^{(1)}$ is the zeroth order Hankel function and $\gamma = \sqrt{k_w^2 - k^2}$, with branch cuts in the k-plane extending from $k = \pm(k_w + i\epsilon)$ $(\epsilon \to +0)$ to $\pm\infty$, so that γ is positive imaginary on the real axis when $|k| > k_w$. The function $\mathcal{A}(k)$ is determined from the conditions

$$\left.\begin{aligned} \frac{\partial G}{\partial r} + \frac{ik_w G}{\mathcal{Z}} = 0, &\qquad x < 0 \\ G = 0, &\qquad x > 0 \end{aligned}\right\}, \quad r = a + 0 \tag{5.26}$$

which supply the following dual integral equations satisfied by $\mathcal{A}(k)$

$$\int_{-\infty}^{\infty} \left(\gamma H_1^{(1)}(\gamma a) + \frac{ik_w}{\mathcal{Z}} H_0^{(1)}(\gamma a) \right) \mathcal{A}(k) \mathrm{e}^{ikx} \mathrm{d}k = 0, \qquad x < 0, \tag{5.27}$$

$$\int_{-\infty}^{\infty} \left(\mathcal{A}(k) H_0^{(1)}(\gamma a) + \frac{\mathcal{G}_1}{2\pi i (k - k_w - i\epsilon)} \right) \mathrm{e}^{ikx} \mathrm{d}k = 0, \qquad x > 0. \tag{5.28}$$

For $k_w a \gg 1$, the Hankel functions $H_0^{(1)}, H_1^{(1)}$ can be replaced by their large argument approximations [1]. Solving by the Wiener-Hopf method [9, 33]

$$G(x, r) \approx \mathcal{G}_1 \left(\mathrm{e}^{ik_w x} + \frac{i}{2\pi} \sqrt{\frac{a}{r}} \int_{-\infty}^{\infty} \frac{K_+(k_w) \mathrm{e}^{i\{kx + \gamma(r-a)\}} \mathrm{d}k}{K_+(k)(k - k_w - i\epsilon)} \right), \quad k_w a \gg 1 \tag{5.29}$$

where $K_+(k)$ is one of two functions $K_\pm(k)$ regular on the real k axis and respectively in $\mathrm{Im}\, k \gtrless 0$, and satisfying for real k

$$K_+(k) K_-(k) = \frac{k_w}{\mathcal{Z}} + \sqrt{(k_w + i\epsilon)^2 - k^2}\ . \tag{5.30}$$

Taking the derivative of (5.29) on the cavity interface $r = a$,

$$\left(\frac{\partial G}{\partial r}\right)_{r=a} = \frac{\mathcal{G}_{\mathrm{I}}}{2\pi}\int_{-\infty}^{\infty} \frac{K_+(k_w)\sqrt{k_w + i\epsilon + k}}{K_+(k)\sqrt{k_w + i\epsilon - k}}\,\mathrm{e}^{ikx}\mathrm{d}k, \quad \epsilon \to +0, \quad k_w a \gg 1, \tag{5.31}$$

When $x > 0$ and $k_w x$ is large, the main contribution to the integral in (5.31) is from the neighborhood of the branch point at $k = k_w + i\epsilon$. By expansion of the integrand about this point we find, to leading order, that

$$\left(\frac{\partial G}{\partial r}\right)_{r=a} \approx \mathcal{G}_{\mathrm{I}}\sqrt{\frac{2k_w}{\pi x}}\,\mathrm{e}^{i\left(k_w x - \frac{\pi}{4}\right)}, \quad k_w a \gg 1. \tag{5.32}$$

Using (5.23) and the definition (5.9), we obtain from this the corresponding explicit approximation for the transfer function

$$T(x,\omega) \approx -\frac{3i}{2\pi a^2}\sqrt{\frac{k_w a}{x/a}}\sum_n \left(\frac{\sqrt{k_n a}}{\frac{k_w}{\mathcal{Z}k_n} - \frac{ik_n a^2}{2b}\left(\frac{2k_w^2}{k_n^2} + 1\right)\left[1 - \left(1 - \frac{1}{\mathcal{Z}^2}\right)\frac{k_w^2}{k_n^2}\right]}\right)_0 \mathrm{e}^{i\{\Psi_n(\ell) + k_w x\}}, \tag{5.33}$$

for $k_w a \gg 1$.

5.2.3 Behavior of the transfer function when $k_w a \sim O(1)$

The approximate behavior of the transfer function when $k_w a \sim O(1)$ is obtained by the method discussed by Howe *et al.* [23] in which the surface wave on $\mathrm{S_N}$ incident on the edge A of the cavitator is approximated by the surface potential produced by the point source at N on a *flat*, infinitely extensive surface. In a first approximation at low frequencies, this potential is the same as that generated by a source on a rigid surface, for which

$$G_{\mathrm{N}}(0,\varpi) = -\frac{\mathrm{e}^{ik_w\varpi}}{2\pi\varpi}. \tag{5.34}$$

The influence on this wave of diffraction at the edge A will be assumed to be well approximated by the formula (5.32) of §5.2.2, wherein we take

$$\mathcal{G}_{\mathrm{I}} = -\frac{\mathrm{e}^{ik_w\ell}}{2\pi\ell} \tag{5.35}$$

where ℓ is defined as in equation (5.23). Therefore (5.32) yields

$$T(x,\omega) \sim \frac{-1}{2^{\frac{1}{2}}\pi^{\frac{3}{2}}a\ell}\sqrt{\frac{k_w a}{x/a}}\,\mathrm{e}^{i\left(k_w(\ell+x)-\frac{\pi}{4}\right)}, \quad k_w a \sim O(1). \tag{5.36}$$

5.3 Transfer function: Numerical results

The properties of a *compliant* cavitator are most easily demonstrated by letting $\mathcal{Z} = 1$ in the surface condition (5.4) on $\mathrm{S_N}$, corresponding to a locally reacting 'ρc surface'. The attenuation of creeping waves on $\mathrm{S_N}$ is then governed by the solutions k_n of equation (5.18)) when $\mathcal{Z} = 1$. At very high frequencies ($k_w\wp \to \infty$) the zeros are the same as those for a *pressure release* surface [37], which are determined by the roots $\zeta = -\xi_n,\ n = 1,\ 2,\ 3,\ \ldots$ of $\mathrm{Ai}(\zeta) = 0$, which are real and negative and given by [1]

$$\xi_1 = 2.33818, \quad \xi_2 = 4.08794, \quad \xi_3 = 5.52056, \quad \xi_n = \left[\frac{3\pi}{8}\Big(4n-1\Big)\right]^{\frac{2}{3}}, \ n > 3. \tag{5.37}$$

Each ξ_n determines a corresponding pole k_n given approximately by

$$\frac{k_n}{k_w} \sim 1 + \frac{\xi_n}{2}\left(\frac{2}{k_w\wp}\right)^{\frac{2}{3}}\mathrm{e}^{\frac{i\pi}{3}}, \quad n = 1,\ 2,\ 3,\ \ldots,\ k_w\wp \gg 1. \tag{5.38}$$

The exact dependencies on $k_w\wp$ of the real and imaginary parts of the solutions k_n/k_w of equation (5.18) are plotted in Figures 5.3, 5.4 for $n = 1,\ 2,\ 3$. $\mathrm{Re}(k_n) \sim k_w$ when $k_w\wp$ exceeds about 10, and $\mathrm{Im}(k_n)$ increases rapidly with n for fixed $k_w\wp$. Indeed, as a result, it is readily verified that only the first term ($n = 1$) makes a significant contribution to the sum on the right hand side of (5.33).

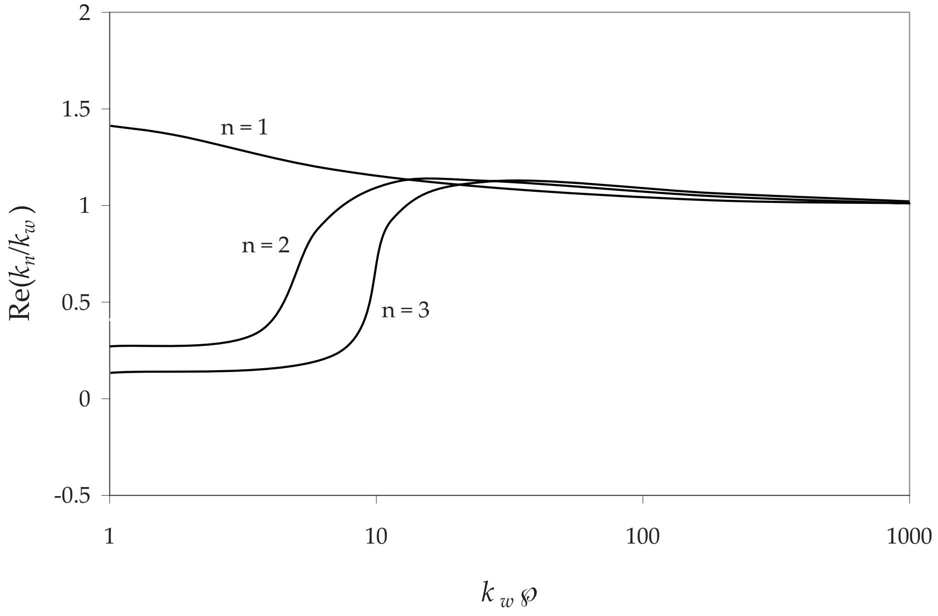

Figure 5.3. Real parts of the creeping mode wavenumbers k_n/k_w for n $=$ 1, 2, 3 for a ρc-cavitator ($\mathcal{Z} \equiv 1$)

The comparison in Figure 5.5 of the numerical solution of (5.18) and the asymptotic approximation (5.38) for this principal creeping mode ($n = 1$) indicates that (5.38) may be used when $k_w \wp > 10$. In particular it can be used to evaluate the phase $\Psi_1(\ell)$ for the first term in the expansion (5.33). To do this it is convenient to introduce the parametric representation $(x, r) = (-b\cos\phi, a\sin\phi),\ 0 < \phi < \frac{\pi}{2}$, of a point on the ellipsoidal nose (5.1). Then

$$\wp = \frac{1}{ab}(a^2\cos^2\phi + b^2\sin^2\phi)^{\frac{3}{2}}, \quad d\varpi = (a^2\cos^2\phi + b^2\sin^2\phi)^{\frac{1}{2}}\,d\phi, \tag{5.39}$$

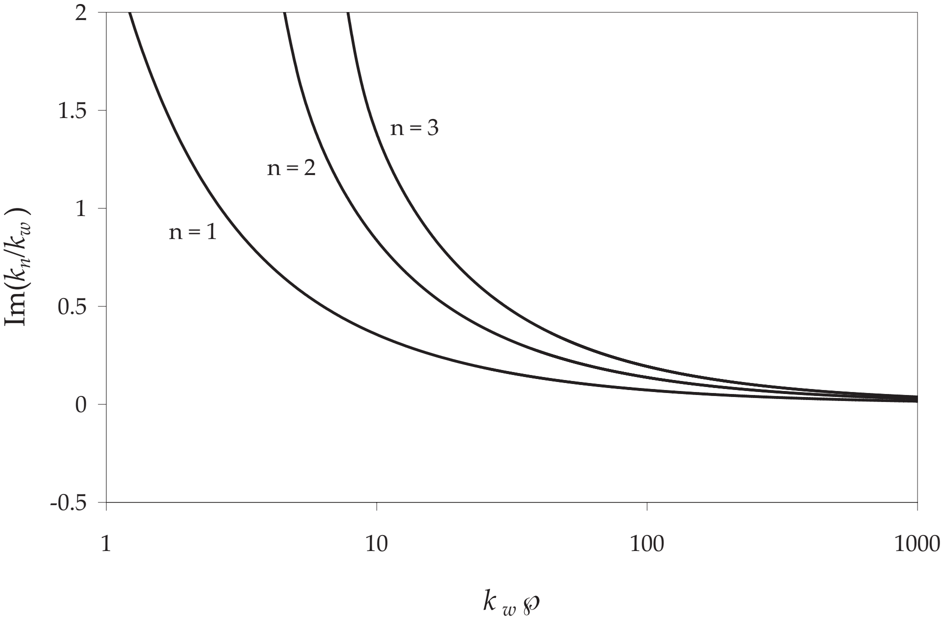

Figure 5.4. Imaginary parts of the creeping mode wavenumbers k_n/k_w for n = 1, 2, 3 for a ρc-cavitator ($\mathcal{Z} \equiv 1$)

and

$$\begin{aligned}
\Psi_1(\ell) &\approx k_w\ell + \xi_1 \left(\frac{k_w a^2}{2b}\right)^{\frac{1}{3}} \mathrm{e}^{\frac{i\pi}{3}} \int_0^{\frac{\pi}{2}} \frac{d\phi}{\sqrt{\sin^2\phi + (a^2/b^2)\cos^2\phi}} \\
&= k_w\ell + \xi_1 \left(\frac{k_w a^2}{2b}\right)^{\frac{1}{3}} \mathrm{K}\left(\sqrt{\frac{b^2 - a^2}{b^2}}\right) \mathrm{e}^{\frac{i\pi}{3}}, \qquad (5.40)
\end{aligned}$$

where K denotes the complete elliptic integral of the first kind [1].

The magnitude of the transfer function $|T(x,\omega)|$ determines the strength of the self noise at the nose N in terms of the impinging gas pressure field p_v on the cavity interface. Its variation for $k_w a \gg 1$ is given by the first mode in (5.33) in the form

$$a^2|T(x,\omega)| \approx \frac{3}{2\pi}\sqrt{\frac{a}{x}}(k_w a)^{\frac{1}{2}} \left| \frac{(k_1 a)^{\frac{1}{2}} \mathrm{e}^{i\Psi_1(\ell)}}{\frac{k_w}{k_1} - \frac{ik_1 a^2}{2b}\left(\frac{2k_w^2}{k_1^2} + 1\right)} \right| \qquad (5.41)$$

This approximation is plotted as the 'ρc-nose' curve in Figures 5.7-5.9 for a cavitator

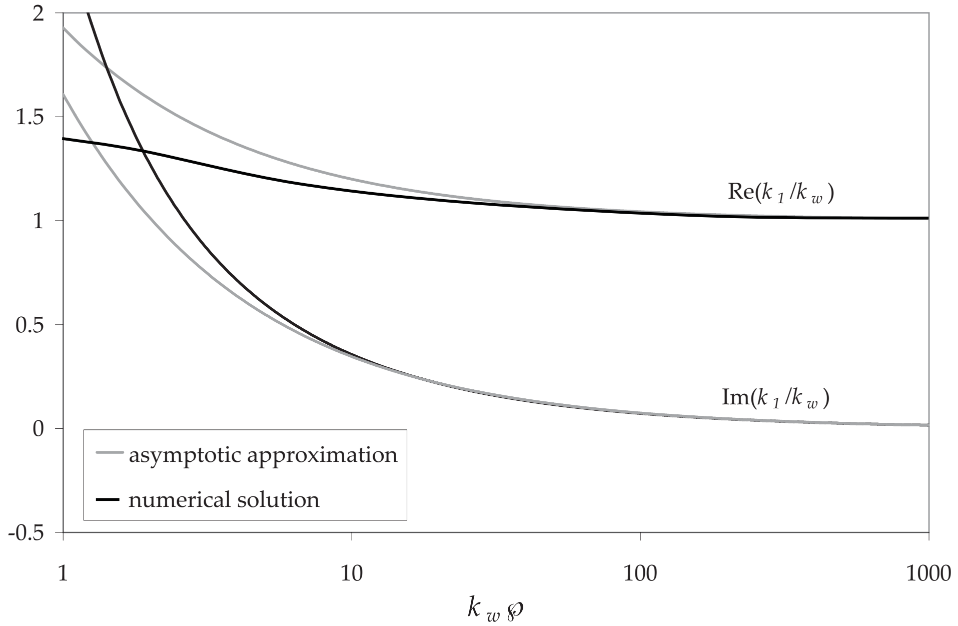

Figure 5.5. Comparison of the real and imaginary parts of k_1/k_w for a ρc cavitator determined by equation (5.18) (with $\mathcal{Z} \equiv 1$) and the asymptotic approximation (5.38) with $n = 1$.

of aspect ratio $b/a = 5/3$ and $x = a, 2a, 3a$ downstream of the edge A of the cavitator. The straight line labeled 'flat nose' in the figure is the corresponding low frequency prediction given by (5.36) (in which $\ell/a = (b/a)E(0.8) \approx 2.125$). The behavior at intermediate frequencies is estimated by a smooth interpolating curve (— — —) between these high and low frequency limits.

Figures 5.7-5.9 also depict the corresponding prediction of $|T(x,\omega)|$ for an acoustically *hard* ellipsoidal cavitator of the same aspect ratio and distances from the cavitator edge, which obtains in the formal limit $\mathcal{Z} \to \infty$. In this case equation (5.18) for the creeping mode poles reduces to

$$\mathrm{Ai}'\left\{ \mathrm{e}^{-\frac{i\pi}{3}} \left(\frac{|k|\wp}{2}\right)^{\frac{2}{3}} \left(\frac{k_w^2}{k^2} - 1\right) \right\} = 0. \tag{5.42}$$

Again only the pole k_1 in the upper half plane nearest to the real k axis makes a significant

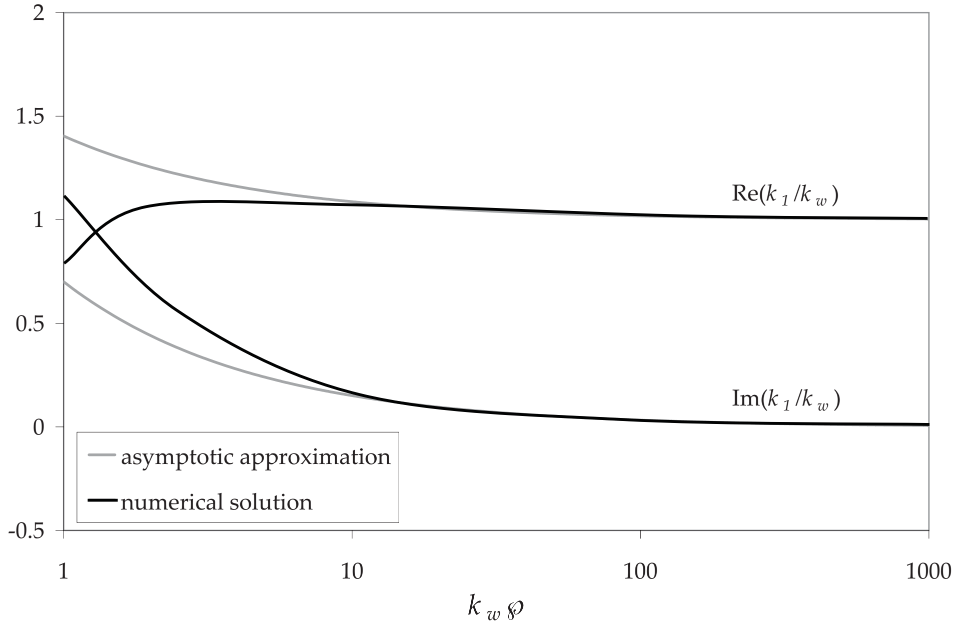

Figure 5.6. Comparison of the real and imaginary parts of k_1/k_w for an acoustically hard cavitator ($\mathcal{Z} \to \infty$) with the approximation (5.43) with $n = 1$.

contribution to the creeping wave amplitude. The calculated dependence of the real and imaginary parts of k_1/k_w on $k_w\wp$ are shown in Figure 5.6. The asymptotic approximation is given by

$$\frac{k_1}{k_w} \approx 1 + \frac{\sigma_1}{2}\left(\frac{2}{k_w\wp}\right)^{\frac{2}{3}} \mathrm{e}^{\frac{i\pi}{3}}, \quad \sigma_1 = 1.01879. \tag{5.43}$$

The zeros of $\mathrm{Ai}'(\zeta)$ lie on the negative real axis, and $\zeta = -\sigma_1$ is the root closest to the origin. The approximation (5.43) has been used to evaluate the complex phase $\Psi_1(\ell)$ for the hard cavitator, yielding

$$\Psi_1(\ell) = k_w\ell + \sigma_1\left(\frac{k_w a^2}{2b}\right)^{\frac{1}{3}} \mathrm{K}\left(\sqrt{\frac{b^2-a^2}{b^2}}\right) \mathrm{e}^{\frac{i\pi}{3}}, \tag{5.44}$$

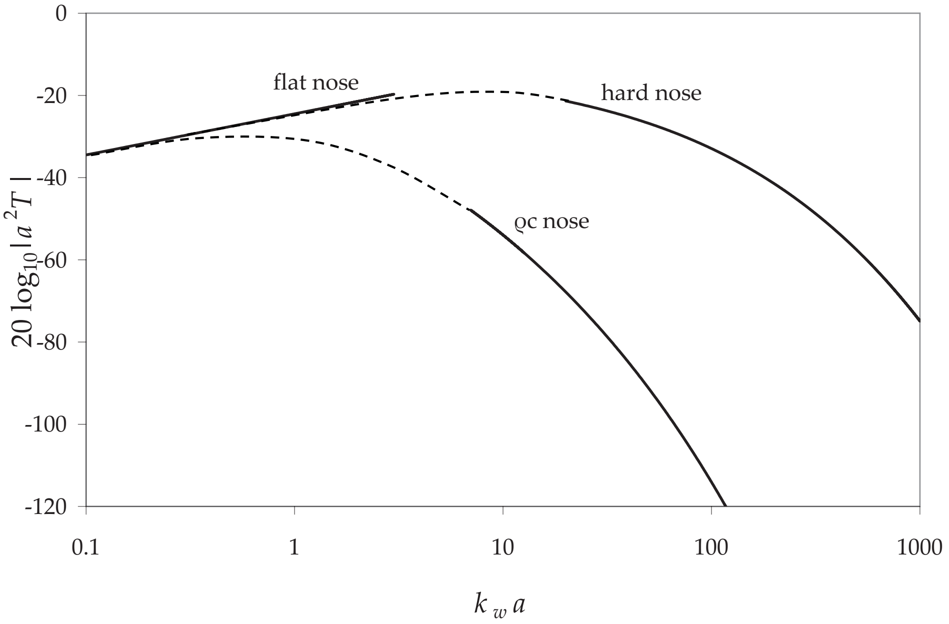

Figure 5.7. Frequency dependence of the creeping wave and low frequency ('flat nose') approximations for $20 \times \log_{10}(a^2|T|)$ (dB) at $x = a$ for an ellipsoidal cavitator of aspect ratio $b/a = 5/3$ for cases where the cavitator has a ρc-nose or is acoustically hard; the broken line curves represent possible interpolations for intermediate frequencies.

5.4 Prediction of the sound pressure spectrum at the nose

To predict the self-noise at the nose of our experimental supercavitating vehicle (Fig. 1.1) we consider that the fluctuating surface pressure p_v is generated by an axisymmetric array of 20 jets of infinitesimal cross-section discreetly impinging the surface $\mathrm{S_C}$, hence

$$p_v = \sum_{i=1}^{20} F_n(\mathbf{x}, \omega)\delta(x - x_n)\frac{\delta(\theta - \theta_n)}{a} \tag{5.45}$$

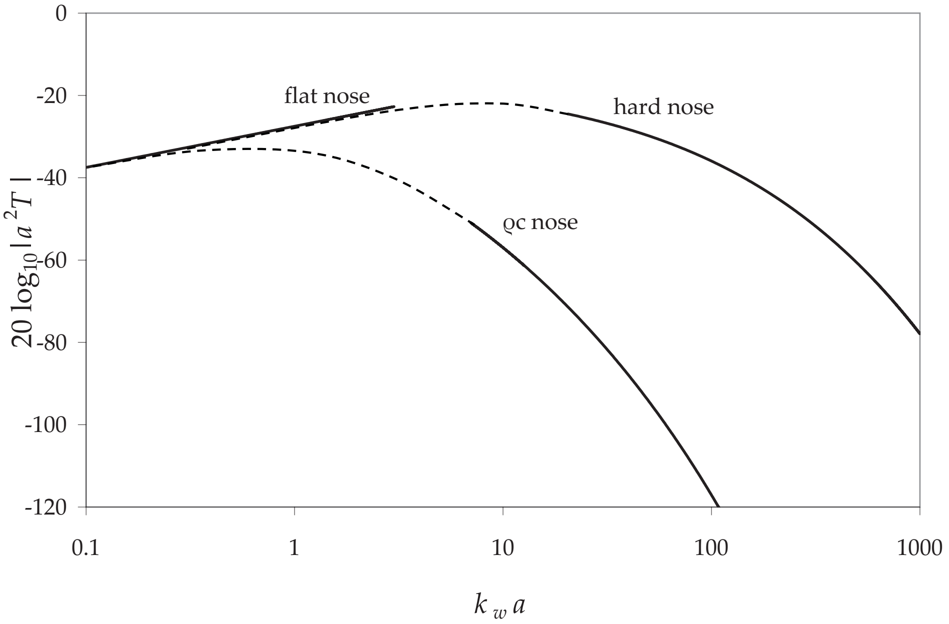

Figure 5.8. Frequency dependence of the creeping wave and low frequency ('flat nose') approximations for $20 \times \log_{10}(a^2|T|)$ (dB) at $x = 2a$ for an ellipsoidal cavitator of aspect ratio $b/a = 5/3$ for cases where the cavitator has a ρc-nose or is acoustically hard; the broken line curves represent possible interpolations for intermediate frequencies.

where F_n is the unsteady force exerted by the nth jet applied at its centroid (x_n, θ_n) and θ is the polar angle about the x-axis. Using this to approximate the integral (5.8),

$$\begin{aligned} p_N(\omega) &= \sum_{n=1}^{20} \int_S F_n(\mathbf{x},\omega)\delta(x-x_n)\delta(\theta-\theta_n)T(x,\omega)\mathrm{d}x\mathrm{d}\theta \\ &= \sum_{n=1}^{20} F_n(x_n,\theta_n,\omega)T(x_n,\omega). \end{aligned} \tag{5.46}$$

where $T(x_n, \omega)$ is the transfer function corresponding with the centroid of the nth jet. As we are interested in the spectral content of the noise at the nose $\Phi_{P,N} = \frac{1}{2\pi}\langle p_N(\omega)p_N^*(\omega)\rangle$, we multiply each side by its complex conjugate and divide by 2π to find an expression

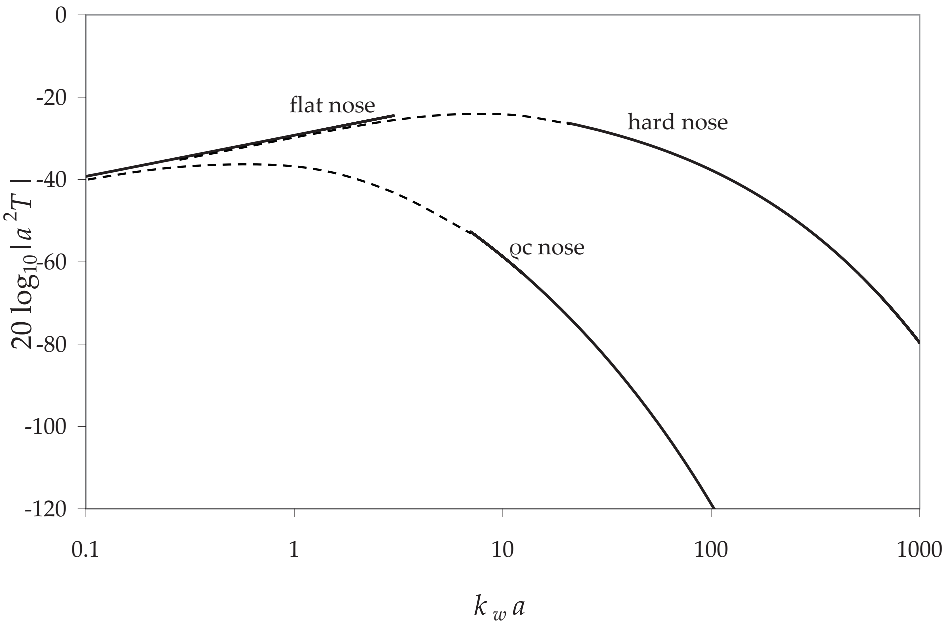

Figure 5.9. Frequency dependence of the creeping wave and low frequency ('flat nose') approximations for $20 \times \log_{10}(a^2|T|)$ (dB) at $x = 3a$ for an ellipsoidal cavitator of aspect ratio $b/a = 5/3$ for cases where the cavitator has a ρc-nose or is acoustically hard; the broken line curves represent possible interpolations for intermediate frequencies.

for the sound pressure spectrum at the nose

$$\Phi_{P,N}(\omega) = \frac{1}{2\pi} \sum_{n=1}^{20} \sum_{m=1}^{20} \langle F_n(x_n, \theta_n, \omega) F_m^*(x_n, \theta_n, \omega) \rangle T(x_n, \omega) T^*(x_m, \omega) \tag{5.47}$$

where * denotes the complex conjugate. As the jets are assumed to be statistically independent, the terms of the double summation are non-zero only if $n = m$, leaving

$$\Phi_{P,N}(\omega) = \sum_{n=1}^{20} \Phi_{FF,n}(\omega) |T(x_n, \omega)|^2 \tag{5.48}$$

where $\Phi_{FF,n}(\omega)$ is the frequency spectrum of the force exerted by the nth jet on the surface. If we consider, as in Chapter 3, that the 20 jets are statistically independent and that they are equidistant from the nose so that $x_1 = x_2 = x_3 ... x_{20} \equiv x$, then (5.48) reduces to

$$\Phi_{P,N}(\omega) = 20\Phi_{FF}(\omega)|T(x,\omega)|^2 \tag{5.49}$$

5.5 Spectrum predictions at the nose

The experimental results of §4.4 and the numerical results of §5.3 are now used in Eq. (5.49) to predict the impingement-generated sound pressure spectrum at the nose of the experimental supercavitating vehicle. Figures 5.10-5.12 present the normalized prediction for the sound pressure spectra

$$10 \times \log_{10}\left(\frac{\Phi_{P,N}(\omega)}{M\rho_A^2 U^3 a}\right)$$

versus dimensionless frequency $k_w a$ for jets located at distances $x/a = 1$, 2, and 3 aft of the cavitator edge, where $M = U/c_w$ is the Mach number of the jet relative to the sound speed in water c_w, ρ_A is the mean jet density (taken as 1.2 kg/m^3) and U is the jet impact velocity. Predictions for both the hard and compliant (ρc) nose are given using the experimentally measured $\Phi_{FF}(\omega)$ for a gas injection rate of $Q = 0.0094\,\mathrm{m}^3/\mathrm{s}$ and $\ell = 35\,\mathrm{mm}$, chosen for being the most typical parameters of ARL's model vehicle experiments. U is therefore taken as 31.1 m/s (see Table 4.2). Predictions made using the force spectrum measurements from Chapter 4 for each measured jet length and injection flow rate are presented in Appendix E.

Differences between sound at the nose for the hard and ρc nose are small at low frequencies ($k_w a < 1$), but very large at high frequencies ($k_w a \sim 10$), on the order of 30dB or more. The sound spectra all peak near $k_w a = 0.1$, with the predictions for a hard nose dropping off like $(k_w a)^{-1}$ and the predictions for the ρc nose dropping off like $(k_w a)^{-2}$. There is approximately a 2dB decrease in the sound amplitude between the predictions when the jets are one and two cavity radii away from the cavitator edge

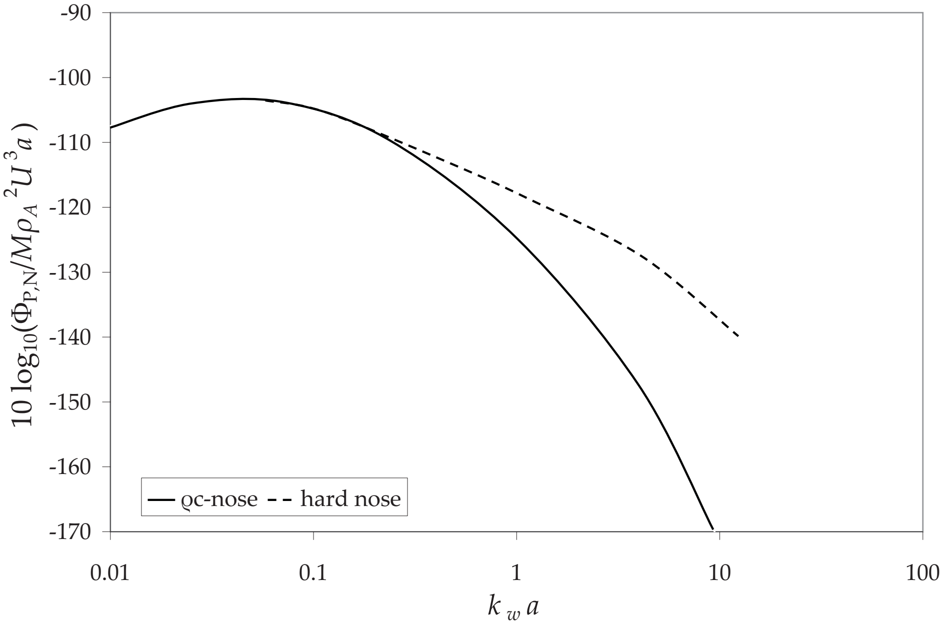

Figure 5.10. Predictions of the sound pressure at the nose when $x = a$ for an ellipsoidal cavitator of aspect ratio $b/a = 5/3$ for cases where the cavitator has a ρc-nose or is acoustically hard and gas is injected at $Q = 0.0094\,\mathrm{m}^3/\mathrm{s}$ producing jets of length 35 mm.

$(x = a, 2a)$, and a 1.5dB decrease between predictions for jets two and three cavity radii away $(x = 2a, 3a)$.

5.6 Conclusions

Comparing the predictions for the sound at the nose with the predictions for the radiated sound in the water found in Chapter 4, there is a dramatic decrease in the presence of high frequency sound at the nose, particularly for a compliant (ρc) nose section. This suggests that the high frequencies $(k_w a \geq 10)$ generated by the jet impingement source have very low amplitudes at the nose and will have negligible impact on guidance systems located forward of the cavitator.

Although we predict that high frequencies at the nose will be minimal, it is always desirable to reduce the self-noise generated in and around the supercavity. An important

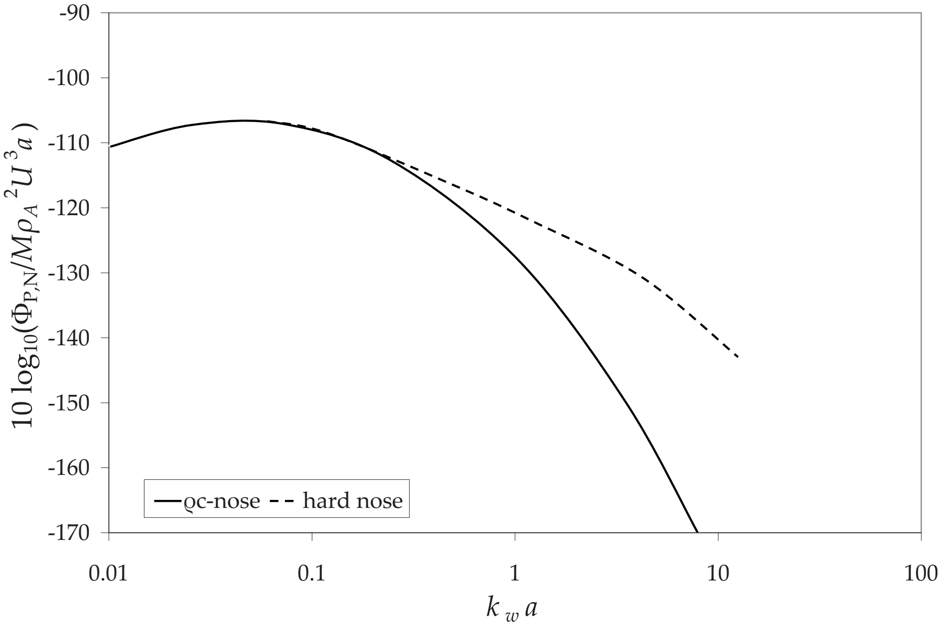

Figure 5.11. Predictions of the sound pressure at the nose when $x = 2a$ for an ellipsoidal cavitator of aspect ratio $b/a = 5/3$ for cases where the cavitator has a ρc-nose or is acoustically hard and gas is injected at $Q = 0.0094\,\mathrm{m}^3/\mathrm{s}$ producing jets of length 35 mm.

conclusion from our predictions for the sound spectrum at the nose which applies to the self-noise problem is that high frequencies are significantly damped by an acoustically soft nose; we predict, for example, a 30 dB decrease in high frequencies between the hard and compliant nose sections. Furthermore, small decreases to the amplitude of the broadband sound at the nose may be achieved by increasing the distance between the edge of the cavitator and the ventilating jets. This insight provides two strategies for reducing the high frequency noise at the nose of a supercavitating vehicle. The first is to choose the most acoustically compliant material for the nose section which still allows for transmission of guidance communications and does not inhibit the vehicles hydrodynamic performance. The second is to locate the ventilation jets as far downstream from the cavitator as possible without inhibiting the generation of the supercavity or vehicle performance.

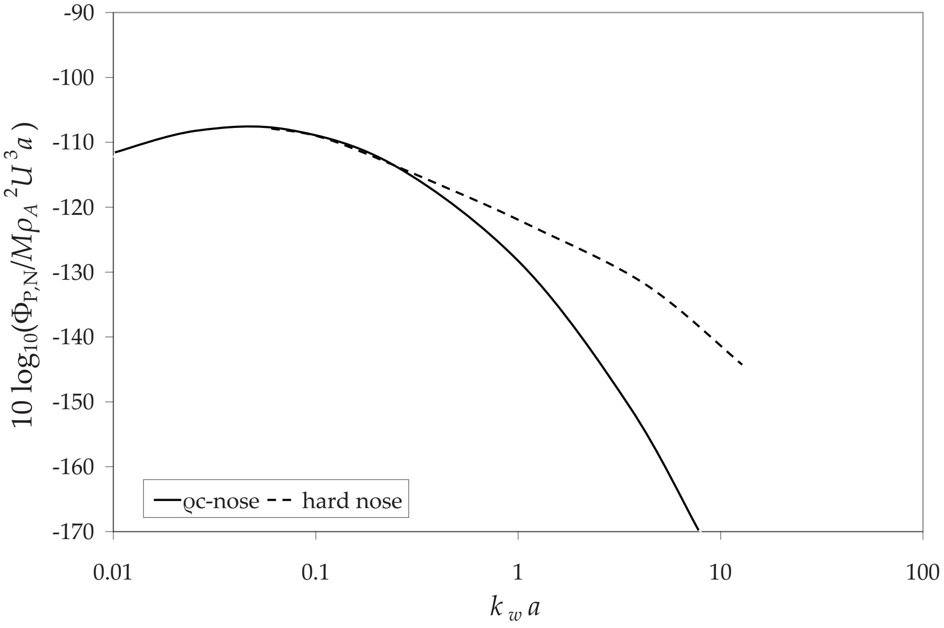

Figure 5.12. Predictions of the sound pressure at the nose when $x = 3a$ for an ellipsoidal cavitator of aspect ratio $b/a = 5/3$ for cases where the cavitator has a ρc-nose or is acoustically hard and gas is injected at $Q = 0.0094\,\mathrm{m}^3/\mathrm{s}$ producing jets of length 35 mm.

Chapter 6

Conclusions

6.1 Summary

Ventilated supercavities yield dramatic reductions in vehicle drag, but they can be a significant source of noise, some of which can inhibit successful deployment of a supercavitating underwater vehicle. The research described in this dissertation was motivated by the need to understand the contributions to this noise made by the ventilating jets of the supercavity. The problem was approached by the development of three general theoretical models for jet-cavity interaction supported by experiments. Empirical knowledge of the cavity and ventilating jets determined from a scale-model experimental vehicle were used with the theory to make specific predictions for the sound and self-noise generated by the ventilating jets.

The first theoretical problem involved an idealized, gas-filled spherical cavity whose interface was excited by a planar ring of radially projecting jets originating from a source at the sphere's center. Analysis of this configuration provided a general understanding of the directivity of the sound radiated into the water as well as the importance of cavity resonances and damping mechanisms within the cavity. It was deduced that low frequency sound emanates from the spherical cavity omni-directionally, while higher frequencies are generated by a source of dipole type, projecting sound outward and normal to the cavity at the jet impingement site. It was determined that the amplitudes of resonant cavity oscillations are controlled by sound radiation damping and by thermal and viscous losses within the cavity; it was argued that the steady exhausting of gas at the rear of a real supercavity has a negligible effect on damping. Another important conclusion was confirmation of the validity of the effective pressure release nature of the gas-water interface, which implies that the dominant source of sound radiated into the water is associated with the direct impact of the ventilating jets on the cavity interface.

The second theoretical problem examined the sound generated in the water by a turbulent gas jet of infinitesimal cross-section impinging at normal incidence on a plane gas-water interface. The acoustic spectrum was represented in terms of the unsteady force exerted on the interface by the jet. Theoretical results were combined with measurements of the force spectrum for a jet impinging on a rigid wall to predict the acoustic spectrum in the water. Results for a plane interface were then applied to develop an understanding of the sound generated for a more realistic, cylindrical cavity.

Finally, a theory was developed to estimate the high-frequency self-noise at the vehicle nose in terms of the pressure fluctuations at the cavity interface induced by the ventilating jets. This was done by deriving an asymptotic approximation for a transfer function that accounts for the diffraction of sound around an ellipsoidal surface of the vehicle nose. Numerical predictions of the transfer function revealed the important role played by the surface impedance of the nose; an acoustically hard nose results in significantly greater acoustic amplitudes at the nose than an acoustically soft or compliant nose.

It was determined that as a first approximation the supercavity interface could be treated as rigid. This allowed for empirical knowledge of the ventilating jets of an experimental supercavitating vehicle to be acquired by means of an experiment involving the measurement of the frequency spectrum of the unsteady force exerted by a gas jet on a plane, rigid surface. Results were combined with the theoretical predictions to make specific predictions of the frequency dependence and amplitude of the sound generated by a supercavitating vehicle. The experiments also confirmed an important approximation of the theoretical model, namely that the impingement source region is acoustically compact. The predictions of the sound generated by the measured supercavity jets were compared with predictions made using an independent measurement of the surface pressure on a flat plate produced by an air jet impinging at normal incidence. The close coincidence between these predictions lends valuable support for the validity of our measurement procedure.

6.2 Recommendations for future work

6.2.1 Extended experiments

The work described in this dissertation compliments experimental investigations of the acoustics of ventilated supercavities on underwater vehicles. Our predictions for the self noise at the nose should be investigated by the direct measurement of the sound at the nose of a deployed supercavitating vehicle that uses the modified gas injection system with radially projecting ventilation jets. Our results and the advanced acoustic levels produced by the impact of the jets on the cavity interface at normal incidence will help isolate impingement-generated sound from that created by other acoustic sources within and around the cavity. The experiment should be conducted using a free-running vehicle rather than one mounted in a water tunnel, where the enclosed test section creates a reverberant field that may influence the measured self-noise levels.

As the experimental supercavitating vehicles evolve in scale and design, it will be desirable to make predictions for the impingement-generated sound specific to each vehicle. The theoretical solutions are general and applicable to any cavity with a comparable injection system. If acoustic compactness of the impingement source is maintained, that is, if the jet impact diameter remains small relative to the wavelength of the relevant acoustic frequencies, the sound predictions are easily made using empirical jet and cavity information unique to each vehicle. The benchtop test described in Chapter 4 can be easily setup and quickly executed using either a vehicle jet or a stand alone jet nozzle, facilitating the production of theoretical results which compliment the acoustic investigations for each model vehicle.

A possible extension to the self-noise predictions would be the development of solutions for the self-noise generated by jets impinging at shallow incidence. This arrangement more closely represents the acoustic source present due to the traditional gas injection system on supercavitating underwater vehicles which includes gas deflectors which redirect the ventilating jets. The prediction method could again be derived in terms of the unsteady force exerted by a jet on the interface, and an analogous experiment for measuring this force could be developed. The importance of considering this more general problem will become apparent as understanding of all of the various acoustic sources in the supercavity improves. It is unlikely that a theory that uses a more realistic geometry of the gas-impingement source would reveal any new insight relevant to the problem of noise reduction; it would primarily provide a more accurate prediction for the absolute levels of the impingement-generated sound.

6.2.2 Recommendations for achieving noise reduction

This dissertation is only a first step in the complete investigation of the self-noise problem. However, it immediately provides valuable insight into the possible means of reducing the self-noise at the nose of a supercavitating vehicle. The first insight, revealed by the measurements of Chapter 4, is the relationship between ventilation gas injection rate and the amplitude of the generated sound. A doubling of the ventilation rate produces a rapid increase in generated sound power, approximately 10-15 dB. This leads us to recommend an investigation to determine the lowest gas injection rate capable of safely maintaining a stable supercavity around the underwater vehicle.

Chapter 5 demonstrated that the impedance of the cavitating nose section material has a significant impact on self-noise at the vehicle nose. Predictions for an acoustically hard cavitator were dramatically louder than those for an acoustically compliant nose. This result reinforces the importance of identifying a material for the nose which minimizes the diffraction of sound from its trailing edge without compromising the transmission of guidance system communications or hydrodynamic performance.

Another important conclusion from Chapter 5 is the demonstrated effect on the sound at the nose of the distance between the vehicle's ventilating jets and the edge of the cavitating nose section. Proximity of the jets to the nose significantly increased the magnitude of the self-noise at the nose. We therefore recommend exploring the maximum distance between the vehicle's nose section and gas injection site for which the supercavity is successfully and safely developed and maintained without adversely affecting the vehicle's hydrodynamic performance or stability.

Appendix A

Review of select topics in linear acoustics

This appendix summarizes some of the fundamentals of acoustic theory pertinent to this dissertation. The information herein is well known and included for completeness. Material is taken from Blackstock [5], Howe [18], and Pierce [37]. See these references and their bibliographies for greater detail on each topic or a more general review of the principles of linear acoustics.

A.1 The linear wave equation

The acoustic wave equation is derived from the conservation and constitutive equations which describe a fluid. We consider a fluid volume V defined by a surface S in which body forces and thermal and viscous effects are negligible. The fluid inside the volume has velocity $\mathbf{u}(\mathbf{x}, t)$, pressure $P(\mathbf{x}, t)$, and density $\rho(\mathbf{x}, t)$ at a position $\mathbf{x} = (x_1, x_2, x_3)$ and time t.

Conservation of mass requires that the increase of mass inside V must be equal to the influx of mass through S. This is expressed by the continuity equation

$$\frac{D\rho}{Dt} + \rho\nabla\cdot\mathbf{u} = 0, \tag{A.1}$$

where the material derivative $D/Dt = \partial/\partial t + \mathbf{u}\cdot\nabla$.

Conservation of momentum holds that the time rate of change of momentum inside V is equal to the sum of all forces acting on the fluid volume and the momentum flux through the surface S. Neglecting body and viscous forces, momentum conservation can be expressed by

$$\rho\frac{D\mathbf{u}}{Dt} + \nabla P = 0. \tag{A.2}$$

Finally we require an equation of state, a relationship between thermodynamic variables. We will assume that our fluid volume is isentropic, that is, the entropy s in the volume is constant, *e.g.*

$$P = P(\rho) \tag{A.3}$$

We consider that the pressure P and density ρ can be decomposed into a mean, or static, and excess constituent, such that

$$P = p_o + p, \tag{A.4}$$

$$\rho = \rho_o + \delta\rho, \tag{A.5}$$

where p_o and ρ_o are respectively the mean pressure and density in the fluid volume, $\delta\rho$ is the excess density, and p is the excess or *acoustic pressure*. This leads to the Taylor expansion of our equation of state (A.3)

$$P = p_o + A\frac{\rho-\rho_o}{\rho_o} + \frac{B}{2!}\left(\frac{\rho-\rho_o}{\rho_o}\right)^2 + \ldots \tag{A.6}$$

where A,B, etc. are empirically determined coefficients. We then introduce the sound speed c in the fluid, defined by

$$c^2 = \frac{dP}{d\rho} = \frac{A}{\rho_o} + \frac{B}{\rho_o}\frac{\rho - \rho_o}{\rho_o} + ... \tag{A.7}$$

Letting $\rho \rightarrow \rho_o$, we find that c becomes a constant c_o and that $A = \rho_o c_o^2$. Applying the decomposition (A.4, A.5), we arrive at the equation of state

$$p = c_0^2\, \delta\rho \left(1 + \frac{B}{2!A}\frac{\delta\rho}{\rho_o} + ...\right). \tag{A.8}$$

To simplify these equations, we consider that fluctuations in the fluid properties induced by sound energy are very small. In a quiet fluid, $P = p_o$, $\rho = \rho_o$, and $\mathbf{u} = \mathbf{0}$ across V. We also consider that the fluid is homogeneous, and that pressure and density are constant across the volume. We will assume that when sound is introduced the excess pressure and density and induced particle velocity are very small compared to their static values, and take the relations

$$|\delta\rho| \ll \rho_o, \tag{A.9}$$

$$|p| \ll \rho_o c_o^2, \tag{A.10}$$

$$|u| \ll c_o. \tag{A.11}$$

Applying the decomposition (A.5), we expand the continuity equation (A.1) as

$$\frac{\partial}{\partial t}(\delta\rho) + u\nabla\delta\rho + \rho_o\nabla\cdot\mathbf{u} + \delta\rho\nabla\cdot\mathbf{u} = 0. \tag{A.12}$$

Considering our small value approximations, we note that the second and fourth terms on the left-hand side (LHS) above are an order of magnitude smaller than the first and third, and are therefore considered negligible. Eliminating them, we arrived at the linearized continuity equation

$$\frac{\partial}{\partial t}(\delta\rho) + \rho_o \nabla \cdot \mathbf{u} = 0. \tag{A.13}$$

We next apply the same procedure to the conservation of momentum equation (A.2). Expanding (A.2) in terms of the decompositions of pressure and density,

$$\rho_o \frac{\partial \mathbf{u}}{\partial t} + \rho_o \mathbf{u} \cdot \nabla \mathbf{u} + \delta\rho \frac{\partial \mathbf{u}}{\partial t} + \delta\rho \mathbf{u} \cdot \nabla \mathbf{u} + \nabla p = 0. \tag{A.14}$$

As before we consider the order of each term, and find that only the first and fifth terms on the LHS are of first order. Dropping the negligible terms, the linearized conservation of momentum equation is found to be

$$\rho_o \frac{\partial \mathbf{u}}{\partial t} + \nabla p = 0. \tag{A.15}$$

The equation of state (A.8) is linearized by inspection of its terms, yielding

$$p = c_o^2 \delta\rho. \tag{A.16}$$

Using this to eliminate $\delta\rho$ from the linearized continuity equation (A.13),

$$\frac{1}{c_o^2}\frac{\partial p}{\partial t} + \rho_o \nabla \cdot \mathbf{u} = 0. \tag{A.17}$$

Taking the difference of the time derivative of this equation with the spatial derivative of the linearized momentum equation (A.15) results in the linear acoustic wave equation

$$\left(\frac{1}{c_0^2}\frac{\partial^2}{\partial t^2} - \nabla^2 \right) p = 0. \tag{A.18}$$

It is often convenient to consider sound transmission in the frequency domain rather than the time domain. The wave equation is easily brought into the frequency domain by applying a Fourier transform, yielding the Helmholtz equation

$$(k_o^2 + \nabla^2)p = 0, \tag{A.19}$$

where the acoustic wavenumber $k_o = \omega / c_o$ and ω is angular frequency.

Now we will consider a fluid volume which contains an acoustic source. The source can be considered to add a volume source to the right side of the continuity equation (A.13) and a force term to the right side of the momentum equation (A.15). Carrying these terms through the above derivation yields

$$\left(\frac{1}{c_0^2} \frac{\partial^2}{\partial t^2} - \nabla^2 \right) p = \mathcal{F}(\mathbf{x}, t) \tag{A.20}$$

where the volume and force terms have been replaced by a generalized pressure source $\mathcal{F}(\mathbf{x}, t)$. This result is known as the *inhomogeneous* wave equation.

The radiation condition In general, solutions of the wave equation and Helmholtz equation can be decomposed into two parts which respectively describe an outgoing, or forward-traveling wave and an incoming, or backward-traveling wave. Let us consider a fluid at rest. At time $t = 0$, an acoustic source begins to generate sound in the fluid. Causality requires that for $t > 0$ the wave energy from the source radiates *outward* and, in the absence of other sources or bodies, there is no incoming energy. The consideration that all incoming solutions of the wave equation must therefore be identically zero is known as the *radiation condition*.

A.2 Acoustic impedance, intensity, and power

Acoustic impedance quantifies the sound absorption of a fluid. It is defined as the ratio of acoustic pressure to the particle velocity in the fluid. For an outgoing wave, the characteristic impedance Z_o of a medium is given as

$$Z_o = \frac{p}{u} = \rho_o c_o. \tag{A.21}$$

Rigid walls and pressure release surfaces A medium is considered acoustically *hard* or rigid if its impedance $Z \to \infty$. A normally incident plane wave traveling through a medium with impedance Z_1 is reflected back in its entirety when it reaches a medium of impedance Z_2 when $Z_1 \ll Z_2$. If instead $Z_1 \gg Z_2$, there is again no transmission and the reflected wave identically cancels the incident wave; the interface between two such media is termed a *pressure release* surface, so named because the acoustic pressure there is identically zero. Media whose impedance $Z \to 0$ are considered *compliant*, or acoustically *soft*.

Acoustic intensity is the time average of the sound energy flow through a unit area in the direction normal to that area. In integral form, acoustic intensity $\mathbf{I}$ is found as

$$\mathbf{I} = \frac{1}{t_{av}} \int_0^{t_{av}} p\mathbf{u} dt. \tag{A.22}$$

The *directivity* of radiated sound is determined by the dependence of intensity on the direction in which it is calculated. For sound which radiates omnidirectionally, intensity on a spherical surface of radius r simplifies, applying the definition of impedance, to a scalar quantity

$$I = \frac{p(r)^2}{\rho_o c_o}. \tag{A.23}$$

Finally, the acoustic power W passing through any surface S in the fluid is the integral of the sound intensity over that surface, so

$$W = \int_S \mathbf{I} \mathrm{d}\mathbf{S}'. \tag{A.24}$$

where S' is a differential element of the surface S. For omnidirectional sound, the power through a sphere of radius r reduces to

$$W = 4\pi r^2 I. \tag{A.25}$$

Appendix B

Advanced topics from aeroacoustics

This appendix provides a brief overview of select topics from aeroacoustics pertinent to this dissertation and is included for completeness. Material is taken from Howe's *Acoustics of Fluid-Structure Interactions* [18], *Theory of Vortex Sound* [20], and *Hydrodynamics and Sound* [22].

B.1 Acoustic compactness and the near and far fields

An acoustic source occupying a fluid region of characteristic dimension ℓ and frequency ω radiates sound of wavelength $2\pi c_o/\omega$. The source is considered *acoustically compact* when ℓ is much smaller than this wavelength, or $\omega\ell/c_o \equiv k_o\ell \ll 1$. The acoustic *far field* exists at points $|\mathbf{x}|$ (taking the origin of coordinates at the source) many wavelengths from the source, or where $k_o|\mathbf{x}| \gg 1$. The *near field* is thus that region in the immediate vicinity of the source, for which $k_o \leq 1$.

Monopoles, dipoles, and quadrupoles A *monopole* is an acoustic source which can be considered analogous to a pulsating sphere. Sound radiates from the source omnidirectionally, diminishing in the far field (as $|\mathbf{x}| \to \infty$) like $\frac{1}{|\mathbf{x}|}$. A general expression for a monopole is a source of the form $q(t)\delta(\mathbf{x})$, where $q(t)$ is the 'strength' of the source.

A *dipole* is source of the form $\frac{\partial}{\partial x_j}\left[f_j(t)\delta(\mathbf{x})\right]$ with strength $f_j(t)$. As a monopole can be likened to a pulsating sphere, a dipole is analogous to an oscillating sphere. Sound emanates from the source as two lobes protruding in the direction of that oscillation (see Figure B.1), diminishing like $\frac{1}{|\mathbf{x}|^2}$ in the far field. A point dipole is also equivalent to two monopoles of opposite strength a short distance apart.

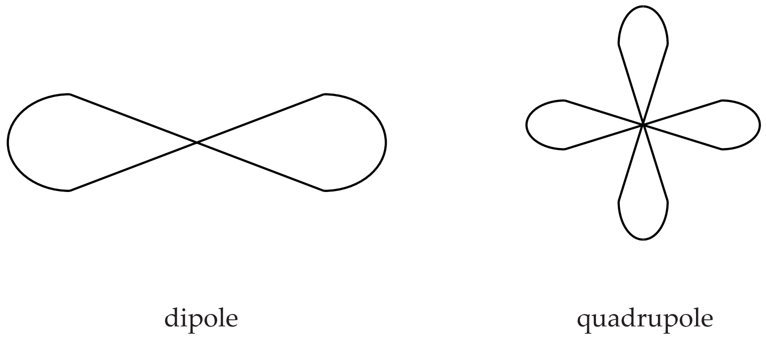

Figure B.1. Directivity of the sound from a dipole and quadrupole source

A source distribution equivalent to four monopoles (whose net source strength is zero) is called a *quadrupole*. A quadrupole source has the general form $\frac{\partial^2 T_{ij}}{\partial x_i \partial x_j}(\mathbf{x}, t)$, and in the far field its generated sound diminishes like $\frac{1}{|\mathbf{x}|^3}$. The directivity of a quadrupole is depicted in Fig. B.1.

In general, any acoustic source can be represented as the sum of component sources of monopole, dipole, quadrupole, and higher-order pole strength. Typically it is necessary only to consider the leading order term when determining the radiated acoustic pressure generated by the source.

B.2 Aerodynamic sound

The sound generated by vorticity in an unbounded fluid is called *aerodynamic sound*. Lighthill [32] developed the theory of vortex sound by reformulating the Navier-Stokes equation into an exact, inhomogeneous wave equation whose source terms are important only within the turbulent (vortical) region. It was determined that the solution in a real fluid for the density fluctuations $\delta\rho$ in the far-field from a vortical acoustic source is equivalent to the solution in an ideal fluid which is forced by a stress distribution T_{ij}, the *Lighthill stress tensor*. This is known as *Lighthill's acoustic analogy*. Including this stress term in the momentum equation used to derive the acoustic wave equation (see Appendix A) yields *Lighthill's equation*:

$$\left(\frac{1}{c_o^2}\frac{\partial^2}{\partial t^2} - \nabla^2\right) c_o^2 \delta\rho = \frac{\partial T_{i,j}}{\partial x_i \partial x_j}. \tag{B.1}$$

The problem of calculating aerodynamic sound in a real fluid is therefore found to be equivalent to solving this equation for the radiation of sound in an ideal fluid produced by a distribution of *quadrupole* sources whose strength per unit volume is Lighthill's stress tensor T_{ij}.

B.3 Acoustic Green's function

The Green's function is an important tool for solving inhomogeneous wave equations. The *free-space Green's function* is the outgoing solution of the wave equation generated by the point source $\delta(\mathbf{x}-\mathbf{y})\delta(t-\tau)$ in an unbounded fluid located at a point $\mathbf{x}=\mathbf{y}$ and a time $t=\tau$. Expressed mathematically,

$$\left(\frac{1}{c_o^2}\frac{\partial^2}{\partial t^2} - \nabla^2\right) G = \delta(\mathbf{x}-\mathbf{y})\delta(t-\tau) \tag{B.2}$$

where $G = 0$ for $t < \tau$. This has the solution

$$G(\mathbf{x}, \mathbf{y}, t-\tau) = \frac{1}{4\pi|\mathbf{x}-\mathbf{y}|}\delta\left(t - \tau - \frac{|\mathbf{x}-\mathbf{y}|}{c_o^2}\right). \tag{B.3}$$

The inhomogeneous wave equation

$$\left(\frac{1}{c_o^2}\frac{\partial^2}{\partial t^2} - \nabla^2\right) p = \mathcal{F}(\mathbf{x}, t) \tag{B.4}$$

describes the behavior of waves generated by a distributed source $\mathcal{F}(\mathbf{x}, t)$. This source can be regarded as an array of point sources, such that

$$\mathcal{F}(\mathbf{x}, t) = \int\int_{-\infty}^{\infty} \mathcal{F}(\mathbf{y}, \tau)\delta(\mathbf{x}-\mathbf{y})\delta(t-\tau)d^3\mathbf{y}d\tau. \tag{B.5}$$

The solution for each constituent source of strength $\mathcal{F}(\mathbf{y}, \tau)\delta(\mathbf{x}-\mathbf{y})\delta(t-\tau)d^3\mathbf{y}d\tau$ is $\mathcal{F}(\mathbf{y}, \tau)G(\mathbf{x}, \mathbf{y}, t-\tau)d^3\mathbf{y}d\tau$. Adding up these individual contributions we obtain

$$\begin{aligned} p(\mathbf{x}, t) &= \int\int_{-\infty}^{\infty} \mathcal{F}(\mathbf{y}, \tau)G(\mathbf{x}, \mathbf{y}, t-\tau)d^3\mathbf{y}d\tau & \text{(B.6)} \\ &= \frac{1}{4\pi}\int\int_{-\infty}^{\infty} \frac{\mathcal{F}(\mathbf{y}, \tau)}{|\mathbf{x}-\mathbf{y}|}\delta\left(t-\tau-\frac{|\mathbf{x}-\mathbf{y}|}{c_o^2}\right) d^3\mathbf{y}d\tau & \text{(B.7)} \\ &= \frac{1}{4\pi}\int_{-\infty}^{\infty} \frac{\mathcal{F}\left(\mathbf{y}, t-\frac{|\mathbf{x}-\mathbf{y}|}{c_o^2}\right)}{|\mathbf{x}-\mathbf{y}|}d^3\mathbf{y}. & \text{(B.8)} \end{aligned}$$

Green's functions can be applied to more general acoustic problems involving solid or fluid boundaries, and have equivalent expressions in both the time and frequency domains. To demonstrate the use of Green's functions in a general problem, we will consider a simple example involving the solution of the homogeneous Helmholtz equation. We consider an acoustic source on the boundary of a volume of fluid defined by some surface S. The source generates an acoustic pressure $p(\mathbf{x}, \omega)$ within the fluid volume which satisfies

$$(\nabla^2 + k_o^2)p = 0 \tag{B.9}$$

subject to some boundary condition $p = p'(\mathbf{x}, \omega)$ on S. We then introduce a Green's function $G(\mathbf{x}, \omega)$ with outgoing wave behavior,

$$(\nabla^2 + k_o^2)G = 0 \tag{B.10}$$

with the boundary condition $G = G'(\mathbf{x}, \omega)$ on S. Taking the difference of $G\cdot$(B.9) and $p\cdot$(B.10),

$$p\nabla^2 G - G\nabla^2 p = 0. \tag{B.11}$$

Integrating over the fluid volume V,

$$\int_V (p\nabla^2 G - G\nabla^2 p)\,\mathrm{d}V = 0. \tag{B.12}$$

Introducing the vector identities

$$p\nabla^2 G = \nabla^2(pG) - \nabla\cdot(G\nabla p) - \nabla G\cdot\nabla p, \tag{B.13}$$

$$G\nabla^2 p = \nabla^2(Gp) - \nabla\cdot(p\nabla G) - \nabla p\cdot\nabla G \tag{B.14}$$

into the integrand we find

$$\int_V [\nabla\cdot(p\nabla G) - \nabla\cdot(G\nabla p)]\,\mathrm{d}V = 0. \tag{B.15}$$

Applying the divergence theorem, this reduces to

$$\int_V [\nabla\cdot(p\nabla G) - \nabla\cdot(G\nabla p)]\,\mathrm{d}V = \oint_S \left[p\frac{\partial G}{\partial x_n} - G\frac{\partial p}{\partial x_n}\right]\mathrm{d}S = 0 \tag{B.16}$$

where x_n is the vector outward normal to the surface S. The acoustic pressure p is then solved for by substitution into the integrand of the Green's function G and the boundary conditions on S specific to the problem's geometry and source parameters.

B.3.1 The reciprocal theorem

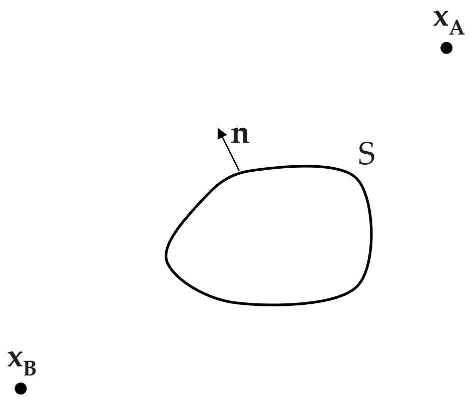

Figure B.2. Reciprocal acoustic problems of equal point sources at $\mathbf{x_A}$ and $\mathbf{x}_B$.

An important and very useful concept in the application of Green's functions for solving acoustic problems is the *reciprocal theorem.* We consider two acoustic problems in which sound is generated in a fluid by two point sources at $\mathbf{x} = \mathbf{x}_A$ and $\mathbf{x} = \mathbf{x}_B$ in the presence of a solid body defined by a surface S. The Green's functions $G(\mathbf{x}, \mathbf{x}_A, \omega), G(\mathbf{x}, \mathbf{x}_B, \omega)$ which determine the acoustic pressure generated by each respective source are defined by

$$(\nabla^2 + k_o^2)G(\mathbf{x}, \mathbf{x}_A, \omega) = \delta(\mathbf{x} - \mathbf{x}_A) \tag{B.17}$$

$$(\nabla^2 + k_o^2)G(\mathbf{x}, \mathbf{x}_B . \omega) = \delta(\mathbf{x} - \mathbf{x}_B) \tag{B.18}$$

subject to the boundary conditions on S

$$\frac{\partial G}{\partial x_n}(\mathbf{x}, \mathbf{x}_A, \omega) = \frac{G(\mathbf{x}, \mathbf{x}_A, \omega)}{Z(\mathbf{x}, \omega)}, \quad \frac{\partial G}{\partial x_n}(\mathbf{x}, \mathbf{x}_B, \omega) = \frac{G(\mathbf{x}, \mathbf{x}_B, \omega)}{Z(\mathbf{x}, \omega)}, \tag{B.19}$$

where x_n is the vector normal to the surface S directed into the fluid and $Z(\mathbf{x}, \omega)$ is the surface impedance on S. Mathematically stated, the reciprocal theorem holds that

$$G(\mathbf{x}_A, \mathbf{x}_B) = G(\mathbf{x}_B, \mathbf{x}_A), \tag{B.20}$$

that is, the acoustic pressure at $\mathbf{x}_A$ produced by the point source at $\mathbf{x}_B$ is equal to the acoustic pressure at $\mathbf{x}_B$ produced by an equal point source at $\mathbf{x}_A$. The reciprocal theorem is particularly useful for simplifying acoustic problems in which the geometry local to either the source or the point of interest complicates finding their solutions.

B.3.2 Method of images

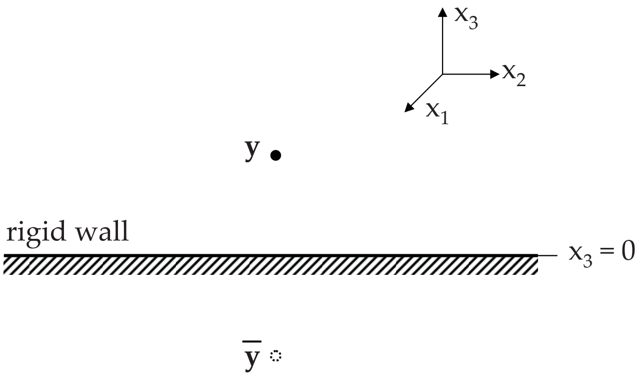

Figure B.3. Acoustic image problem

Another important concept in applying Green's functions is the method of images. Let us consider an acoustic source at a point $\mathbf{y}$ near an infinite rigid wall $x_3 = 0$. Recognizing that the acoustic pressure on the wall vanishes, we can choose to reformulate the problem by removing the wall and introducing a source of equal and opposite strength located at the image point $\bar{\mathbf{y}}$ of the original source in the wall, that is, its reflection through the plane $x_2 = 0$; the sound generated from the image source identically cancels that generated by the original source along $x_2 = 0$, maintaining the boundary condition of the original problem. This is applied in the use of Green's functions by letting the Green's function G for the source near the wall be represented as the sum of the free-space Green's functions G' for the sources at the original point and the image point, or

$$G(\mathbf{x}, \mathbf{y}, \omega) = G'(\mathbf{x}, \mathbf{y}, \omega) - G'(\mathbf{x}, \bar{\mathbf{y}}, \omega). \tag{B.21}$$

Appendix C

Garfield Thomas Water Tunnel

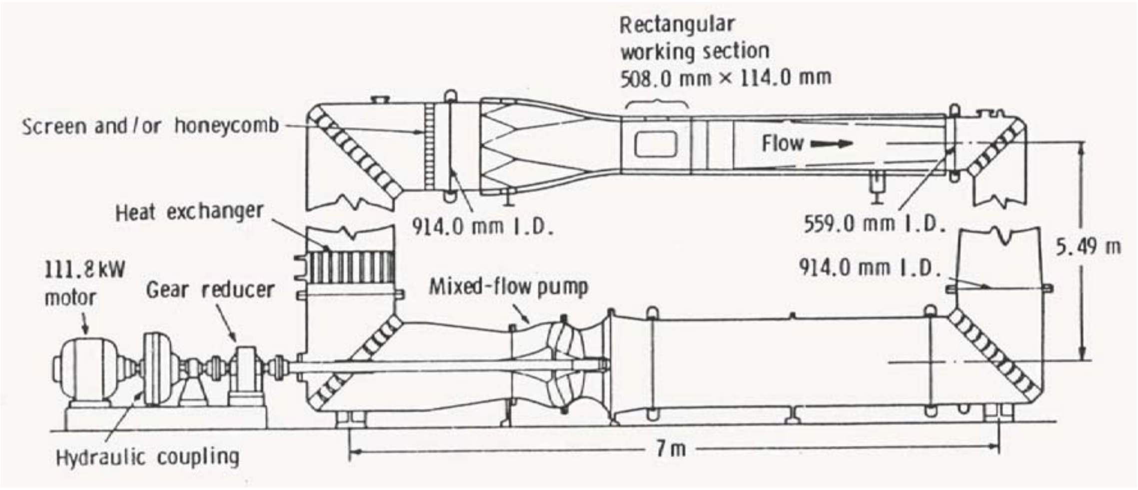

Figure C.1. Schematic of the ARL 0.3048-m diameter water tunnel facility

Experiments using the model supercavitating vehicle are conducted inside ARL's 0.3048 m-diameter water tunnel facility. The tunnel is a closed circuit, closed jet system which can achieve velocities up to 24.38 m/s under absolute pressures ranging between 20.7 and 413.7 kPa. The flow is controlled by a mixed flow peerless pump driven by a 111.8 kW motor. The tunnel accomodates two test sections, a rectangular section measuring 508 mm by 114.3 mm by 762 mm long (shown above), and a cylindrical test section measuring 304.8 mm in diameter by 762 mm long. The cylindrical test section is used for the supercavitating vehicle tests.

Appendix D

Equipment Specifications

This appendix presents the pertinent specifications for transducers and electronics used in the jet impact force experiment. These include the unsteady force sensor, accelerometer, velocimeter, flowmeter, signal conditioner, and data acquisition hardware.

D.1 Unsteady force transducer

Model	PCB 208C01
Frequency Response	0.01 to 36000 Hz
Resolution	0.00045 N-rms
Measurement Range	44.48 N
Nominal Sensitivity	112.4 mV/N

Table D.1. Force transducer specifications

D.2 Accelerometer

Model	PCB 352B10
Frequency Response	1 to 17000 Hz
Resonant Frequency	$\geq$ 65 kHz
Nominal Sensitivity	10 mV/g

Table D.2. Accelerometer specifications

D.3 Velocimeter

Model	TSI 8345
Velocity Range	0 to 30 m/s
Temperature Range	-17.8 to 93.3°C
Velocity Sensitivity	3% or ±0.15 m/s,whichever is greater
Temperature Sensitivity	± 0.3°C

Table D.3. VelociCalc specifications

This velocimeter is calibrated annually by the manufacturer.

D.4 Flowmeter

Model	Sierra Instruments 780S-NAA-N5-E2-P3-V1-DD-MP-SR
Accuracy	±1%

Table D.4. Flowmeter specifications

This flowmeter is calibrated annually by the manufacturer.

D.5 Signal Conditioner

Model	PCB 480B21
Frequency Range	0.15 to 100 kHz
Voltage Gain (± 2%)	1:1
(± 2%)	1:10
(± 2%)	1:100
Spectral Noise (1 Hz)(Gain x1)	-128 dB
Spectral Noise (10 Hz)(Gain x1)	-140 dB
Spectral Noise (100 Hz)(Gain x1)	-144 dB
Spectral Noise (1 kHz)(Gain x1)	-147 dB
Spectral Noise (10 kHz)(Gain x1)	-148 dB
Broadband Electrical Noise (1 to 10 kHz)(Gain x1)	-110 dB/rms
Spectral Noise (1 Hz)(Gain x10)	-115 dB
Spectral Noise (10 Hz)(Gain x10)	-118 dB
Spectral Noise (100 Hz)(Gain x10)	-122 dB
Spectral Noise (1 kHz)(Gain x10)	-123 dB
Spectral Noise (10 kHz)(Gain x10)	-129 dB
Broadband Electrical Noise (1 to 10 kHz)(Gain x10)	-86 dB/rms

Table D.5. Signal conditioner specifications

D.6 Data Acquisition System

Model	DSP Technologies SigLab 50-21
Frequency Response	0 to 50 kHz

Table D.6. SigLab hardware specifications

Computer: Dell Latitude D820 laptop computer

Software: Siglab Dynamic Signal Analyzer (VNA) v3.2

Appendix E

Extended experimental results and sound predictions

This appendix presents all of the unsteady force spectra measured during the experiment of Chapter 4. Each test using the parameters of injection rate Q and jet length ℓ (see 4.1) was repeated three times; we herein refer to these as runs A, B, and C. Also included are the subsequent predictions of the impingement-generated sound power spectra, as in §4.5 for each data set. An example of the prediction for the self-noise spectra at the vehicle nose (as in §5.5) is given for each set of jet parameters ℓ and Q.

E.1 Measured force spectra (§4.4)

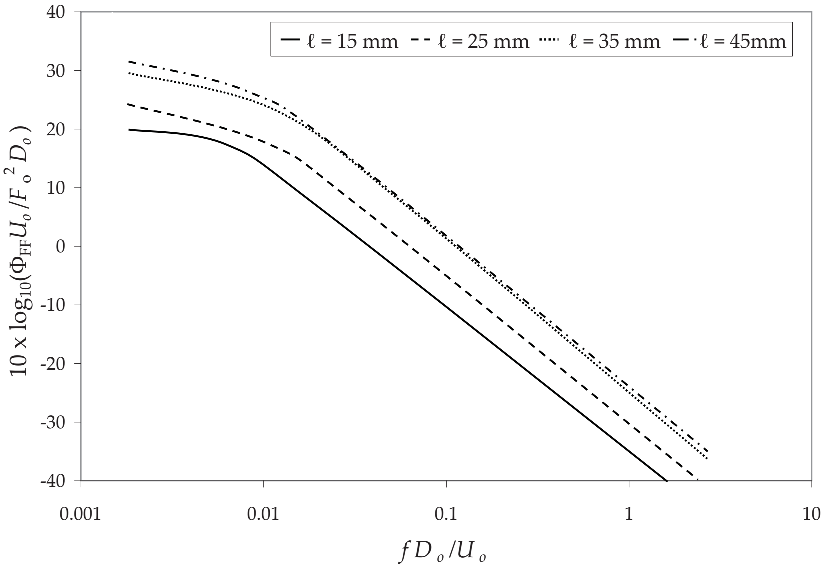

Figure E.1. Measured force spectra for jets of gas injection rate $Q = 0.0047$ m^3/s and jet lengths $\ell = 15$, 25, 35, and 45 mm, run A, normalized to mean force F_o in 15.6 Hz bins, versus dimensionless frequency fD_o/U_o.

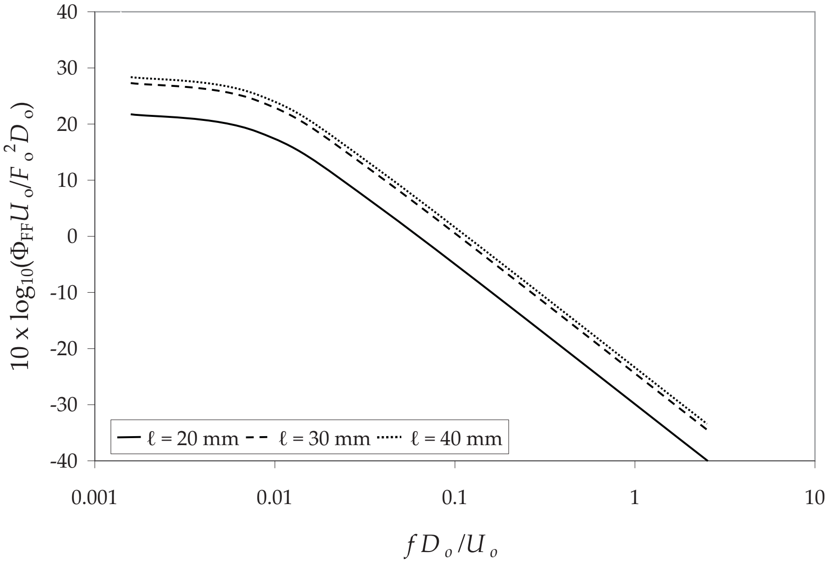

Figure E.2. Measured force spectra for jets of gas injection rate $Q = 0.0047$ m^3/s and jet lengths $\ell = 20$, 30, and 40 mm, run A, normalized to mean force F_o in 15.6 Hz bins, versus dimensionless frequency fD_o/U_o.

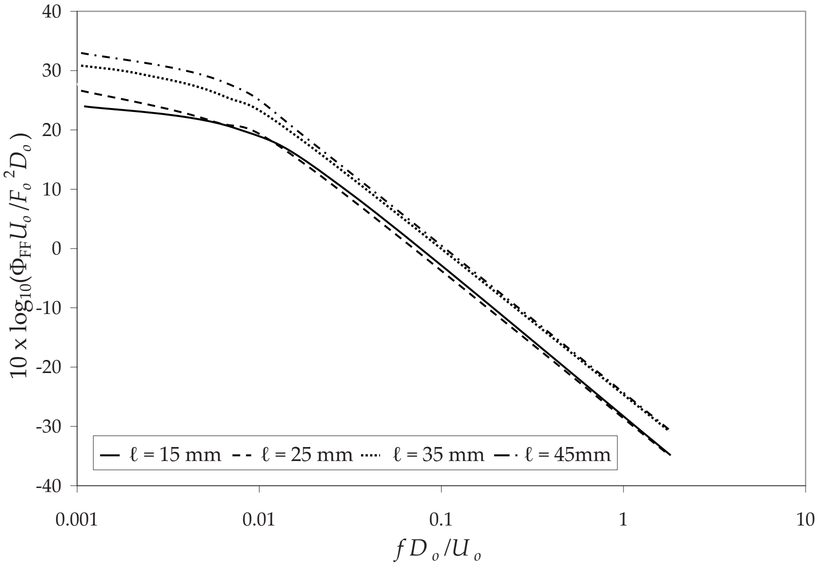

Figure E.3. Measured force spectra for jets of gas injection rate $Q = 0.0071$ m^3/s and jet lengths $\ell = 15$, 25, 35, and 45 mm, run A, normalized to mean force F_o in 15.6 Hz bins, versus dimensionless frequency fD_o/U_o.

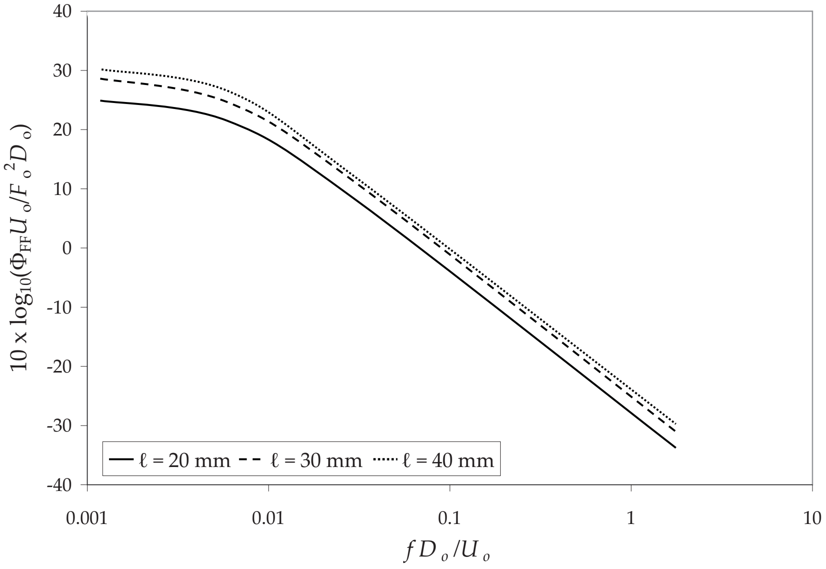

Figure E.4. Measured force spectra for jets of gas injection rate $Q = 0.0071$ m^3/s and jet lengths $\ell = 20$, 30, and 40 mm, run A, normalized to mean force F_o in 15.6 Hz bins, versus dimensionless frequency fD_o/U_o.

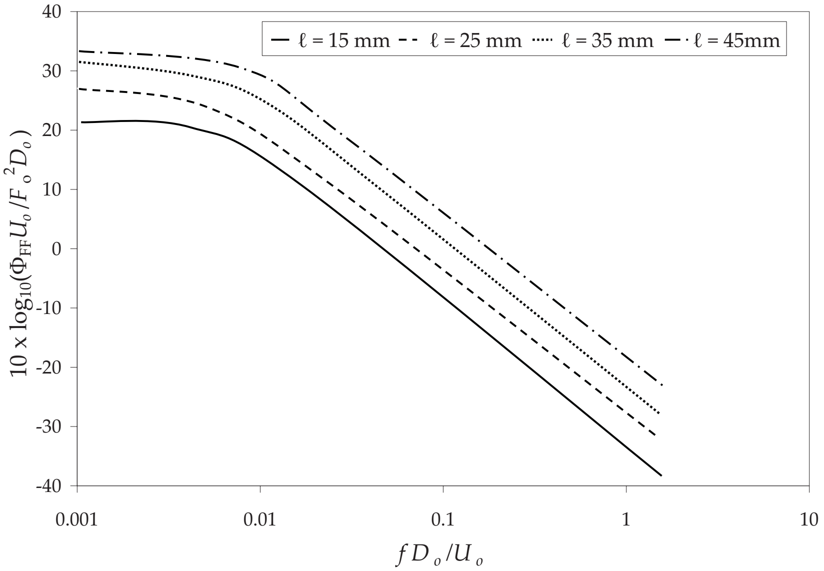

Figure E.5. Measured force spectra for jets of gas injection rate $Q = 0.0094$ m^3/s and jet lengths $\ell = 15$, 25, 35, and 45 mm, run A, normalized to mean force F_o in 15.6 Hz bins, versus dimensionless frequency fD_o/U_o.

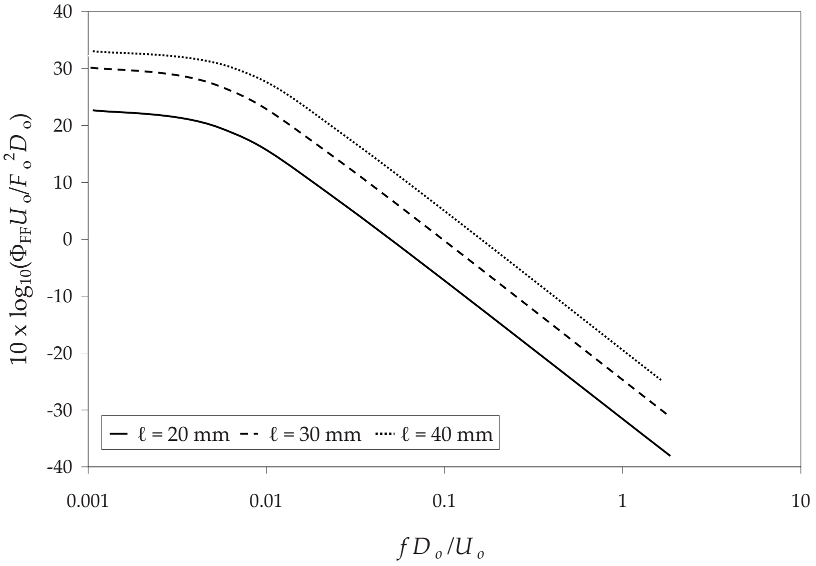

Figure E.6. Measured force spectra for jets of gas injection rate $Q = 0.0094$ m^3/s and jet lengths $\ell = 20$, 30, and 40 mm, run A, normalized to mean force F_o in 15.6 Hz bins, versus dimensionless frequency fD_o/U_o.

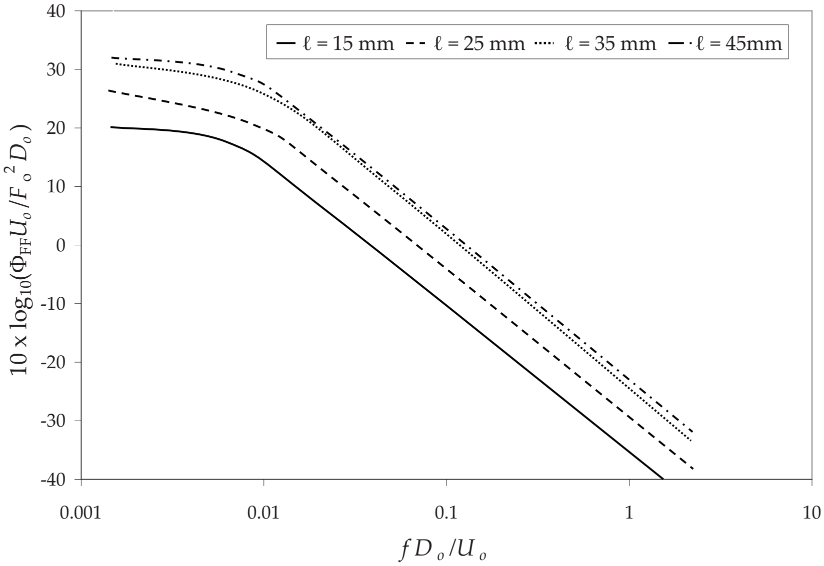

Figure E.7. Measured force spectra for jets of gas injection rate $Q = 0.0047$ m^3/s and jet lengths $\ell = 15$, 25, 35, and 45 mm, run B, normalized to mean force F_o in 15.6 Hz bins, versus dimensionless frequency fD_o/U_o.

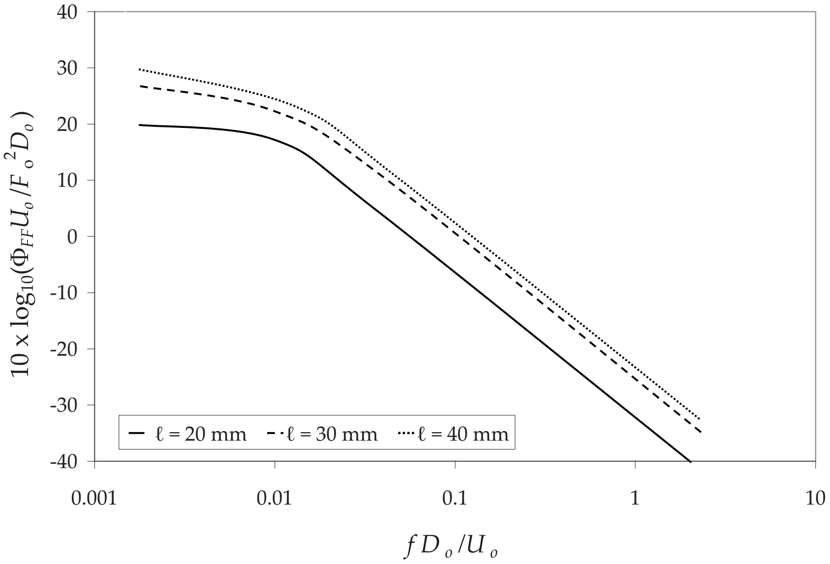

Figure E.8. Measured force spectra for jets of gas injection rate $Q = 0.0047$ m^3/s and jet lengths $\ell = 20$, 30, and 40 mm, run B, normalized to mean force F_o in 15.6 Hz bins, versus dimensionless frequency fD_o/U_o.

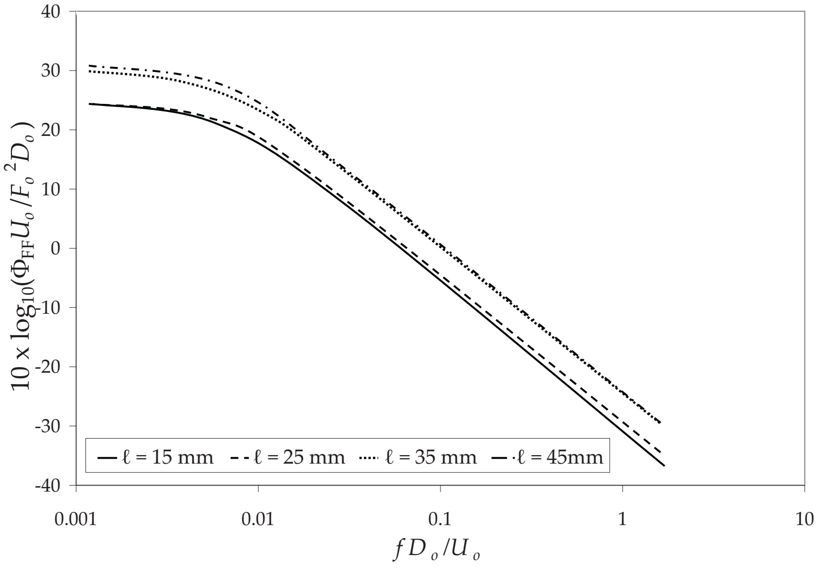

Figure E.9. Measured force spectra for jets of gas injection rate $Q = 0.0071$ m^3/s and jet lengths $\ell = 15$, 25, 35, and 45 mm, run B, normalized to mean force F_o in 15.6 Hz bins, versus dimensionless frequency fD_o/U_o.

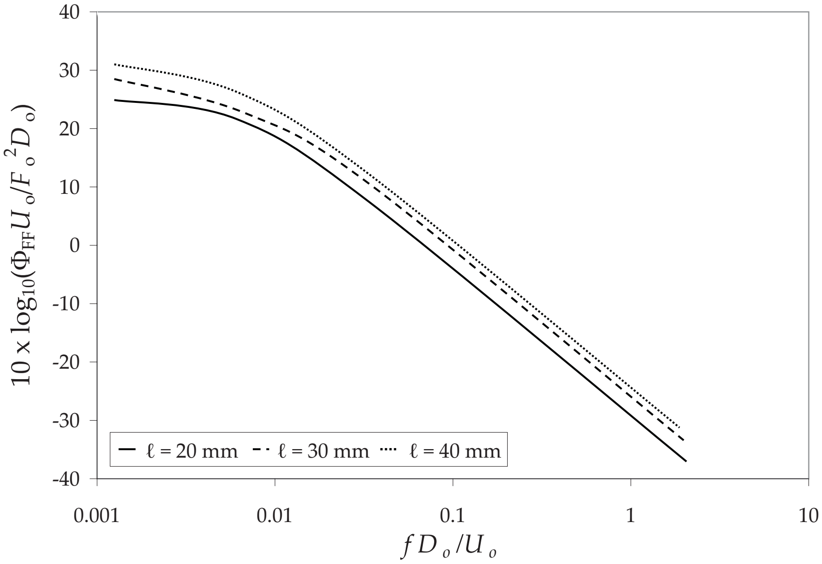

Figure E.10. Measured force spectra for jets of gas injection rate $Q = 0.0071$ m^3/s and jet lengths $\ell = 20$, 30, and 40 mm, run B, normalized to mean force F_o in 15.6 Hz bins, versus dimensionless frequency fD_o/U_o.

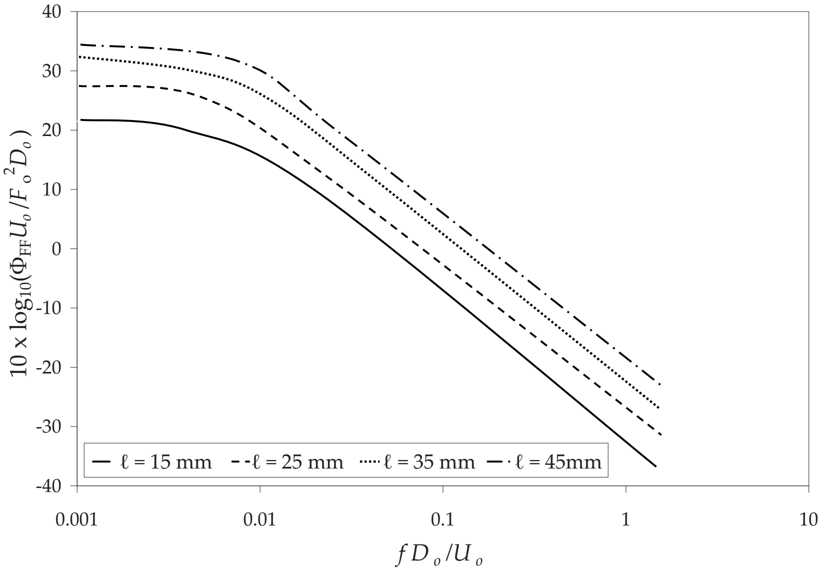

Figure E.11. Measured force spectra for jets of gas injection rate $Q = 0.0094$ m^3/s and jet lengths $\ell = 15$, 25, 35, and 45 mm, run B, normalized to mean force F_o in 15.6 Hz bins, versus dimensionless frequency fD_o/U_o.

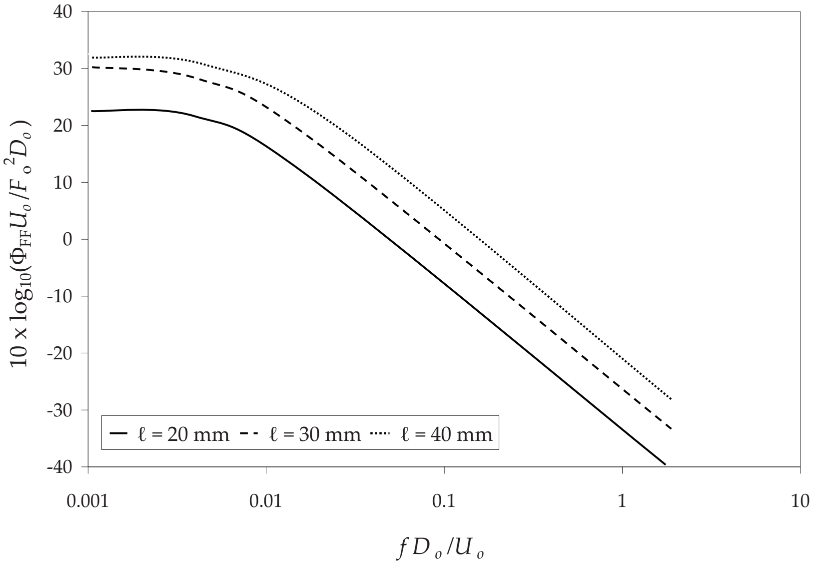

Figure E.12. Measured force spectra for jets of gas injection rate $Q = 0.0094$ m^3/s and jet lengths $\ell = 20$, 30, and 40 mm, run B, normalized to mean force F_o in 15.6 Hz bins, versus dimensionless frequency fD_o/U_o.

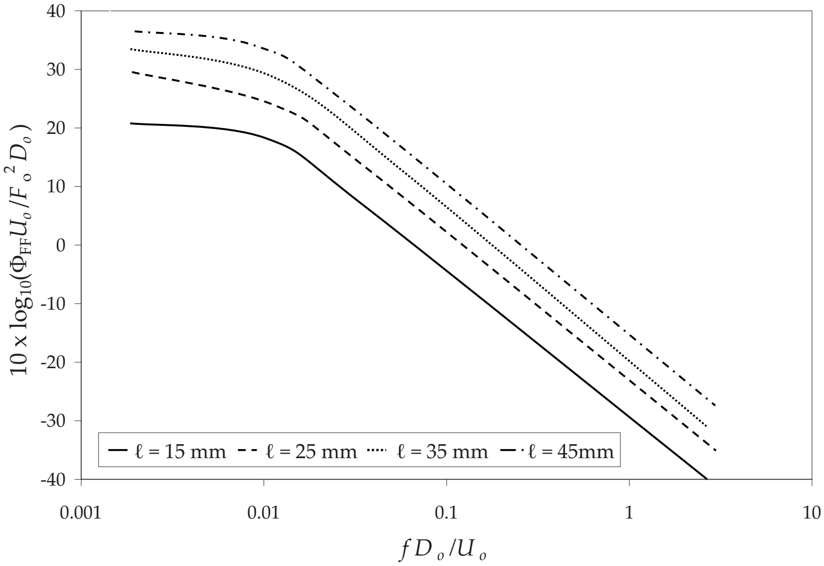

Figure E.13. Measured force spectra for jets of gas injection rate $Q = 0.0047$ m^3/s and jet lengths $\ell = 15$, 25, 35, and 45 mm, run C, normalized to mean force F_o in 15.6 Hz bins, versus dimensionless frequency fD_o/U_o.

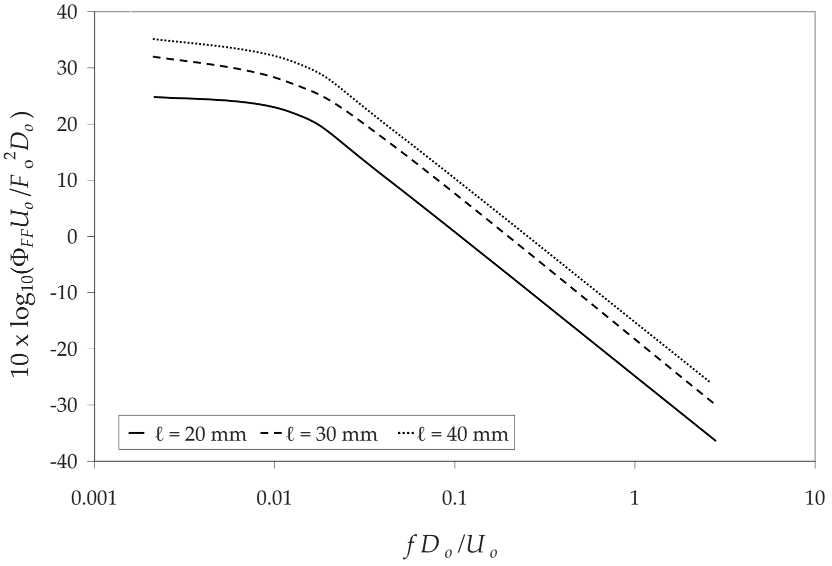

Figure E.14. Measured force spectra for jets of gas injection rate $Q = 0.0047$ m^3/s and jet lengths $\ell = 20$, 30, and 40 mm, run C, normalized to mean force F_o in 15.6 Hz bins, versus dimensionless frequency fD_o/U_o.

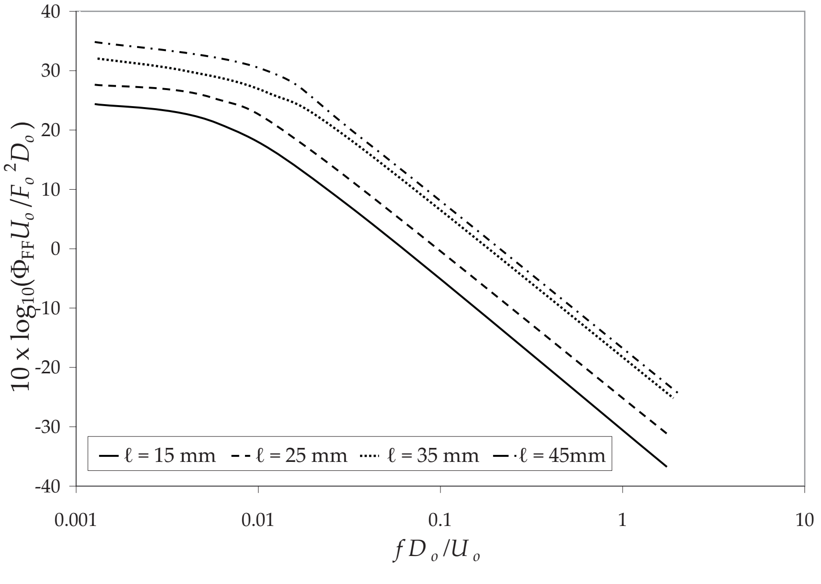

Figure E.15. Measured force spectra for jets of gas injection rate $Q = 0.0071$ m^3/s and jet lengths $\ell = 15$, 25, 35, and 45 mm, run C, normalized to mean force F_o in 15.6 Hz bins, versus dimensionless frequency fD_o/U_o.

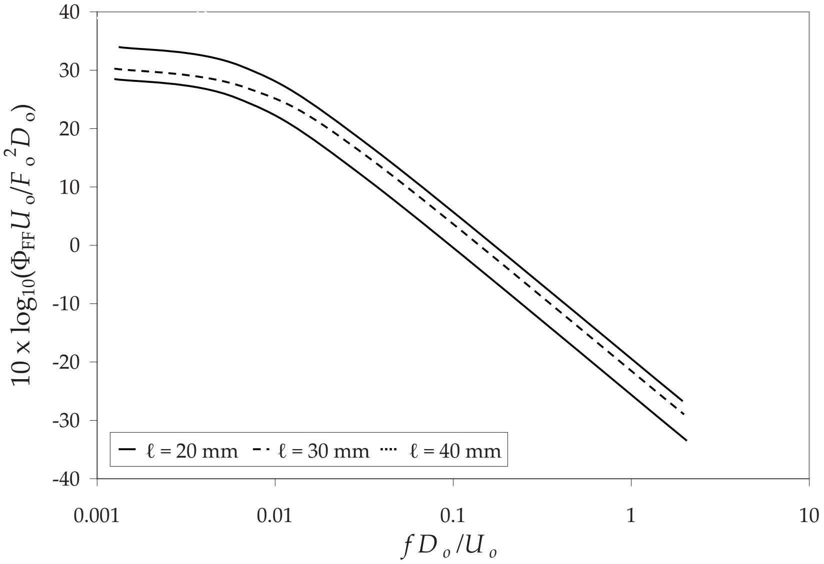

Figure E.16. Measured force spectra for jets of gas injection rate $Q = 0.0071$ m^3/s and jet lengths $\ell = 20$, 30, and 40 mm, run C, normalized to mean force F_o in 15.6 Hz bins, versus dimensionless frequency fD_o/U_o.

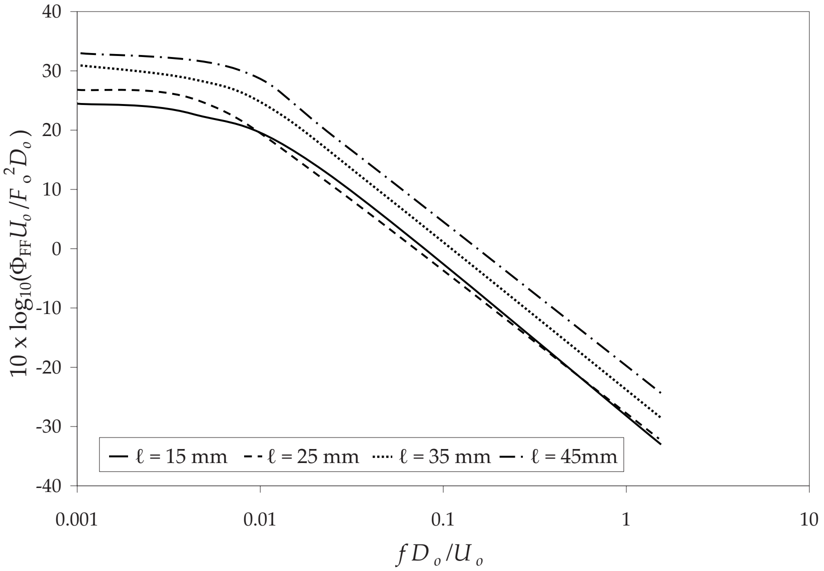

Figure E.17. Measured force spectra for jets of gas injection rate $Q = 0.0094$ m^3/s and jet lengths $\ell = 15$, 25, 35, and 45 mm, run C, normalized to mean force F_o in 15.6 Hz bins, versus dimensionless frequency fD_o/U_o.

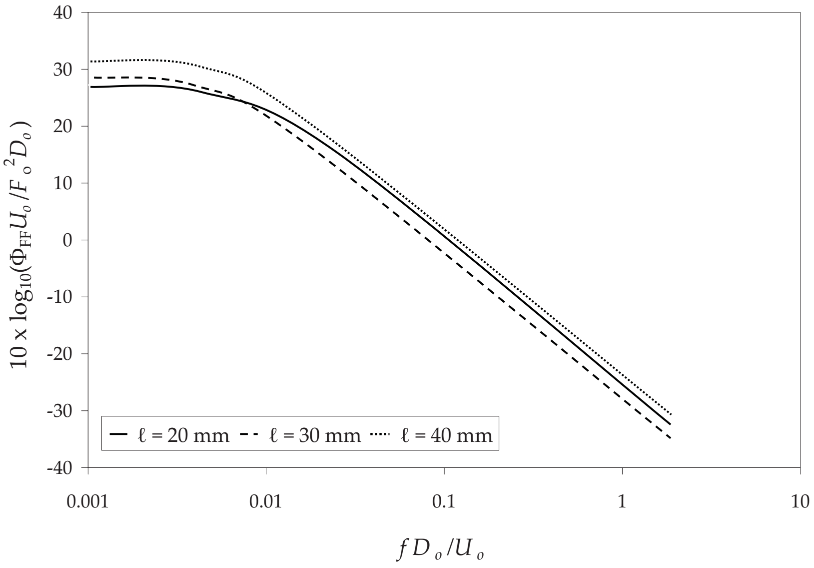

Figure E.18. Measured force spectra for jets of gas injection rate $Q = 0.0094$ m^3/s and jet lengths $\ell = 20$, 30, and 40 mm, run C, normalized to mean force F_o in 15.6 Hz bins, versus dimensionless frequency fD_o/U_o.

E.2 Predicted sound power spectra (§4.5)

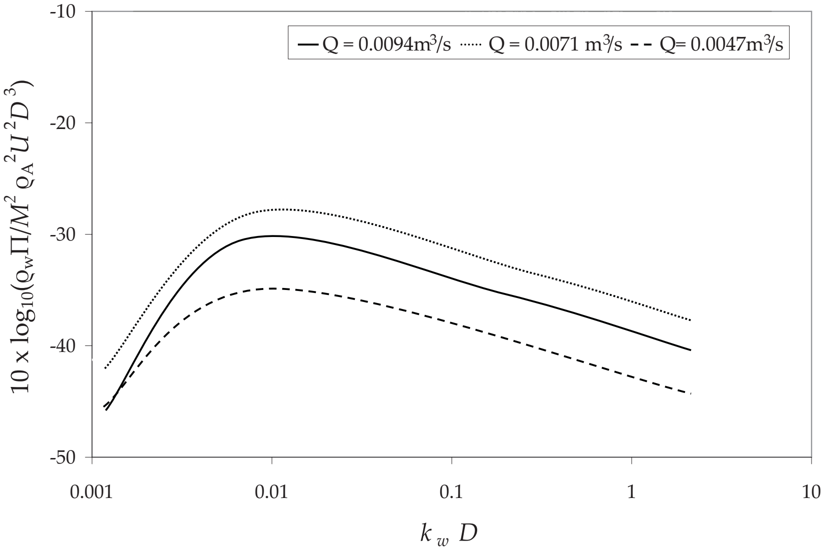

Figure E.19. Predicted sound power spectra for jets of gas injection rate $Q = 0.0047$, 0.0071, and 0.0094 m^3/s and $\ell = 15\,\mathrm{mm}$, run A, versus reduced frequency k_w/D.

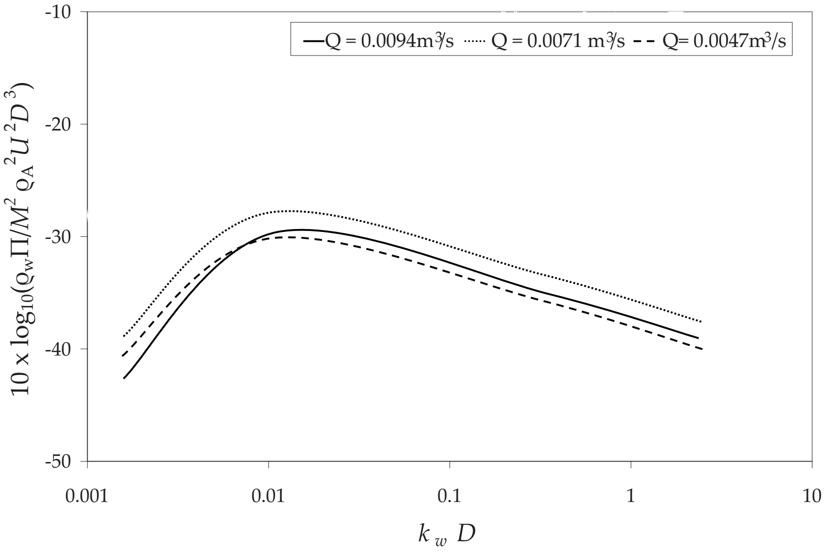

Figure E.20. Predicted sound power spectra for jets of gas injection rate $Q = 0.0047$, 0.0071, and 0.0094 m^3/s and $\ell = 20\,\mathrm{mm}$, run A, versus reduced frequency k_w/D.

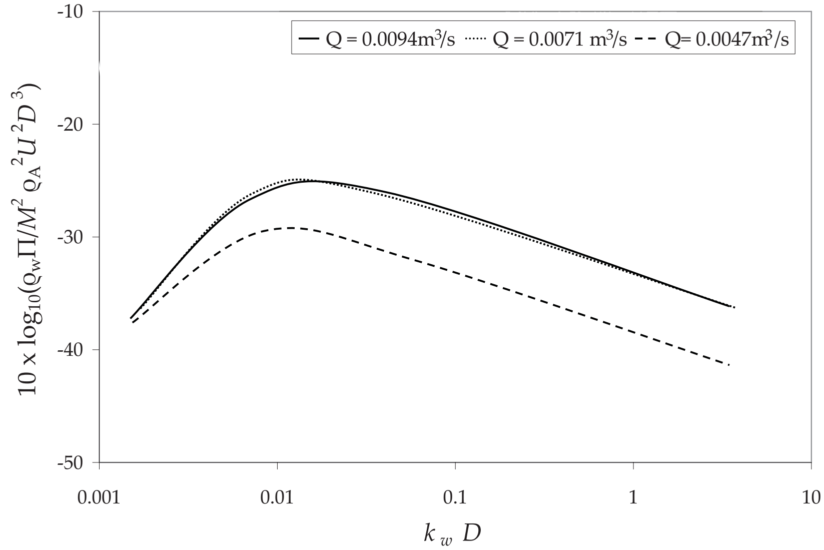

Figure E.21. Predicted sound power spectra for jets of gas injection rate $Q = 0.0047$, 0.0071, and 0.0094 m^3/s and $\ell = 25\,\mathrm{mm}$, run A, versus reduced frequency k_w/D.

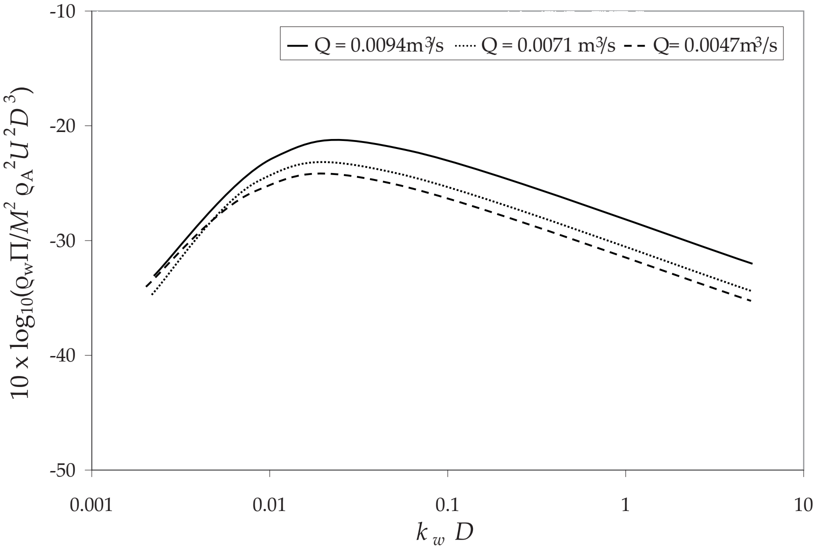

Figure E.22. Predicted sound power spectra for jets of gas injection rate $Q = 0.0047$, 0.0071, and 0.0094 m^3/s and $\ell = 30\,\mathrm{mm}$, run A, versus reduced frequency k_w/D.

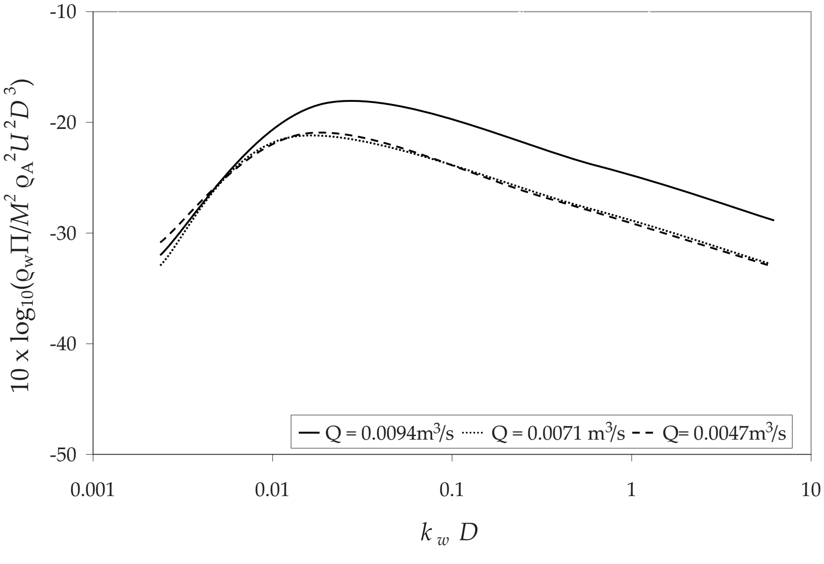

Figure E.23. Predicted sound power spectra for jets of gas injection rate $Q = 0.0047$, 0.0071, and 0.0094 m^3/s and $\ell = 35\,\mathrm{mm}$, run A, versus reduced frequency k_w/D.

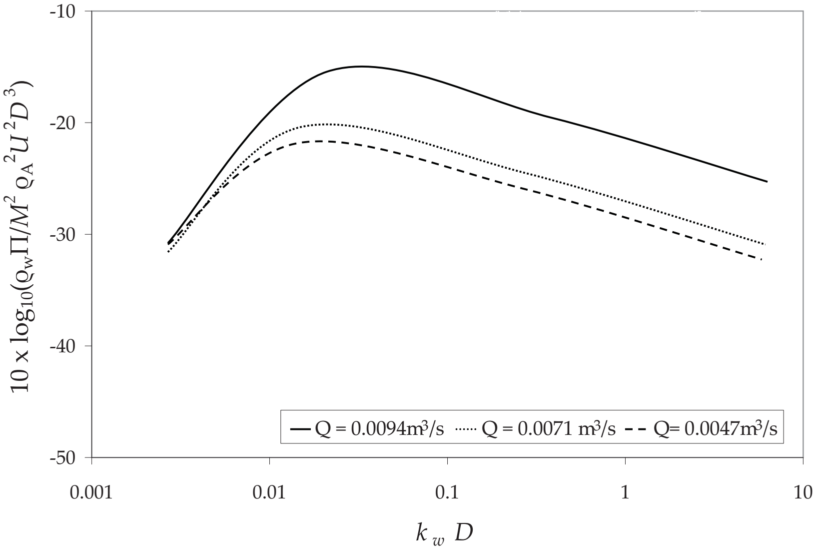

Figure E.24. Predicted sound power spectra for jets of gas injection rate $Q = 0.0047$, 0.0071, and 0.0094 m^3/s and $\ell = 40$ mm, run A, versus reduced frequency k_w/D.

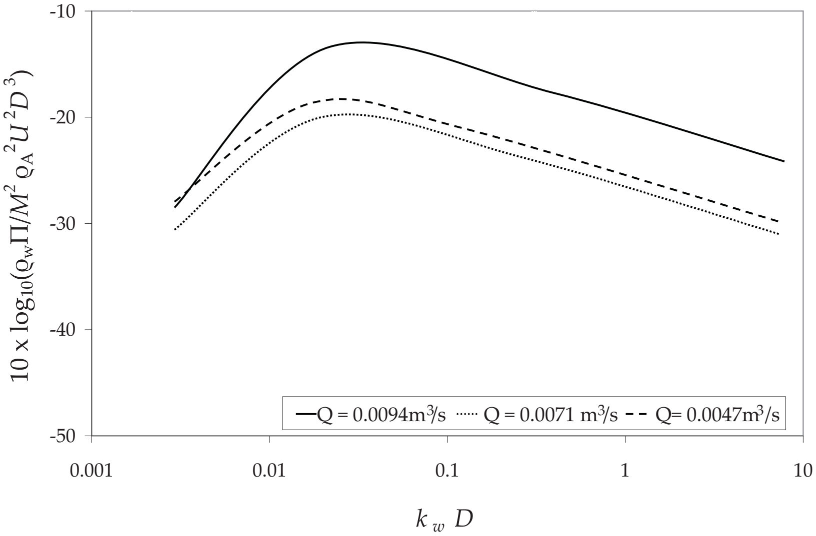

Figure E.25. Predicted sound power spectra for jets of gas injection rate $Q = 0.0047$, 0.0071, and 0.0094 m^3/s and $\ell = 45$ mm, run A, versus reduced frequency k_w/D.

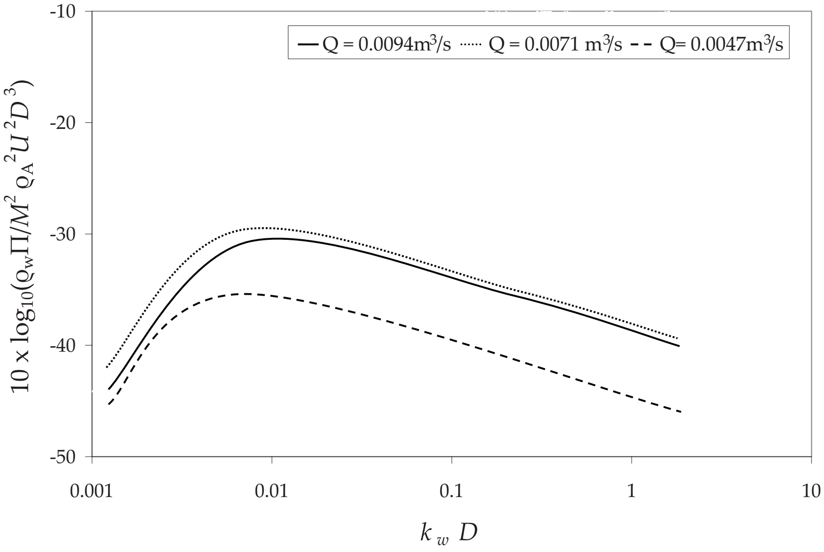

Figure E.26. Predicted sound power spectra for jets of gas injection rate $Q = 0.0047$, 0.0071, and 0.0094 m^3/s and $\ell = 15\,\mathrm{mm}$, run B, versus reduced frequency k_w/D.

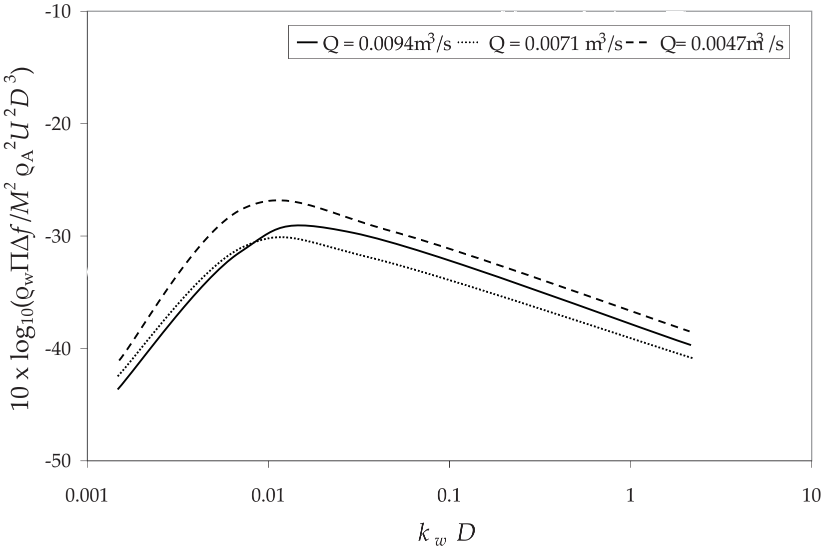

Figure E.27. Predicted sound power spectra for jets of gas injection rate $Q = 0.0047$, 0.0071, and 0.0094 m^3/s and $\ell = 20\,\mathrm{mm}$, run B, versus reduced frequency k_w/D.

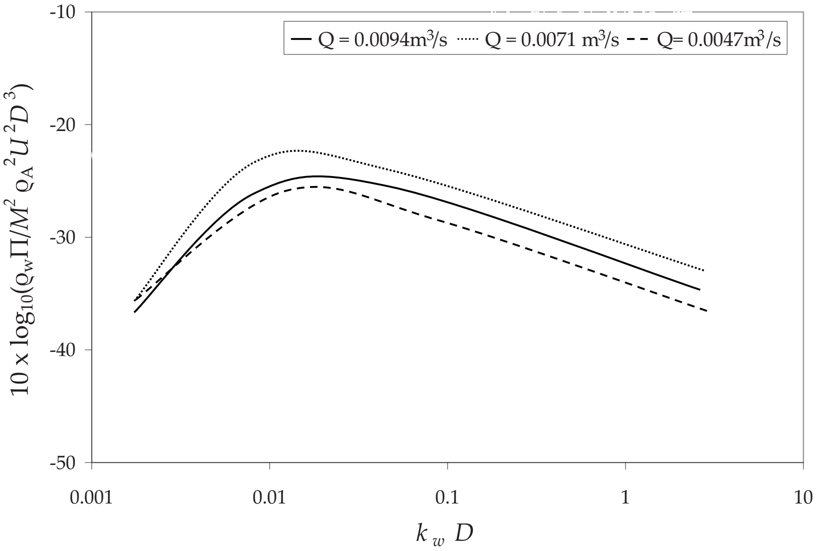

Figure E.28. Predicted sound power spectra for jets of gas injection rate $Q = 0.0047$, 0.0071, and 0.0094 m^3/s and $\ell = 25\,\mathrm{mm}$, run B, versus reduced frequency k_w/D.

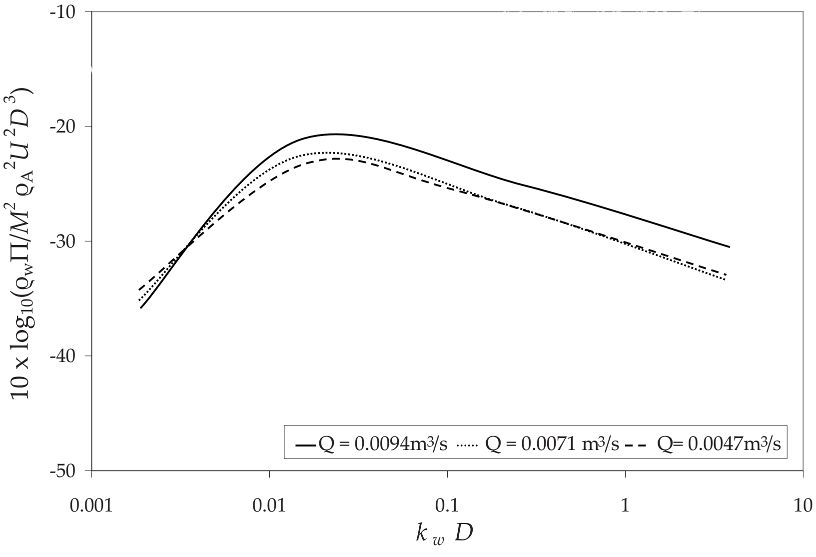

Figure E.29. Predicted sound power spectra for jets of gas injection rate $Q = 0.0047$, 0.0071, and 0.0094 m^3/s and $\ell = 30\,\mathrm{mm}$, run B, versus reduced frequency k_w/D.

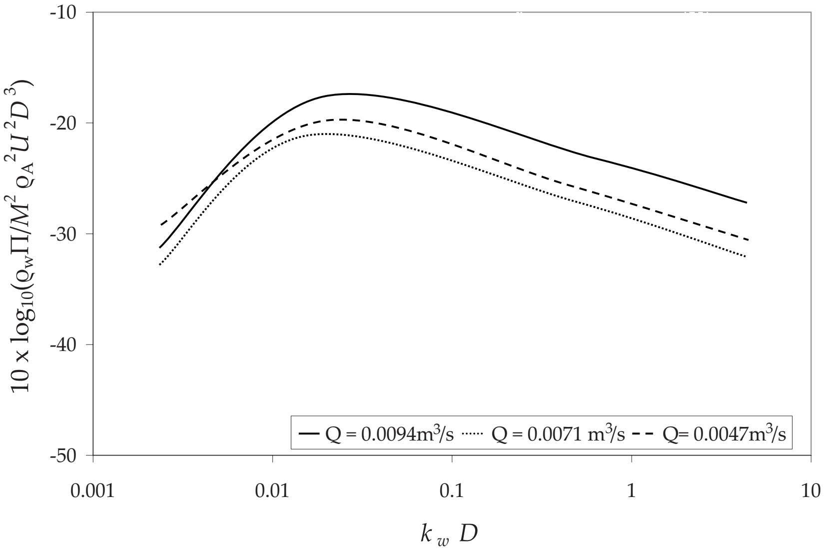

Figure E.30. Predicted sound power spectra for jets of gas injection rate $Q = 0.0047$, 0.0071, and 0.0094 m^3/s and $\ell = 35\,\mathrm{mm}$, run B, versus reduced frequency k_w/D.

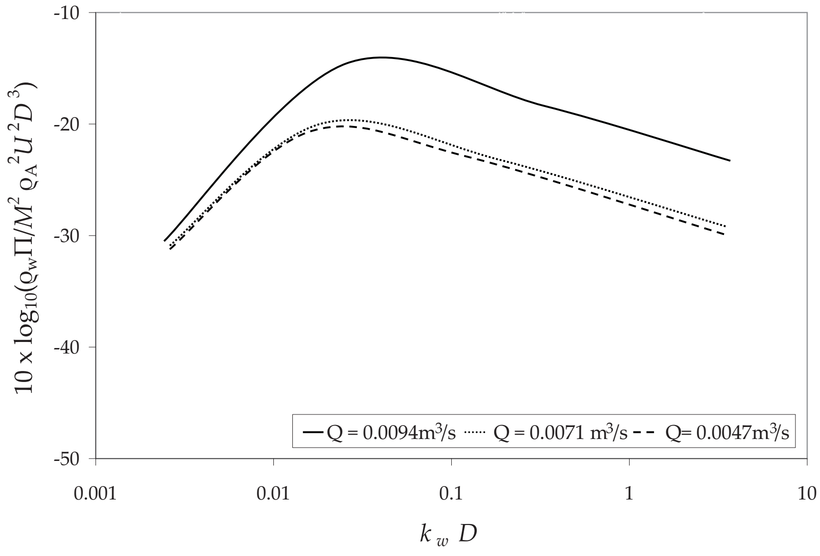

Figure E.31. Predicted sound power spectra for jets of gas injection rate $Q = 0.0047$, 0.0071, and 0.0094 m^3/s and $\ell = 40\,\mathrm{mm}$, run B, versus reduced frequency k_w/D.

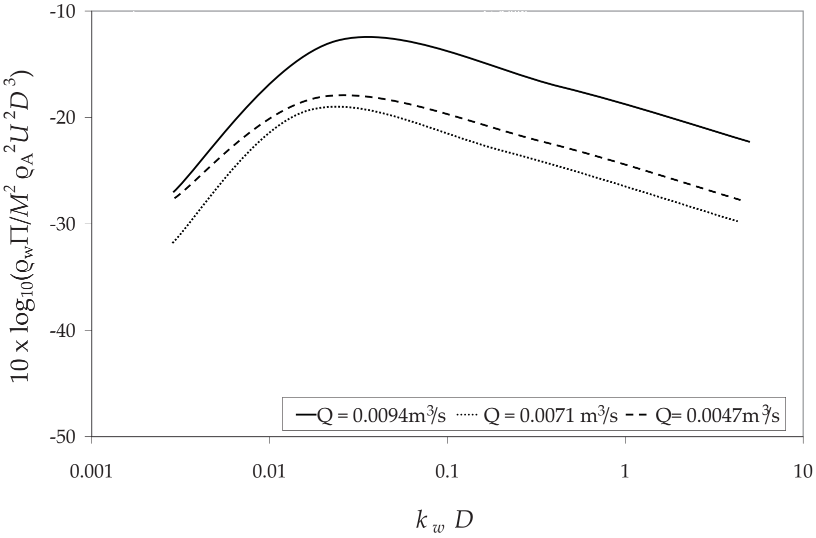

Figure E.32. Predicted sound power spectra for jets of gas injection rate $Q = 0.0047$, 0.0071, and 0.0094 m^3/s and $\ell = 45\,\mathrm{mm}$, run B, versus reduced frequency k_w/D.

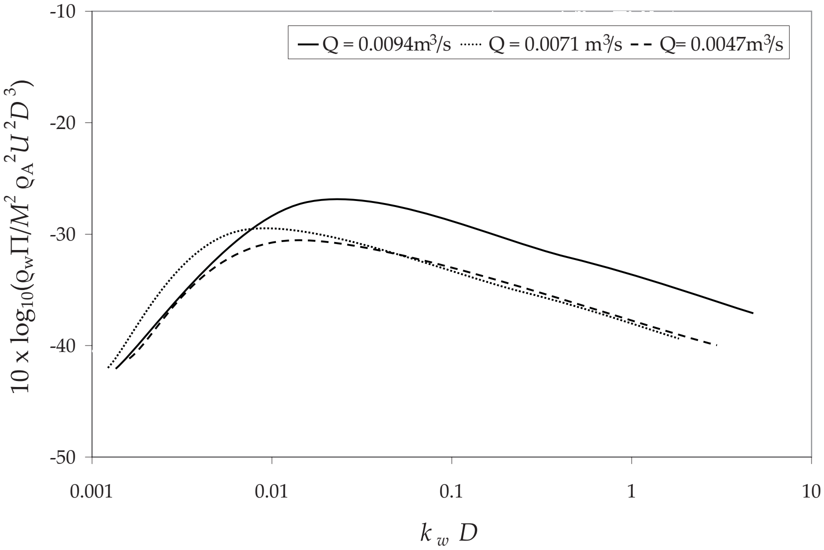

Figure E.33. Predicted sound power spectra for jets of gas injection rate $Q = 0.0047$, 0.0071, and 0.0094 m^3/s and $\ell = 15\,\mathrm{mm}$, run C, versus reduced frequency k_w/D.

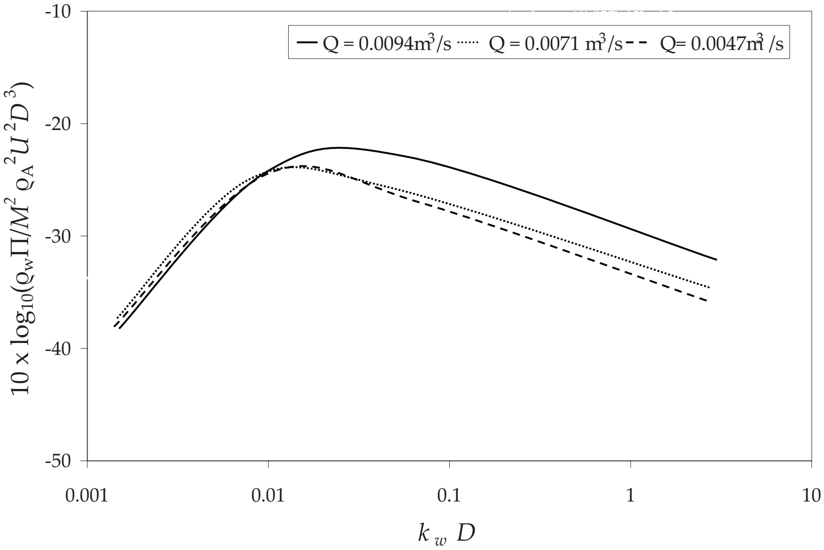

Figure E.34. Predicted sound power spectra for jets of gas injection rate $Q = 0.0047$, 0.0071, and 0.0094 m^3/s and $\ell = 20\,\text{mm}$, run C, versus reduced frequency k_w/D.

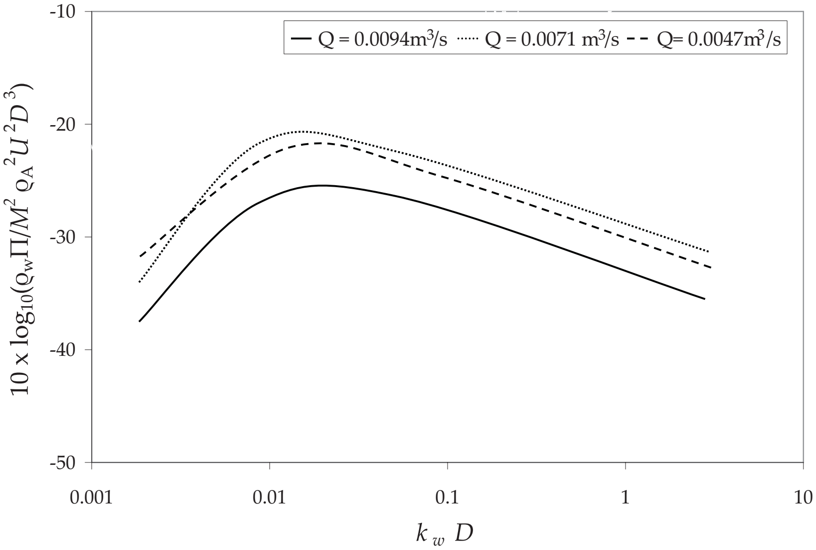

Figure E.35. Predicted sound power spectra for jets of gas injection rate $Q = 0.0047$, 0.0071, and 0.0094 m^3/s and $\ell = 25\,\text{mm}$, run C, versus reduced frequency k_w/D.

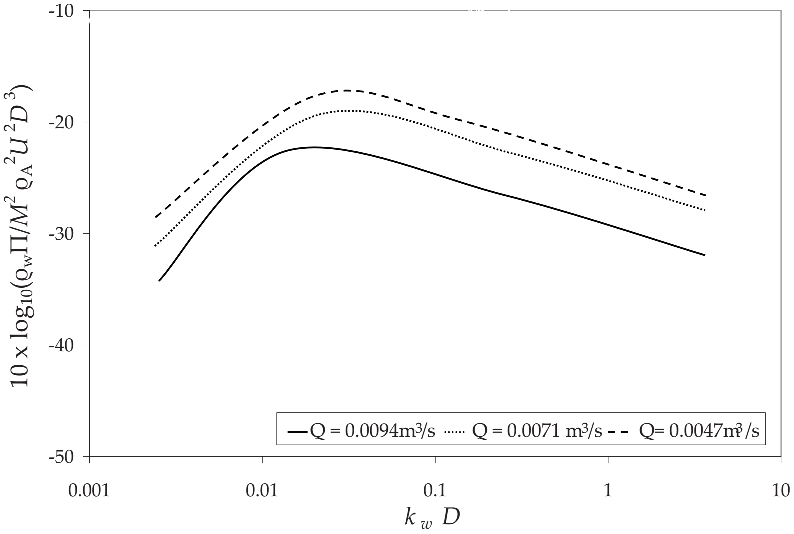

Figure E.36. Predicted sound power spectra for jets of gas injection rate $Q = 0.0047$, 0.0071, and 0.0094 m^3/s and $\ell = 30\,$mm, run C, versus reduced frequency k_w/D.

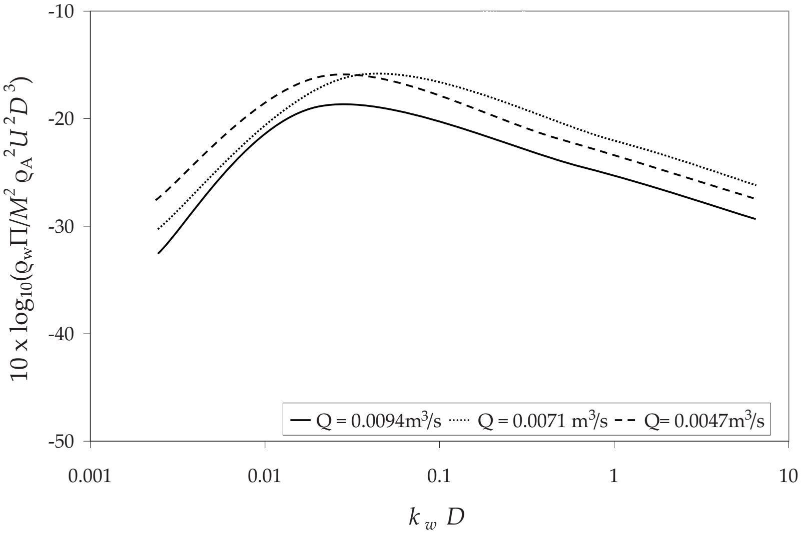

Figure E.37. Predicted sound power spectra for jets of gas injection rate $Q = 0.0047$, 0.0071, and 0.0094 m^3/s and $\ell = 35\,$mm, run C, versus reduced frequency k_w/D.

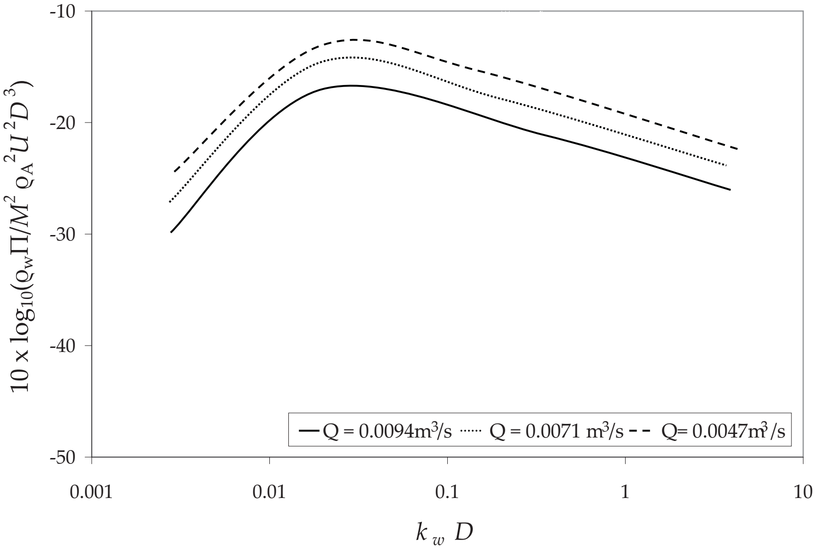

Figure E.38. Predicted sound power spectra for jets of gas injection rate $Q = 0.0047$, 0.0071, and 0.0094 m^3/s and $\ell = 40\,\mathrm{mm}$, run C, versus reduced frequency k_w/D.

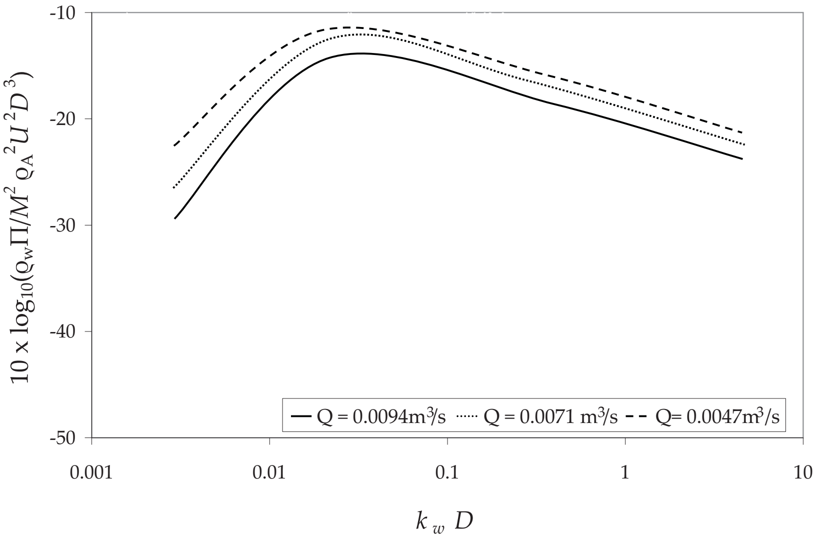

Figure E.39. Predicted sound power spectra for jets of gas injection rate $Q = 0.0047$, 0.0071, and 0.0094 m^3/s and $\ell = 45\,\mathrm{mm}$, run C, versus reduced frequency k_w/D.

E.3 Predicted self-noise spectra at the vehicle nose (§5.5)

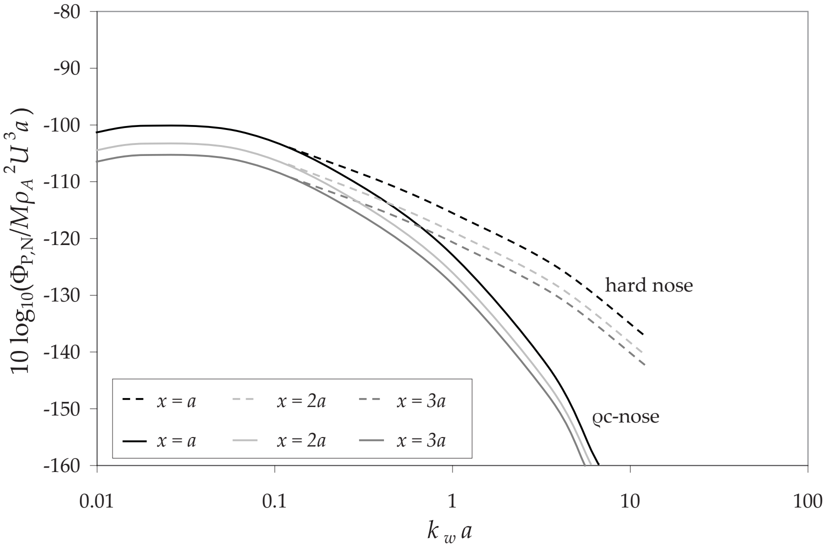

Figure E.40. Predictions of the sound pressure at the nose when $x = a, 2a, 3a$ for an ellipsoidal cavitator of aspect ratio $b/a = 5/3$ for cases where the cavitator has a ρc-nose or is acoustically hard and gas is injected at $Q = 0.0047\,\mathrm{m}^3/\mathrm{s}$ producing jets of length 15 mm.

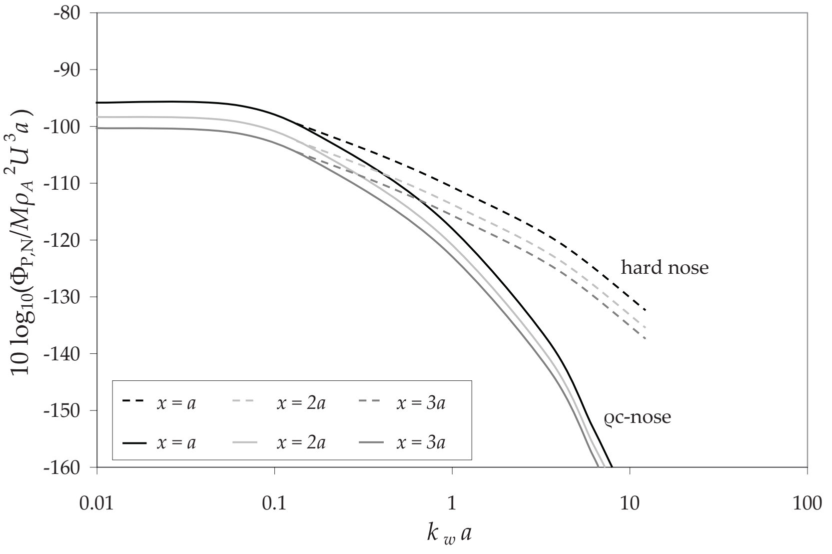

Figure E.41. Predictions of the sound pressure at the nose when $x = a, 2a, 3a$ for an ellipsoidal cavitator of aspect ratio $b/a = 5/3$ for cases where the cavitator has a ρc-nose or is acoustically hard and gas is injected at $Q = 0.0047\,\mathrm{m}^3/\mathrm{s}$ producing jets of length 20 mm.

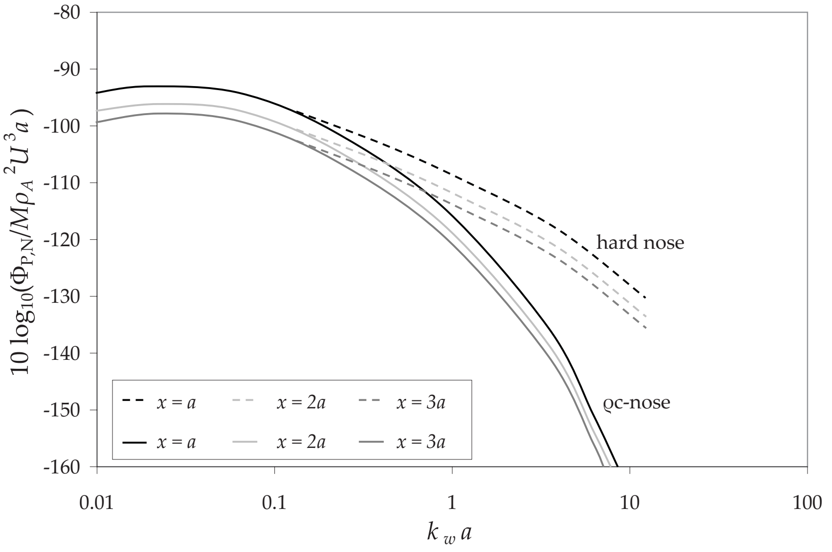

Figure E.42. Predictions of the sound pressure at the nose when $x = a, 2a, 3a$ for an ellipsoidal cavitator of aspect ratio $b/a = 5/3$ for cases where the cavitator has a ρc-nose or is acoustically hard and gas is injected at $Q = 0.0047\,\mathrm{m}^3/\mathrm{s}$ producing jets of length 25 mm.

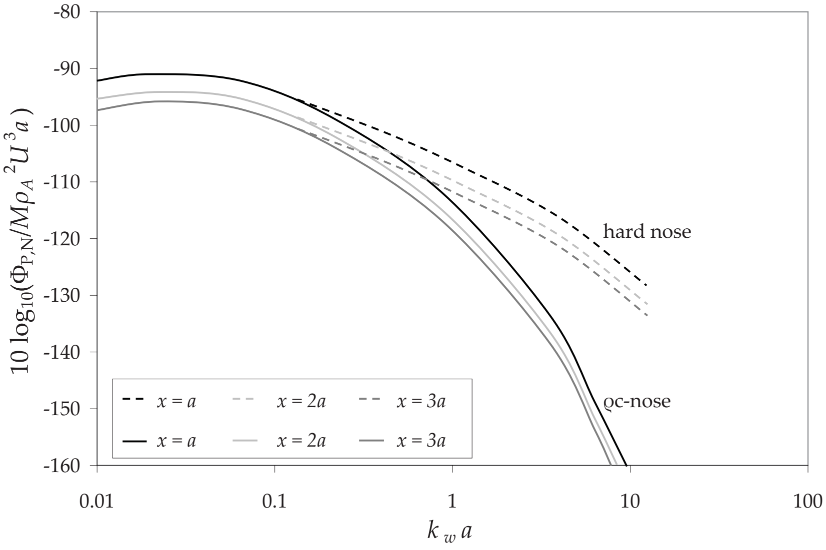

Figure E.43. Predictions of the sound pressure at the nose when $x = a, 2a, 3a$ for an ellipsoidal cavitator of aspect ratio $b/a = 5/3$ for cases where the cavitator has a ρc-nose or is acoustically hard and gas is injected at $Q = 0.0047\,\mathrm{m}^3/\mathrm{s}$ producing jets of length 30 mm.

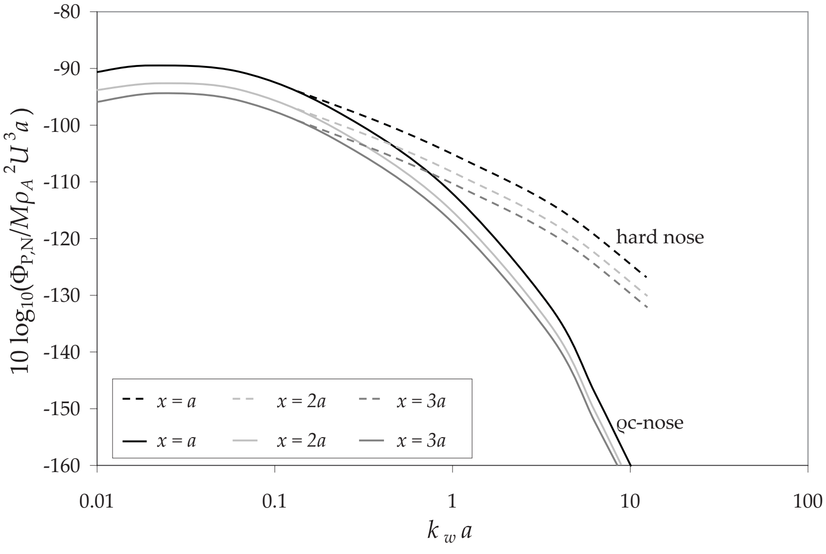

Figure E.44. Predictions of the sound pressure at the nose when $x = a, 2a, 3a$ for an ellipsoidal cavitator of aspect ratio $b/a = 5/3$ for cases where the cavitator has a ρc-nose or is acoustically hard and gas is injected at $Q = 0.0047\,\mathrm{m}^3/\mathrm{s}$ producing jets of length 35 mm.

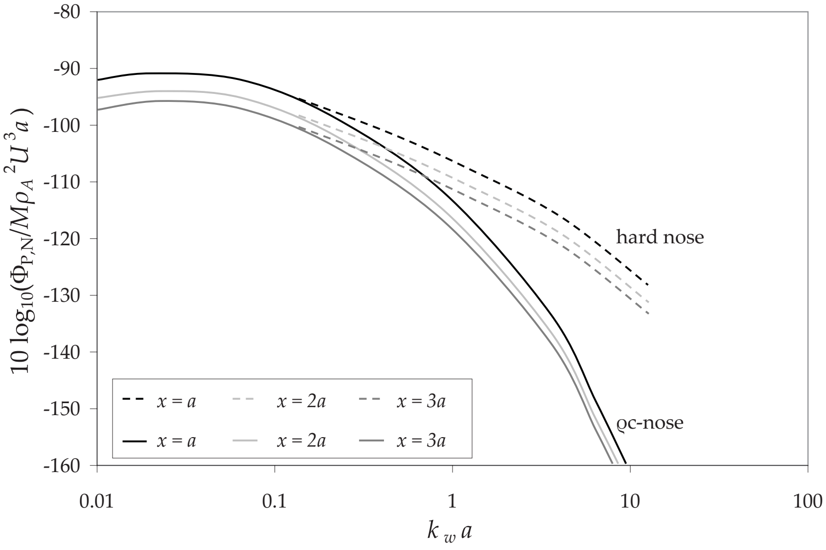

Figure E.45. Predictions of the sound pressure at the nose when $x = a, 2a, 3a$ for an ellipsoidal cavitator of aspect ratio $b/a = 5/3$ for cases where the cavitator has a ρc-nose or is acoustically hard and gas is injected at $Q = 0.0047\,\mathrm{m}^3/\mathrm{s}$ producing jets of length 40 mm.

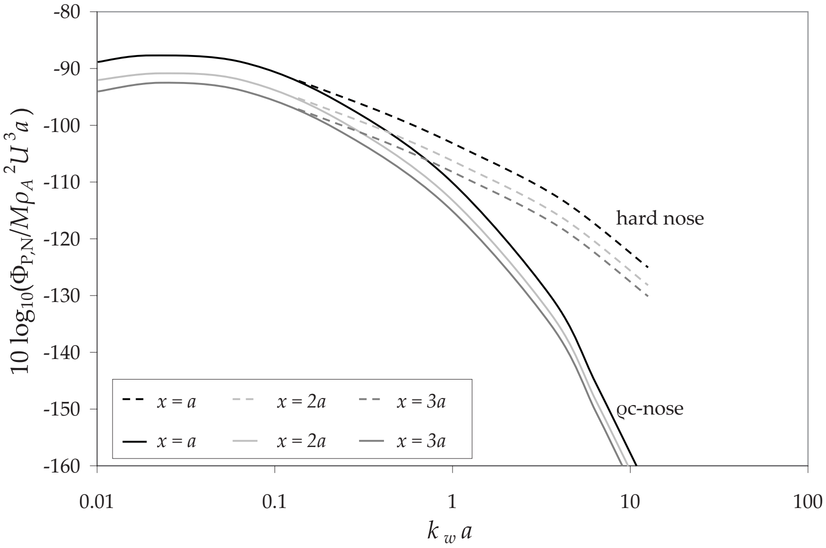

Figure E.46. Predictions of the sound pressure at the nose when $x = a, 2a, 3a$ for an ellipsoidal cavitator of aspect ratio $b/a = 5/3$ for cases where the cavitator has a ρc-nose or is acoustically hard and gas is injected at $Q = 0.0047\,\mathrm{m}^3/\mathrm{s}$ producing jets of length 45 mm.

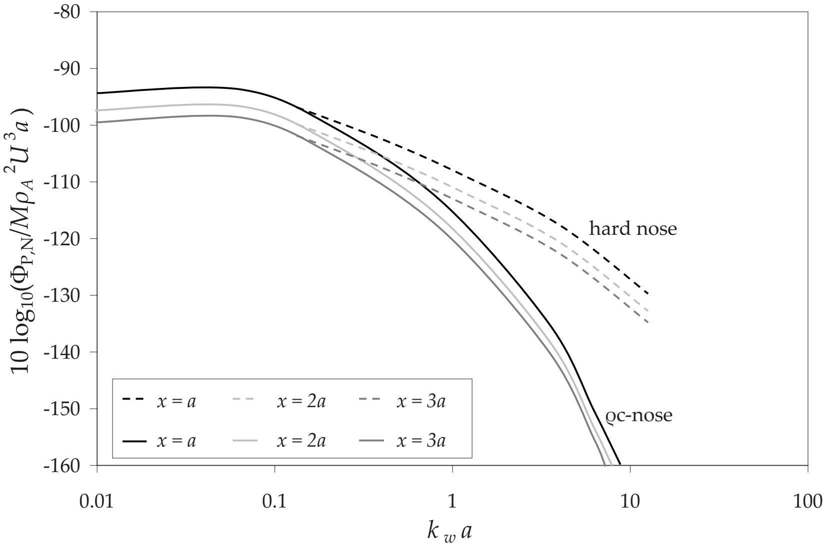

Figure E.47. Predictions of the sound pressure at the nose when $x = a, 2a, 3a$ for an ellipsoidal cavitator of aspect ratio $b/a = 5/3$ for cases where the cavitator has a ρc-nose or is acoustically hard and gas is injected at $Q = 0.0071\,\mathrm{m}^3/\mathrm{s}$ producing jets of length 15 mm.

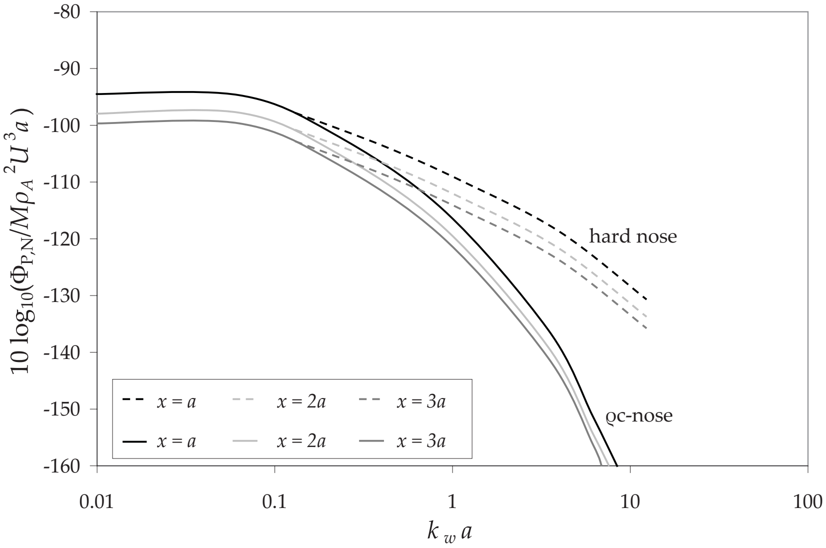

Figure E.48. Predictions of the sound pressure at the nose when $x = a, 2a, 3a$ for an ellipsoidal cavitator of aspect ratio $b/a = 5/3$ for cases where the cavitator has a ρc-nose or is acoustically hard and gas is injected at $Q = 0.0071\,\mathrm{m}^3/\mathrm{s}$ producing jets of length 20 mm.

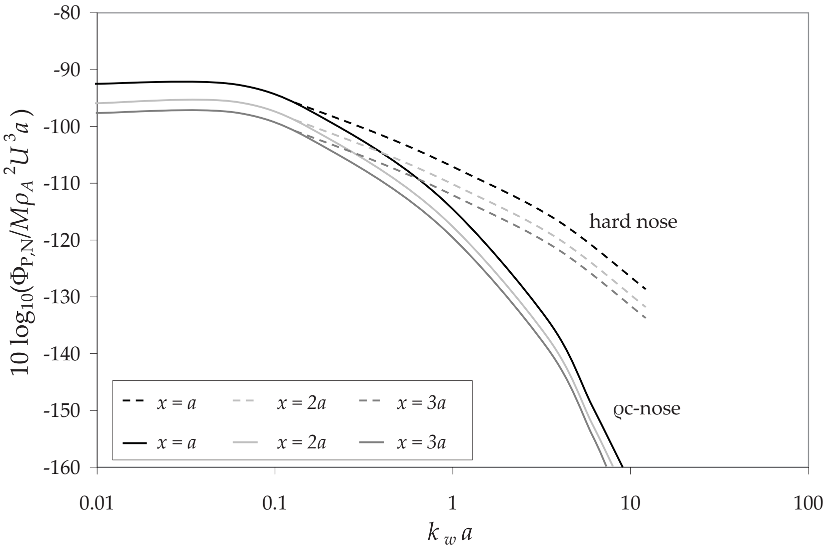

Figure E.49. Predictions of the sound pressure at the nose when $x = a, 2a, 3a$ for an ellipsoidal cavitator of aspect ratio $b/a = 5/3$ for cases where the cavitator has a ρc-nose or is acoustically hard and gas is injected at $Q = 0.0071\,\mathrm{m}^3/\mathrm{s}$ producing jets of length $25\,\mathrm{mm}$.

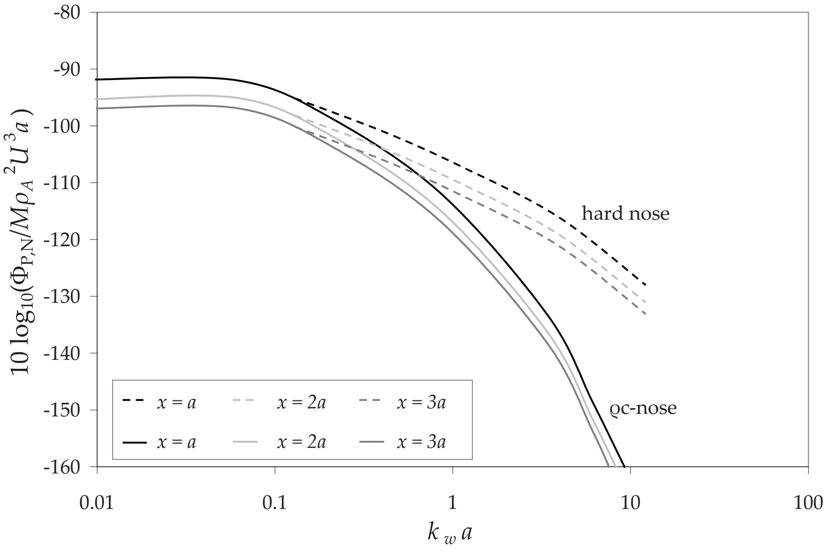

Figure E.50. Predictions of the sound pressure at the nose when $x = a, 2a, 3a$ for an ellipsoidal cavitator of aspect ratio $b/a = 5/3$ for cases where the cavitator has a ρc-nose or is acoustically hard and gas is injected at $Q = 0.0071\,\mathrm{m}^3/\mathrm{s}$ producing jets of length $30\,\mathrm{mm}$.

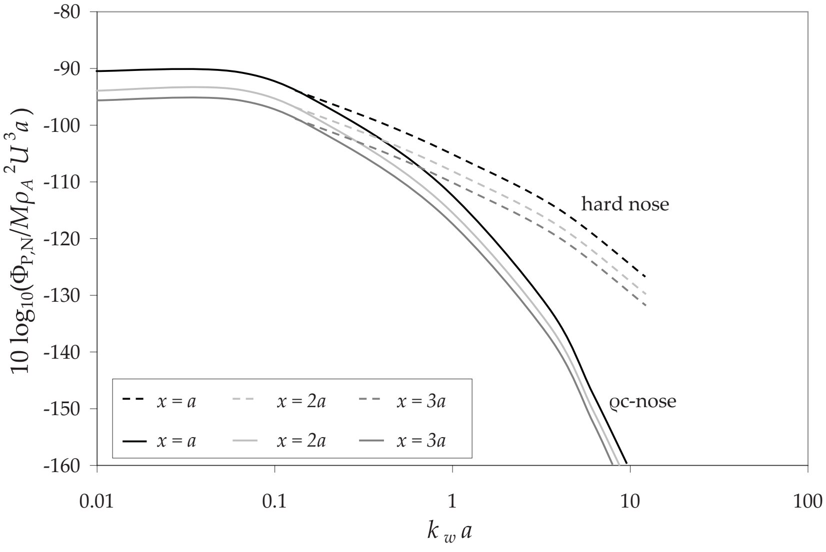

Figure E.51. Predictions of the sound pressure at the nose when $x = a, 2a, 3a$ for an ellipsoidal cavitator of aspect ratio $b/a = 5/3$ for cases where the cavitator has a ρc-nose or is acoustically hard and gas is injected at $Q = 0.0071\,\mathrm{m}^3/\mathrm{s}$ producing jets of length $35\,\mathrm{mm}$.

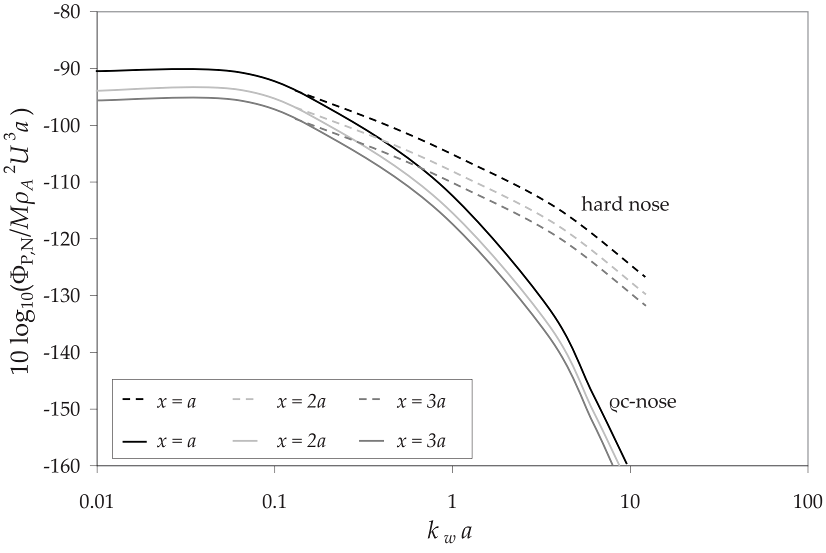

Figure E.52. Predictions of the sound pressure at the nose when $x = a, 2a, 3a$ for an ellipsoidal cavitator of aspect ratio $b/a = 5/3$ for cases where the cavitator has a ρc-nose or is acoustically hard and gas is injected at $Q = 0.0071\,\mathrm{m}^3/\mathrm{s}$ producing jets of length $40\,\mathrm{mm}$.

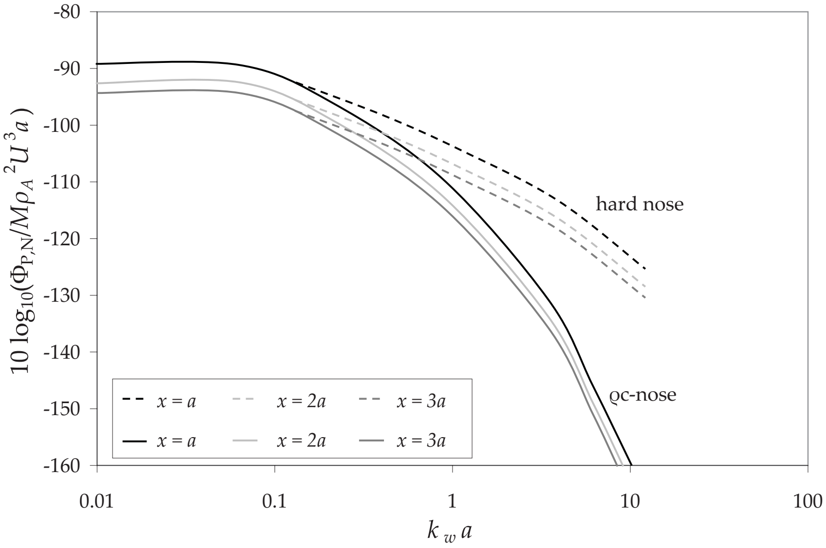

Figure E.53. Predictions of the sound pressure at the nose when $x = a, 2a, 3a$ for an ellipsoidal cavitator of aspect ratio $b/a = 5/3$ for cases where the cavitator has a ρc-nose or is acoustically hard and gas is injected at $Q = 0.0071\,\mathrm{m}^3/\mathrm{s}$ producing jets of length 45 mm.

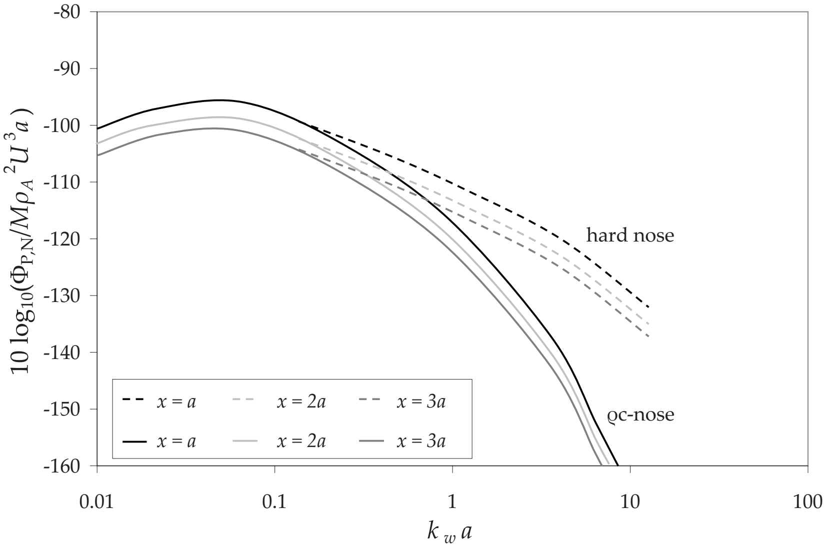

Figure E.54. Predictions of the sound pressure at the nose when $x = a, 2a, 3a$ for an ellipsoidal cavitator of aspect ratio $b/a = 5/3$ for cases where the cavitator has a ρc-nose or is acoustically hard and gas is injected at $Q = 0.0094\,\mathrm{m}^3/\mathrm{s}$ producing jets of length 15 mm.

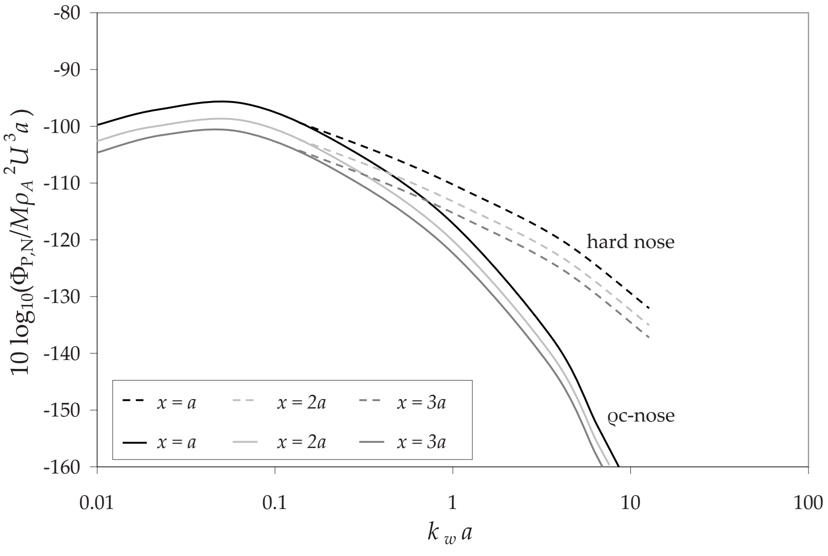

Figure E.55. Predictions of the sound pressure at the nose when $x = a, 2a, 3a$ for an ellipsoidal cavitator of aspect ratio $b/a = 5/3$ for cases where the cavitator has a ρc-nose or is acoustically hard and gas is injected at $Q = 0.0094\,\mathrm{m}^3/\mathrm{s}$ producing jets of length 20 mm.

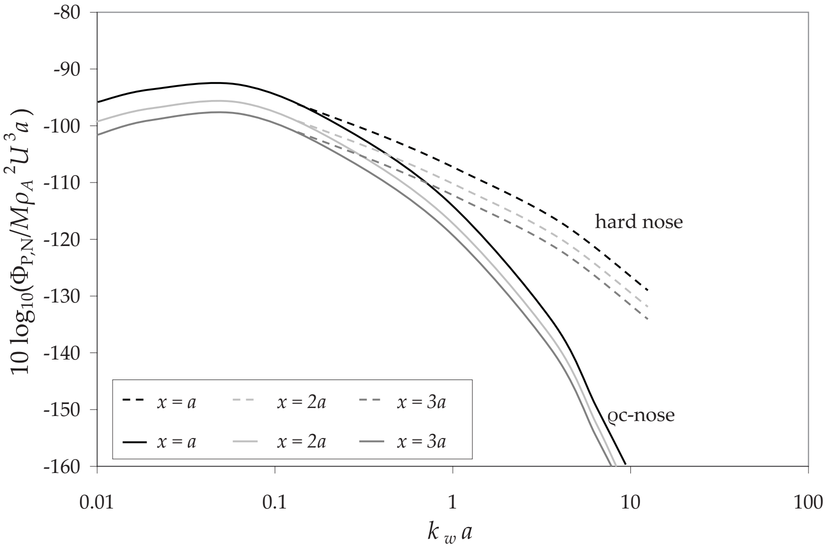

Figure E.56. Predictions of the sound pressure at the nose when $x = a, 2a, 3a$ for an ellipsoidal cavitator of aspect ratio $b/a = 5/3$ for cases where the cavitator has a ρc-nose or is acoustically hard and gas is injected at $Q = 0.0094\,\mathrm{m}^3/\mathrm{s}$ producing jets of length 25 mm.

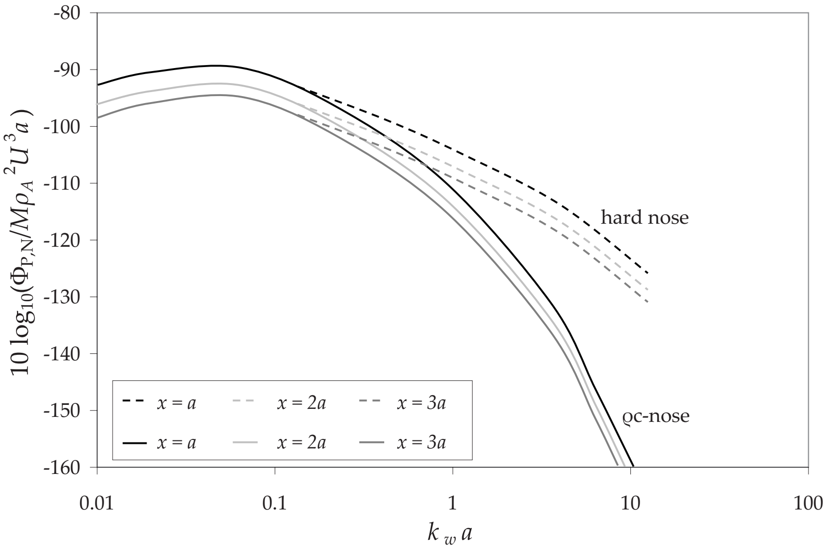

Figure E.57. Predictions of the sound pressure at the nose when $x = a, 2a, 3a$ for an ellipsoidal cavitator of aspect ratio $b/a = 5/3$ for cases where the cavitator has a ρc-nose or is acoustically hard and gas is injected at $Q = 0.0094\,\mathrm{m}^3/\mathrm{s}$ producing jets of length 30 mm.

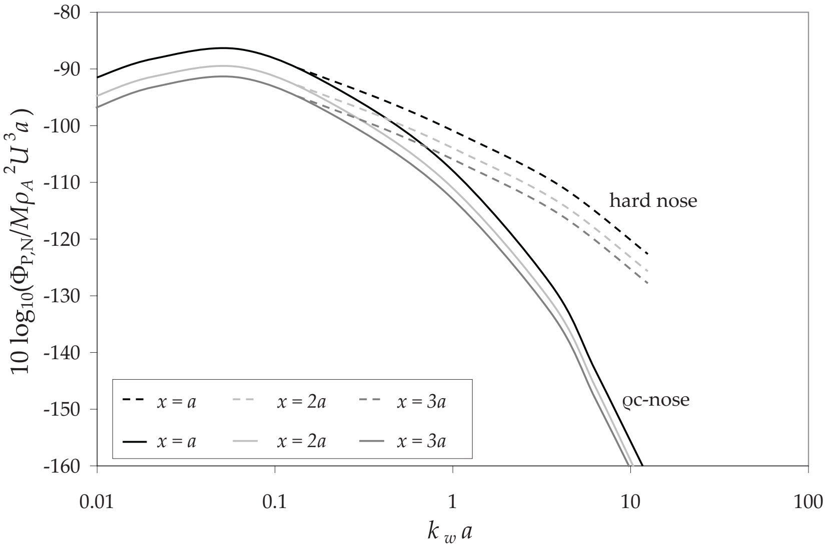

Figure E.58. Predictions of the sound pressure at the nose when $x = a, 2a, 3a$ for an ellipsoidal cavitator of aspect ratio $b/a = 5/3$ for cases where the cavitator has a ρc-nose or is acoustically hard and gas is injected at $Q = 0.0094\,\mathrm{m}^3/\mathrm{s}$ producing jets of length 35 mm.

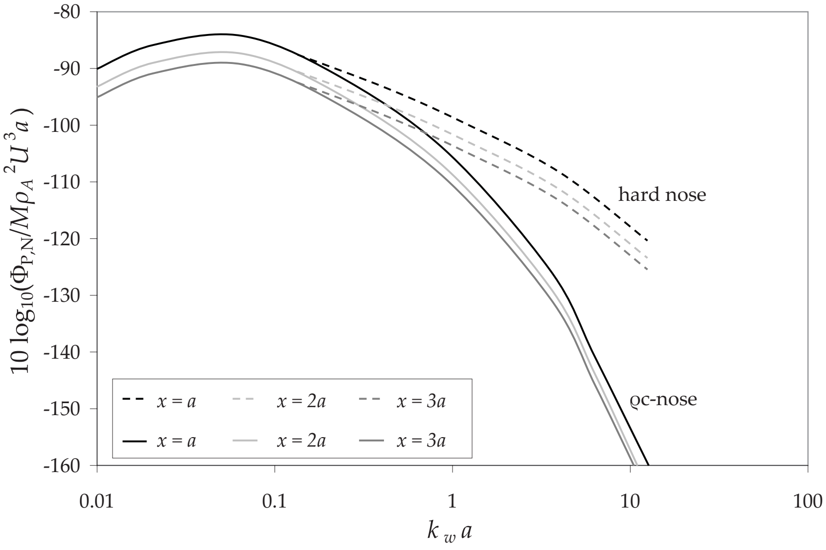

Figure E.59. Predictions of the sound pressure at the nose when $x = a, 2a, 3a$ for an ellipsoidal cavitator of aspect ratio $b/a = 5/3$ for cases where the cavitator has a ρc-nose or is acoustically hard and gas is injected at $Q = 0.0094\,\mathrm{m}^3/\mathrm{s}$ producing jets of length 40 mm.

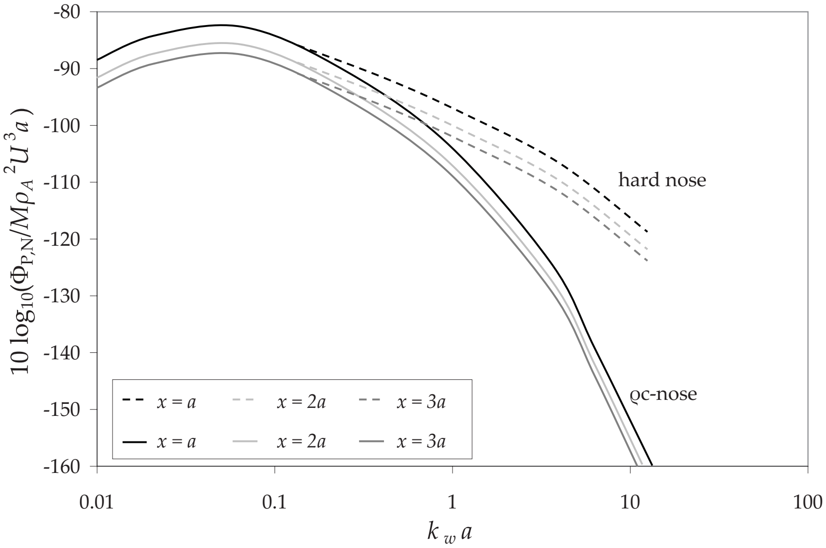

Figure E.60. Predictions of the sound pressure at the nose when $x = a, 2a, 3a$ for an ellipsoidal cavitator of aspect ratio $b/a = 5/3$ for cases where the cavitator has a ρc-nose or is acoustically hard and gas is injected at $Q = 0.0094\,\mathrm{m}^3/\mathrm{s}$ producing jets of length 45 mm.

Bibliography

[1] M. Abramowitz and I. A. Stegun. *Handbook of Mathematical Functions with Formulas, Graphs, and Mathematical Tables.* Dover, New York, 9th dover printing, 10th gpo printing edition, 1964.

[2] B. B. Baker and E. T. Copson. *The Mathematical Theory of Huygen's Principle.* Oxford University Press, second edition, 1969.

[3] J. A. Bendat and A. G. Piersol. *Engineering Applications of Correlation and Spectral Analysis.* John Wiley & Sons, Inc., New York, second edition, 1993.

[4] G. Birkhoff and E. H. Zarantonello. *Jets, Wakes, and Cavities.* Academic Press Inc., 1957.

[5] D. T. Blackstock. *Fundamentals of Physcial Acoustics.* John Wiley & Sons, Inc., 2000.

[6] W. K. Blake. *Mechanics of flow-induced sound vibration.* Academic Press, New York, 1986.

[7] C. E. Brennen. *Cavitation and bubble dynamics.* Oxford University Press, 1995.

[8] K. G. Budden. *The Wave-guide Mode Theory of Wave Propagation.* Logos Press, London, 1961.

[9] P. C. Clemmow. *The Plane Wave Spectrum Representation of Electromagnetic Fields.* Pergamon Press, London, 1966.

[10] D. G. Crighton, A. P. Dowling, J. E. F. Williams, M. Heckl, and F.G.Leppington. Modern Methods in Analytical Acoustics (Lecture notes), 1992.

[11] C. Devin. Survey of thermal, radiation, and viscous damping of pulsating air bubbles in water. *Journal of the Acoustical Society of America* **31** 1654–1667, 1959.

[12] J. E. Ffowcs-Williams. Sound production at the edge of a steady flow. *Journal of Fluid Mechanics* **66** 791–816, 1974.

[13] A. W. Foley, M. S. Howe, and T. A. Brungart. Sound generated by a jet-excited spherical cavity. *Journal of Sound and Vibration* **315** 88–99, 2008.

[14] J.-P. Franc and J.-M. Michel. *Fundamentals of Cavitation*. Kluwer Academic Publishers, Dordrecht, 2004.

[15] B. Friedman. Propagation in a non-homogeneous atmosphere. *Communications on Pure and Applied Mathematics* **4** 317–350, 1951.

[16] J. O. Hinze. *Turbulence*. McGraw-Hill, New York, second edition, 1975.

[17] C.-M. Ho and N. S. Nossier. Dynamics of an impinging jet. Part 1. The feedback phenomenon. *Journal of Fluid Mechanics* **105** 119–142, 1981.

[18] M. S. Howe. *Acoustics of Fluid-Structure Interactions*. Cambridge University Press, 1998.

[19] M. S. Howe. Surface pressure and sound produced by turbulent pressure-release edge flow, 1998. Applied Research Laboratory TM 98-148.

[20] M. S. Howe. *Theory of Vortex Sound*. Cambridge University Press, 2003.

[21] M. S. Howe. Sound producted by a vortex interacting with a cavitated wake. *Journal of Fluid Mechanics* **543** 333–347, 2005.

[22] M. S. Howe. *Hydrodynamics and Sound*. Cambridge University Press, 2007.

[23] M. S. Howe, A. M. Colgan, and T. A. Brungart. On self-noise at the nose of a supercavitating vehicle. *Journal of Sound and Vibration* , 2008. Doi:10.1016/j.jsv.2008.11.019.

[24] M. C. Junger and D. Feit. *Sound, Structures, and their Interactions*. Acoustical Society of America, New York, 1993.

[25] D. E. Kerr (Ed.). Propagation of short radio waves. Technical report, Radiation Laboratory Report 13 Massachusetts Institute of Technology, 1947.

[26] R. T. Knapp, J. W. Daily, and F. G. Hammitt. *Cavitation*. McGraw-Hill, Inc., 1970.

[27] R. Kuklinski, C. Henoch, and J. Castano. Experimental study of ventilated cavities on dynamic test model, 2001. In *Cav2001*:Fourth International Symposium on Cavitation, June 20-23, 2001, California Institute of Technology Pasadena, CA.

[28] C.-Y. Kuo and A. P. Dowling. Acoustics of a two-dimensional compact jet impinging normally onto a flat plate. *Journal of Fluid Mechanics* **414** 251–284, 2000.

[29] L. D. Landau and E. M. Lifshitz. *Fluid Mechanics*. Pergamon Press, Oxford, second edition, 1987.

[30] T. G. Leighton. *The Acoustic Bubble*. Academic Press, New York, 1994.

[31] B. R. Levy and J. B. Keller. Diffraction by a smooth object. *Communications on Pure and Applied Mathematics* **12** 159–209, 1959.

[32] M. J. Lighthill. On sound generated aerodynamically. Part I: General theory. *Proceedings of the Royal Society of London* **211** 564–587, 1952.

[33] B. Noble. *Methods Based on the Wiener-Hopf Technique*. Pergamon Press, London, 1958.

[34] W. A. Olsen, J. H. Miles, and R. G. Dorsch. Noise generated by the impingement of a jet upon a large flat board. Technical Report TN D-7075, NASA, 1972.

[35] C. L. Pekeris. Accuracy of the earth-flattening approximation in the theory of microwave propagation. *Physics Review* **70** 518–522, 1946.

[36] W. Peng and D. E. Parker. An ideal fluid jet impinging on an uneven wall. *Journal of Fluid Mechanics* **333** 231–255, 1997.

[37] A. D. Pierce. *Acoustics: An Introduction to Its Physical Principles and Applications*. McGraw-Hill, Inc., 1981.

[38] J. C. Schelleng, C. R. Burrows, and E. B. Ferrell. Ultra-short-wave propagation. *Proceedings of the Institute of Radio Engineers* **21** 427–463, 1933.

[39] R. S. Scorer. *Natural Aerodynamics*. Pergamon Press, Oxford, 1958.

[40] J. Shen and W. C. Meecham. Quadrupole directivity of jet noise associated when impinging on normal plates. *Journal of the Acoustical Society of America* **94** 1415–1424, 1993.

[41] E. Silberman and C. S. Song. Instability of ventilated cavities. *Journal of Ship Research* **5** (1) 13–33, 1961.

[42] I. N. Sneddon. *The Use of Integral Transforms*. McGraw-Hill, New York, 1972.

[43] C. S. Song. Pulsation of ventilated cavities. *Journal of Ship Research* **5** (4) 8–20, 1962.

[44] J. A. Stratton. *Electromagnetic Theory*. McGraw-Hill Book Company, New York, 1941.

[45] D. R. Strong, T. E. Siddon, and W. T. Chu. Pressure Fluctuation on a Flat Plate with Oblique Jet Impingement. Technical Report CR-839, NASA, 1967.

[46] J.-M. Vanden-Broeck. Deformation of a liquid surface by an impinging gas jet. *SIAM Journal of Applied Mathematics* **41** (2) 306–309, 1981.

[47] G. N. Watson. The diffraction of electric waves by the Earth. *Proceedings of the Royal Society of London A* **95** 83–99, 1919.

[48] S. D. Young, T. A. Brungart, G. C. Lauchle, and M. S. Howe. Effect of a downstream ventilated gas cavity on the spectrum of turbulent boundary layer wall pressure fluctuations. *Journal of the Acoustical Society of America* **118** 3506–3512, 2005.

REPORT DOCUMENTATION PAGE

Form Approved
OMB No. 0704-0188

1. REPORT DATE *(DD-MM-YYYY)*
20-08-2009

2. REPORT TYPE
Final Technical

3. DATES COVERED *(From - To)*
May 2006 - May 2009

4. TITLE AND SUBTITLE
INVESTIGATIONS OF THE SOUND
GENERATED BY SUPERCAVITY VENTILATION

5a. CONTRACT NUMBER

5b. GRANT NUMBER
N00014-06-1-0270

5c. PROGRAM ELEMENT NUMBER

6. AUTHOR(S)
Howe, Michael S. and Foley, Alia W.

5d. PROJECT NUMBER

5e. TASK NUMBER

5f. WORK UNIT NUMBER

7. PERFORMING ORGANIZATION NAME(S) AND ADDRESS(ES)
Boston University, College of Engineering
110 Cummington St. Boston MA 02215

8. PERFORMING ORGANIZATION REPORT NUMBER
ME09-13

9. SPONSORING/MONITORING AGENCY NAME(S) AND ADDRESS(ES)
Office of Naval Research, Code 333
875 N. Randolph St.
One Liberty Center
Arlington, VA 22203-1995

10. SPONSOR/MONITOR'S ACRONYM(S)
ONR-ULI

11. SPONSOR/MONITOR'S REPORT NUMBER(S)

12. DISTRIBUTION/AVAILABILITY STATEMENT
APPROVED FOR PUBLIC RELEASE

13. SUPPLEMENTARY NOTES

14. ABSTRACT

An investigation is made of the sound generated by the impingement of a ventilating jet on the interface of a ventilated supercavity. A ventilated supercavity is a gaseous envelope generated around an underwater vehicle that allows for order of magnitude increases in vehicle speeds. Hydrodynamic noise generated by the supercavity can interfere with successful vehicle deployment. A principal mechanisms of noise generation is believed to be the impingement of ventilating gas jets on the gas-water cavity wall. An understanding of this interaction has been developed by analysis of a series of model problems which approximate the geometry and physical mechanisms involved in the jet-cavity interaction. The first problem is that of a spherical, gas-filled cavity in water whose surface is excited by a planar ring of axially projecting jets. The second involves a theoretical and experimental study of a jet of infinitesimal cross-section impinging at normal incidence on the gas-water interface. The final problem makes use of a creeping mode diffraction theory to estimate the 'self-noise' produced by the impinging jets on the solid nose of the vehicle.

15. SUBJECT TERMS
supercavitating vehicle, aerodynamic sound, self noise, jet noise

16. SECURITY CLASSIFICATION OF:			17. LIMITATION OF ABSTRACT	18. NUMBER OF PAGES	19a. NAME OF RESPONSIBLE PERSON
a. REPORT	b. ABSTRACT	c. THIS PAGE			
U	U	U	UU	146	19b. TELEPHONE NUMBER *(Include area code)*

Reset